

Warsaw University  
Faculty of Physics  
Institute of Experimental Physics

# HIGGS-BOSON PRODUCTION AT THE PHOTON COLLIDER AT TESLA

Piotr Nieżurawski

Thesis submitted to the Warsaw University  
in partial fulfillment of the requirements  
for the Ph. D. degree in Physics.

Prepared under supervision  
of Dr. hab. Aleksander Filip Żarnecki.

Warsaw 2005



*What exists is beyond reach and very deep.*

*Who can discover it?*

*Ecclesiastes 7,24*



## Abstract

In this thesis feasibility of the precise measurement of the Higgs-boson production cross section at the Photon Collider at TESLA is studied in detail. For the Standard-Model Higgs-boson production the decay to  $b\bar{b}$  pairs is considered for the mass between 120 and 160 GeV. The same decay channel is also studied for production of the heavy neutral Higgs bosons in MSSM, for masses 200–350 GeV. For the first time in this type of analysis all relevant experimental and theoretical effects, which could affect the measurement, are taken into account.

The study is based on the realistic  $\gamma\gamma$ -luminosity spectra simulation. The heavy quark background  $\gamma\gamma \rightarrow Q\bar{Q}(g)$  is estimated using the dedicated code based on NLO QCD calculations. Other background processes, which were neglected in the earlier analyses, are also studied:  $\gamma\gamma \rightarrow W^+W^-$ ,  $\gamma\gamma \rightarrow \tau^+\tau^-$ , and light-quark pair production  $\gamma\gamma \rightarrow q\bar{q}$ . Also the contribution from the so-called overlaying events,  $\gamma\gamma \rightarrow hadrons$ , is taken into account; a dedicated package called ORLOP has been prepared for this task. The non-zero beam crossing angle and the finite size of colliding bunches are included in the event generation. The analysis is based on the full detector simulation with realistic  $b$ -tagging, and the criteria of event selection are optimized separately for each considered Higgs-boson mass.

In spite of the significant background contribution and deterioration of the invariant mass resolution due to overlaying events, precise measurement of the Higgs-boson production cross section is still possible. For the Standard-Model Higgs boson with mass of 120 to 160 GeV the partial width  $\Gamma(h \rightarrow \gamma\gamma)\text{BR}(h \rightarrow b\bar{b})$  can be measured with a statistical accuracy of 2.1–7.7% after one year of the Photon Collider running. The systematic uncertainties of the measurement are estimated to be of the order of 2%. For MSSM Higgs bosons  $A$  and  $H$ , for  $M_A = 200\text{--}350$  GeV and  $\tan\beta = 7$ , the statistical precision of the cross-section measurement is estimated to be 8–34%, for four considered MSSM parameters sets. As heavy neutral Higgs bosons in this scenario may not be discovered at LHC or at the first stage of the  $e^+e^-$  collider, an opportunity of being a discovery machine is also studied for the Photon Collider.



# Contents

<b>1</b>	<b>Introduction</b>	<b>5</b>
<b>2</b>	<b>Motivation</b>	<b>9</b>
2.1	The Higgs sector in the SM . . . . .	9
2.2	Higgs sector in the MSSM . . . . .	10
2.3	Status of the Higgs-boson searches . . . . .	11
2.4	Prospects for Higgs-boson measurements . . . . .	12
<b>3</b>	<b>Collider and detector</b>	<b>17</b>
3.1	The TESLA Linear $e^+e^-$ Collider . . . . .	17
3.2	A photon collider as an extension of the LC . . . . .	18
3.3	The Photon Collider at TESLA . . . . .	22
3.3.1	Photon-photon luminosity spectra . . . . .	22
3.3.2	Collision region . . . . .	24
3.4	The detector at TESLA . . . . .	26
3.4.1	Simulation setup . . . . .	30
<b>4</b>	<b>Signal and background</b>	<b>31</b>
4.1	Signal processes . . . . .	31
4.2	Heavy quark production background . . . . .	35
4.3	Other background processes . . . . .	35
4.4	Overlaying events $\gamma\gamma \rightarrow hadrons$ . . . . .	37
<b>5</b>	<b>Standard Model Higgs-boson production</b>	<b>41</b>
5.1	Preselection of energy-flow objects and jet reconstruction . . . . .	41
5.2	Kinematical and topological cuts . . . . .	43
5.3	$b$ -tagging algorithm . . . . .	45
5.4	Results . . . . .	50
<b>6</b>	<b>Production of heavy neutral Higgs bosons in the MSSM</b>	<b>59</b>

<b>7 Summary</b>	<b>73</b>
<b>A Event generation with overlaying events</b>	<b>79</b>
<b>B Influence of higher order corrections</b>	<b>81</b>
<b>C Studies on the influence of overlaying events</b>	<b>83</b>
<b>D ORLOP</b>	<b>93</b>



# Chapter 1

## Introduction

So far, all experimental results concerning fundamental particles and their interactions are well described by the Standard Model (SM), consisting of the electroweak theory (EWT) and the quantum chromodynamics (QCD). These theories allow us to quantify electromagnetic, weak and strong processes; among all known kinds of interactions only the gravity is not incorporated in the SM framework. The very important ingredient of the SM is the so-called Higgs boson,  $h$ , which is responsible for generating masses of all particles. Although predicted by the model, the Higgs boson has not yet been experimentally detected. However, such a particle must exist if the SM is to remain a consistent theory. Consequently, a search for the Higgs boson is among the most important tasks of the present and future colliders. Once the Higgs boson is discovered, it will be crucial to determine its properties with high accuracy, to understand the mechanism of the so-called electroweak symmetry breaking (EWSB).

The neutral Higgs boson couples to the photon pair only at the loop level, through loops of all massive charged particles. In the SM the dominant contribution is due to  $W$  and  $t$  loops. This loop-induced  $h\gamma\gamma$  coupling is sensitive to contributions of new particles which may appear in various extensions of the SM. Hence, the precise measurement of the Higgs-boson partial width  $\Gamma(h \rightarrow \gamma\gamma)$  can indicate existence of very heavy particles even if their direct production is not possible. A photon-collider option<sup>1</sup> of the  $e^+e^-$  collider offers a unique possibility to produce the Higgs boson as an  $s$ -channel resonance in the process  $\gamma\gamma \rightarrow h$ . As the SM Higgs boson with the mass<sup>2</sup> below  $\sim 140$  GeV is expected to decay predominantly into the  $b\bar{b}$  final state, we consider the measurement of the cross section for the process  $\gamma\gamma \rightarrow h \rightarrow b\bar{b}$ , shown in Fig. 1.1, for the Higgs-boson mass in

---

<sup>1</sup>A photon collider option was foreseen for all projects of the  $e^+e^-$  linear collider: TESLA [1], NLC [2] and GLC (earlier JLC) [3, 4]. In this work the photon collider at the TESLA is considered. The superconducting technology developed within the TESLA project has been recently selected as the best suited for the International Linear Collider. Decision of the International Technology Recommendation Panel was presented during the ICHEP2004 conference in Beijing [5].

<sup>2</sup>The energy unit [GeV] is used for masses and momenta, *i.e.* the speed of light is set to 1. However, for lengths and times the corresponding units are [m] and [s].

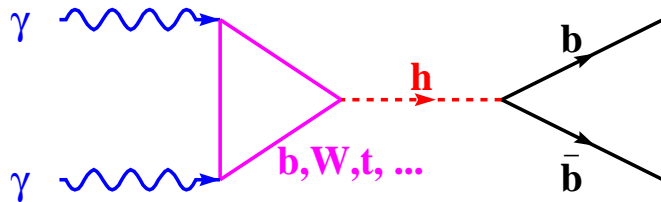


Figure 1.1: A diagram of the process  $\gamma\gamma \rightarrow h \rightarrow b\bar{b}$ . The Higgs boson particle couples to photons through the loop of all massive and charged particles.

the range  $M_h = 120\text{--}160$  GeV. The aim of this study is to estimate the precision with which this measurement and extraction of  $\Gamma(h \rightarrow \gamma\gamma)$  will be possible after one year of the TESLA Photon Collider running.

Besides precision measurements, a photon collider can be also considered as a candidate for a discovery machine. In case of the Minimal Supersymmetric extension of the SM (MSSM) the photon collider will be able to measure the production cross section of the heavy neutral Higgs bosons,  $A$  and  $H$ , covering the so-called “LHC wedge” in the MSSM parameter space, *i.e.* region of intermediate values of  $\tan\beta$ ,  $\tan\beta \approx 4\text{--}10$ , and masses  $M_{A,H}$  above 200 GeV. For this part of parameter space, MSSM Higgs bosons  $A$  and  $H$  may not be discovered at the LHC [6, 7, 8] and at the first stage of the  $e^+e^-$  linear collider [9] because of small branching ratios into leptons or photons (which allow the efficient signal selection) and because of the kinematical limit  $M_{A,H} \lesssim \sqrt{s_{ee}}/2$  for pair production process  $e^+e^- \rightarrow AH$ , respectively. Parameter range considered in this analysis corresponds to a SM-like scenario where the lightest MSSM Higgs boson  $h$  has properties similar to the SM Higgs boson, while heavy neutral Higgs bosons are nearly degenerated in mass and have negligible couplings to the gauge bosons  $W/Z$ . We consider the process  $\gamma\gamma \rightarrow A, H \rightarrow b\bar{b}$  at the Photon Collider at TESLA for Higgs-boson masses  $M_A = 200\text{--}350$  GeV. The aim of the presented study is to evaluate the discovery potential of the considered experiment by estimating the statistical significance of the signal measurement for the chosen region in the MSSM parameters space. Also the precision of the  $\gamma\gamma \rightarrow A, H \rightarrow b\bar{b}$  cross section measurement is estimated.

The measurements of  $\Gamma(h \rightarrow \gamma\gamma)\text{BR}(h \rightarrow b\bar{b})$  and  $\sigma(\gamma\gamma \rightarrow A, H \rightarrow b\bar{b})$  at a photon collider have already been studied before [10, 11, 12, 13, 14, 15, 16, 17, 18, 19, 4, 20, 21, 22, 23, 24, 25, 26, 27, 28, 29, 30, 31]. Although very promising estimates were obtained, many important aspects of the measurement were not considered. This study is the first one to take all relevant experimental and theoretical effects into account. Only results of such a realistic analysis can be used to support the project of the Photon Collider in the framework of the International Linear Collider.

The motivation for this study is outlined in Chapter 2. The proposed experimental setup and simulation tools are described in Chapter 3. In Chapter 4 details of the signal

and background simulations are given. A discussion of the event selection and the final results for SM and MSSM scenarios are given in Chapters 5 and 6, respectively. All results presented in Chapters 4, 5 and 6, and in Appendices were obtained by the author of this thesis.



# Chapter 2

## Motivation

In this chapter our current understanding of the Higgs mechanism and prospects for a discovery of the Higgs boson are outlined. The Higgs sector in the SM is discussed first, then its extension to the MSSM is shortly reviewed. Current limits on the Higgs-boson mass from direct and indirect measurements are summarized. Expected experimental results at future colliders, relevant to the presented study, are also given. An in-depth review of the Higgs-boson theory and phenomenology can be found, for example, in [32, 33]. An extensive summary of experimental results concerning Higgs-boson searches is presented in [34].

### 2.1 The Higgs sector in the SM

Among all fundamental particles of the SM only the Higgs boson still remains hypothetical. This neutral spinless particle is required in the model to *break* the gauge symmetry of weak interactions. Photon, which is a carrier of electromagnetic force, is massless. But three weak bosons  $Z$ ,  $W^+$  and  $W^-$  are massive; this is a serious difficulty as SM equations for interactions involving massive bosons lack a very basic property, the so-called *gauge invariance*<sup>1</sup>. Other problem emerges in cross section calculations for some weak processes, *e.g.*  $e^+e^- \rightarrow W^+W^-$ , because *unitarity* condition is violated for this transition. Probability current is not conserved unless we introduce new particles which couple to electrons and massive bosons. One complex Higgs doublet (four real scalar fields) is introduced in the SM in order to describe experimental results and to preserve clear theoretical picture. These new fields, filling the vacuum, couple to the massless vector bosons, giving them effective mass. This mechanism, introduced by P. Higgs [35], allows

---

<sup>1</sup>A principle of gauge invariance originates in the classical theory of electromagnetism and reads: there is a transformation of electromagnetic four-potential  $A^\mu$  after which physically relevant fields,  $\vec{E}$  and  $\vec{B}$  (or the tensor  $F^{\mu\nu} = \partial^\mu A^\nu - \partial^\nu A^\mu$ ), remain unchanged. In quantum field theories the invariance of equations after simultaneous, special transformations of all fields is required. Thus, the gauge invariance principle determines the allowed interaction terms.

us to introduce massive gauge bosons in the theoretical description without violating the gauge invariance (so-called spontaneous symmetry breaking). One of the scalar fields is expected to exist as a real particle, so-called Higgs boson,  $h$ . All couplings of the Higgs boson to other particles and its self-couplings are predicted by the SM; the couplings to bosons (fermions) are proportional to the mass squared of the boson (the mass of the fermion). The only unknown parameter of the theory is the Higgs-boson mass,  $M_h$ . An intelligible introduction to the Higgs mechanism can be found, for example, in [36].

The SM constitutes a complete effective theory of fundamental interactions (excluding gravity). Existence of the new particle, the Higgs boson, explains how the electroweak symmetry (or gauge invariance) is broken and solves the unitarity problem in weak reactions. However, this great theoretical achievement is undermined by some unsolved problems. On the way to the Planck energy scale some new phenomena are expected to appear. Otherwise, without unnatural tuning, higher order corrections to the Higgs-boson mass diverge as the energy scale increases (so called “hierarchy problem”). The second problem is due to our expectation that at some high energy scale all interactions should unify (*i.e.* their couplings should be equal) which is not exactly the case in the SM.<sup>2</sup> To fulfill this unification requirement new particles or interactions have to be introduced.

## 2.2 Higgs sector in the MSSM

The new symmetry between bosons and fermions, so-called *supersymmetry* (SUSY), could remove the two above-mentioned problems of the SM. It guaranties cancellation of divergences in Higgs-mass calculation.<sup>3</sup> Also the unification of three fundamental couplings is realized. However, in the general case of the Minimal Supersymmetric extension of the SM (MSSM) around 100 new parameters must be introduced whose values are not predicted by the model. All SM particles have their superpartners: fermions – spin-zero bosons (*e.g.* electron – selectron), bosons – fermions (*e.g.* higgs – higgsino,  $W$  –  $W$ -ino, photon – photino). To generate masses for all particles and sparticles, two Higgs doublets (*i.e.* eight fields) have to be introduced. As a result, supersymmetric models contain five Higgs bosons (instead of one Higgs particle). Two of them are neutral scalars and are denoted as  $h$  and  $H$ .<sup>4</sup> There is also one neutral pseudoscalar,  $A$ , and two charged scalars:  $H^+$  and  $H^-$ .

The Higgs sector of the MSSM is described by a subset of parameters which includes:

---

<sup>2</sup>Only approximate unification is obtained in the SM. At the scale of  $M_{\text{GUT}} \sim 10^{15}$  GeV couplings are ‘unified’ to  $\mathcal{O}(10\%)$  [37].

<sup>3</sup>In fact, cancellation is not exact as the supersymmetry is broken, *i.e.* particles have different masses than their superpartners. This results in the prediction that masses of superpartners cannot be heavier than a few TeV. Otherwise supersymmetry does not solve the hierarchy problem.

<sup>4</sup>By definition,  $h$  denotes the lighter scalar Higgs boson, and  $H$  denotes the heavier one.

1.  $\tan\beta$  – the ratio of vacuum expectation values of neutral Higgs fields coupling to *up*- and *down*-type fermions,  $\tan\beta = v_u/v_d$ .
2.  $M_A$  – the mass of the neutral, pseudoscalar Higgs boson,  $A$ .
3.  $\mu$  – the supersymmetry-breaking higgs-higgsino mass parameter.
4.  $M_2$  – the supersymmetry-breaking universal gaugino mass parameter (mass of the  $W$ -ino; masses of other gauginos are related with  $M_2$ ).
5.  $M_{\tilde{f}_L}$ ,  $M_{\tilde{f}_R}$  and  $A_{\tilde{f}}$  – other supersymmetry-breaking parameters: masses of left- and right-handed supersymmetric partners of fermion  $f$  and their coupling to Higgs bosons, respectively.

Only first two parameters,  $\tan\beta$  and  $M_A$ , influence the Higgs sector on the tree level. Other parameters can affect properties of the Higgs bosons via radiative corrections. In contrast to the SM, mass of the lightest Higgs boson,  $h$ , is constrained, *i.e.*  $h$  cannot be heavier than around 150 GeV.

## 2.3 Status of the Higgs-boson searches

In precise calculations of the SM predictions the higher order corrections resulting from the Higgs boson contribution are sizable and must be taken into account. Expected results for many observables depend on the Higgs-boson mass,  $M_h$ . Thus, constraints on the value of  $M_h$  can be obtained from the analysis of electroweak measurements. The result of such analysis is shown in Fig. 2.1 [38], where the  $\chi^2$  value from the SM fit to precise measurements at LEP, SLC, Tevatron and other experiments is presented as a function of the Higgs-boson mass. The best agreement is found for  $M_h \approx 126$  GeV, and with 95% C.L. the upper limit on  $M_h$  is 280 GeV. The best fit value is slightly above the lower mass limit from the direct searches at LEP; excluded is the mass range  $M_h < 114.4$  GeV [39].

In the MSSM case limits for the Higgs-boson masses depend on other model parameters. In the general approach, when other parameters are allowed to vary, we can only conclude that all Higgs bosons must be heavier than 80–90 GeV if model with no  $CP$ -violation in Higgs sector is assumed. However, some MSSM parameter sets result in the lightest *higgs*,  $h$ , having couplings similar to those of the SM Higgs boson (SM-like scenarios). In such cases the Higgs-boson mass constraints are similar to those obtained in the SM.

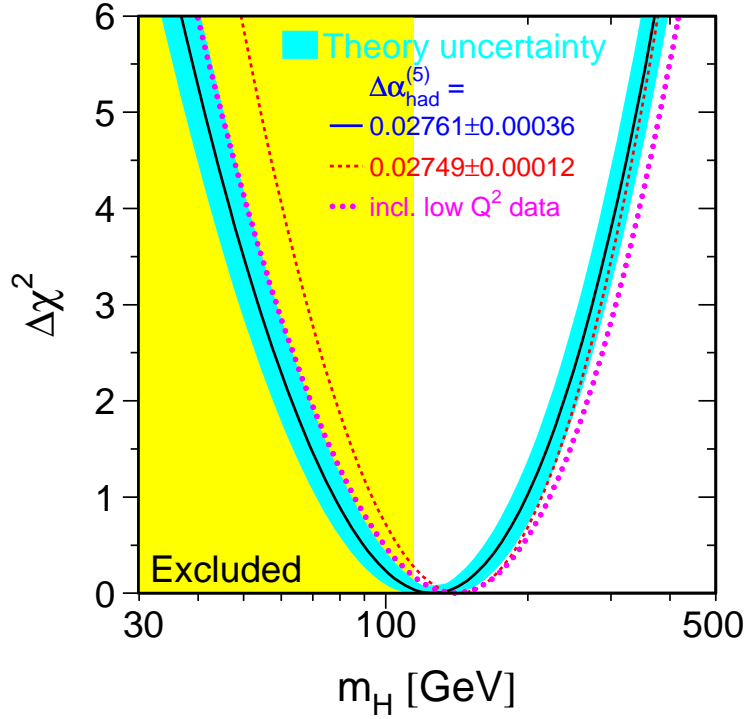


Figure 2.1: The result of the SM fit to the precision electroweak measurements [38]. The  $\Delta\chi^2 = \chi^2 - \chi_{\min}^2$  value is presented as a function of the Higgs-boson mass (here denoted as  $m_H$ ). The best agreement is found for  $M_h \approx 126$  GeV, and with 95% C.L. the upper limit on  $M_h$  is 280 GeV. Excluded mass range from direct searches at LEP,  $M_h < 114.4$  GeV, is indicated in yellow. The band represents the theoretical uncertainty due to missing higher order corrections.

## 2.4 Prospects for Higgs-boson measurements

If the mass of the SM Higgs boson is around 115 GeV it is still possible that it will be discovered at the Tevatron. However, only future machines will have sufficient *higgs* production rates to measure precisely the mass and couplings of the Higgs boson(s). All large accelerator projects aim at measurements of the Higgs-boson properties from which the fundamental one is the mass,  $M_h$ , being at the same time the only unknown parameter in the SM. Measurements of other parameters describing the Higgs boson (total and partial widths, branching ratios, spin, parity) are considered as the crucial tests of the SM and its extensions. Below the estimated precisions of future measurements are summarized, in the expected order of appearance.



## Large Hadron Collider

At the Large Hadron Collider (LHC), which should become operational in 2007, Higgs boson(s) will be produced in processes of gluon fusion (about 80% of the SM Higgs-boson production rate for  $M_h < 2M_Z$ ) and  $W$  boson fusion. Both experiments, ATLAS and CMS, have presented detailed studies showing that the SM Higgs boson will be discovered at LHC if it is lighter than about 1 TeV. The Higgs-boson mass can be measured with precision about 0.1% for  $M_h \lesssim 400$  GeV [40].

Various ratios of Higgs partial widths can be determined with precisions about 10–20%, assuming integrated luminosity of  $100 \text{ fb}^{-1}$  [41]. For heavy SM *higgs*,  $M_h \gtrsim 250$  GeV, also its total width,  $\Gamma_h$ , can be measured as it becomes larger than the experimental mass resolution [40]. The heavy MSSM Higgs bosons,  $A$  and  $H$ , will be observed at the LHC for most of the allowed MSSM parameter space. However, there is a region of  $M_A - \tan\beta$  values where the LHC may not be able to discover heavy MSSM Higgs bosons. This is the so called “LHC wedge” covering  $M_A > 200$  GeV and  $\tan\beta \approx 4\text{--}10$ .

## Linear $e^+e^-$ Collider

According to the currently proposed schedule, the  $e^+e^-$  International Linear Collider (ILC) can become operational in 2015. Two processes contribute to the Higgs-boson production at the ILC: Higgs-strahlung and vector boson fusion. For the SM Higgs boson with mass in the range  $M_h \approx 115\text{--}180$  GeV the expected precision of the mass measurement can be better than 0.05% [9]. As the background is much smaller than at the LHC, Higgs-boson branching ratios can be determined with much better precision and in the model-independent way. Branching ratios  $\text{BR}(h \rightarrow \gamma\gamma)$  and  $\text{BR}(h \rightarrow b\bar{b})$  may be determined with accuracy of about 10% and 1.5%, respectively, after one year of ILC running at nominal luminosity [42, 43].

## Experiments after LHC and LC

After LHC and ILC measurements there will still be some properties of the Higgs-boson(s) which are poorly known and should be determined with greater precision at other experiments. One of the interesting quantities is the  $\gamma\gamma$  partial width,  $\Gamma(h \rightarrow \gamma\gamma) = \Gamma_h \text{BR}(h \rightarrow \gamma\gamma)$ . As already mentioned in Chapter 1, measurement of partial width  $\Gamma(h \rightarrow \gamma\gamma)$  is of special importance as it is sensitive to all charged particles which have mass generated by the Higgs mechanism. Due to the so-called non-decoupling effect contributions of the heavy charged particles to the  $h \rightarrow \gamma\gamma$  loop are finite even in the limit of infinite mass of the particle. Thus, the measurement of  $\Gamma(h \rightarrow \gamma\gamma)$  can indicate existence of particles whose direct production will be impossible in available accelerators.

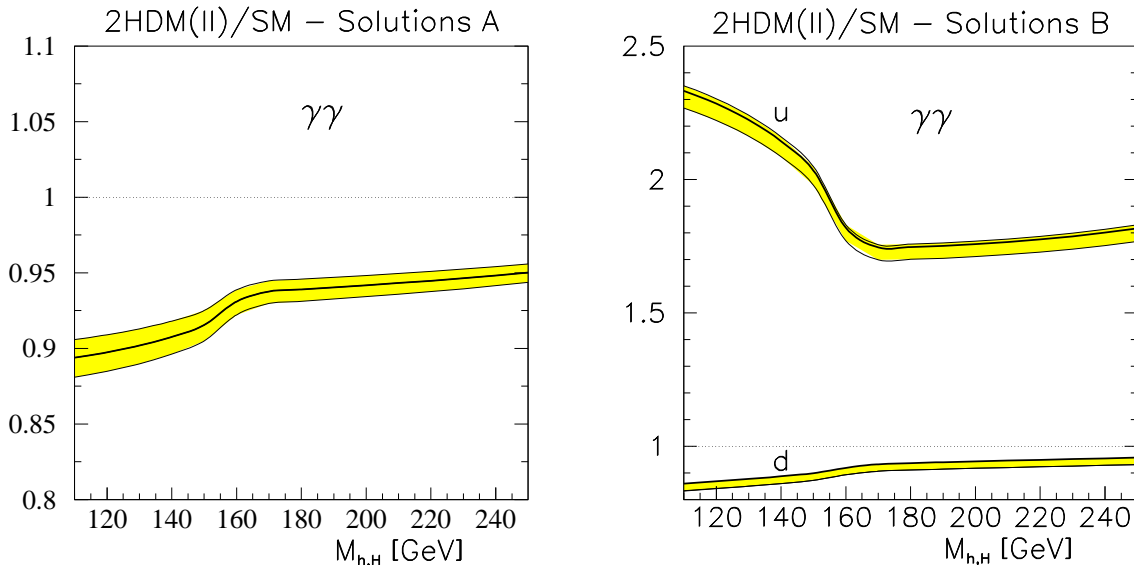


Figure 2.2: Ratio of the  $higgs \rightarrow \gamma\gamma$  decay widths in the 2HDM and the SM as a function of the  $higgs$  mass,  $M_{h,H}$ , for solutions A (left) and B (right) [47]. The yellow bands correspond to the uncertainties expected at  $M_{h,H} = 120$  GeV.

In the MSSM, the loop induced coupling is sensitive to contributions of supersymmetric particles [44, 46, 45]: chargino and top squark loops can lead even to 60% difference between the SM and the SUSY couplings. Scenarios, in which all new particles are very heavy, may be realised not only in the MSSM but also in other models with extended Higgs sector, for example in the Two Higgs Doublet Model (2HDM). In this case the two-photon width of the Higgs boson will differ from the SM value due to the contributions of the heavy charged Higgs bosons, even if all direct couplings to gauge bosons and fermions are equal to the corresponding SM couplings. Different realizations of the 2HDM have been discussed in [47]. Assuming that the partial widths of the observed Higgs boson to quarks,  $Z$  or  $W$  bosons are close to their SM values (SM-like scenario), three different combinations of couplings are possible. Fig. 2.2 shows deviations of the two-photon Higgs width from the SM value for the three SM-like solutions considered in [47]. For solution  $B_u$  one expects significant deviation from the SM predictions since, as compared to the SM, there is a change of the relative sign of the top-quark and the  $W$  contributions. Consequently, for solution  $B_u$  the  $higgs \rightarrow \gamma\gamma$  width is significantly larger than in the SM, where these two contributions partly cancel each other. However, deviation due to the charged Higgs-boson contribution only (solution A) is much smaller, of the order of 5–10%, and the measurement with precision at the level of a few percent is required.

The machine best suited for the measurement of the Higgs boson two-photon width is a photon collider. All photon collider proposals (within TESLA, NLC, GLC and CLIC projects) emphasize the feasibility of a very precise  $\Gamma(h \rightarrow \gamma\gamma)$  measurement. For the

light SM-like Higgs boson the most promising process is  $\gamma\gamma \rightarrow h \rightarrow b\bar{b}$  due to the very high branching ratio  $\text{BR}(h \rightarrow b\bar{b})$ . The measurement of the cross section for this process has been studied in detail and is the main subject of this work. One has to note that the final results on  $\Gamma(h \rightarrow \gamma\gamma)$  from a photon collider must rely on  $\text{BR}(h \rightarrow b\bar{b})$  measurement from other experiment – this branching ratio should be determined at LC with precision of around 1.5% [43]. Measurements of  $\Gamma(h \rightarrow \gamma\gamma)\text{BR}(h \rightarrow b\bar{b})$  at the Photon Collider and of the branching ratios  $\text{BR}(h \rightarrow \gamma\gamma)$  and  $\text{BR}(h \rightarrow b\bar{b})$  at the  $e^+e^-$  collider can be used to determine the total Higgs width,  $\Gamma_h$ , in a model independent way.

The quantity  $\Gamma(h \rightarrow \gamma\gamma)\text{BR}(h \rightarrow \gamma\gamma)$  could also be unfolded from the cross section measurement for the process  $\gamma\gamma \rightarrow h \rightarrow \gamma\gamma$ . Unfortunately this process has a very low rate due to small  $\gamma\gamma$  branching ratio. Moreover, in addition to a one-loop background process  $\gamma\gamma \rightarrow \gamma\gamma$  also ‘machine’ background  $e\gamma \rightarrow e\gamma$  must be considered. Even with optimistic assumptions about angular coverage (down to  $3^\circ$ ) and high granularity of calorimeter the precision of the measurement has been estimated to be of the order of 30% [45]. Therefore this measurement cannot be considered as an alternative to the analysis of the process  $\gamma\gamma \rightarrow h \rightarrow b\bar{b}$ .

The Photon Collider (PC) seems to be the only machine allowing precise measurement of  $\Gamma(h \rightarrow \gamma\gamma)$ . However, physics potential of the PC is much richer and complementary to that of the LHC and the ILC. For Higgs sector itself many interesting measurements can be considered:

- CP-parity of the Higgs boson. The CP-parity of the Higgs boson can be determined in a model independent way from analysis of angular correlations in 4-fermion decays  $h \rightarrow W^+W^- \rightarrow 4j$  and  $h \rightarrow ZZ \rightarrow 2j2l$  [48]. Similar measurements have been also proposed for LHC and ILC.
- Phase of the  $h \rightarrow \gamma\gamma$  coupling. In addition to  $\Gamma(h \rightarrow \gamma\gamma)$ , precise measurements at the PC are also sensitive to the phase of the  $h \rightarrow \gamma\gamma$  amplitude,  $\phi_{h\gamma\gamma}$ . The phase  $\phi_{h\gamma\gamma}$  can be extracted from the measurement of the interference between the resonant *higgs* production processes  $\gamma\gamma \rightarrow h \rightarrow W^+W^-$  and the background process  $\gamma\gamma \rightarrow W^+W^-$  [49]. It turns out that for *higgs* mass of the order of 300–400 GeV the phase  $\phi_{h\gamma\gamma}$  is more sensitive to possible contributions of heavy charged scalar particle than  $\Gamma(h \rightarrow \gamma\gamma)$ . Only by combining  $\Gamma(h \rightarrow \gamma\gamma)$  and  $\phi_{h\gamma\gamma}$  measurements at the PC with those at the LHC and at the LC unique determination of the Higgs-boson couplings and distinction between various models will be possible.
- Charged Higgs-bosons production. For intermediate values of  $\tan\beta$  the charged MSSM Higgs boson,  $H^\pm$ , may not be discovered at the LHC, if its mass is greater than  $\sim 150$  GeV [7, 8]. In the photon collider  $H^+H^-$  pairs can be produced in QED

process and the mass reach for discovery can be extended up to  $\sim 300$  GeV (if running at  $\sqrt{s_{ee}} = 800$  GeV). At the  $e^+e^-$  LC, running with  $\sqrt{s_{ee}} = 800$  GeV, almost an order of magnitude smaller number of *higgs* pairs could be produced during the same time due to smaller cross section [9, 1].

The second generation  $e^+e^-$  linear collider project for which the feasibility study is still in progress is CLIC [50]. At this accelerator multi-TeV energies will be obtained, and the wider range of masses will be accessible for new-particle searches. The photon-photon collision mode has been proposed for this machine as well, but the detailed physics case studies are still missing.

Opportunity of studying elementary particle collisions at multi-TeV energies is the main reason for considering the next generation project of a muon collider. As muons lose much less energy via bremsstrahlung than electrons a circular accelerator option is preferable even for much higher beam energies than those accessible at LEP2. Circulating beams would allow the operation with high luminosity. However, progress must still be made in formation of high-intensity  $\mu$ -beams with low emittance. At the muon collider the same channels could be used for Higgs-boson measurements as at  $e^+e^-$  collider but with extended mass reach. Moreover, the  $s$ -channel production in the process  $\mu\mu \rightarrow \textit{higgs}$  has cross section sufficient for precision measurements due to higher mass of the muon [51]. As the energy spread of muon beam is expected to be negligible, energy scan at the muon collider would result in determination of the Higgs-boson mass and width with precision of the order of 2 MeV.

Construction of a photon collider based on the muon collider is also possible. Unfortunately the high mass of the muon is a problem in this case. The maximal energy of photons from Compton backscattering would be very small compared to the beam energy, *e.g.* the maximal photon energy would be only around 75 GeV at 20 TeV  $\mu$ -beam as compared to about 400 GeV for 500 GeV electrons with the same laser setup<sup>5</sup>.

---

<sup>5</sup>Laser parameters of the TESLA Photon Collider design are assumed.

# Chapter 3

## Collider and detector

### 3.1 The TESLA Linear $e^+e^-$ Collider

Results presented in this thesis are based on the design and machine parameters of the TESLA (TeV-Energy Superconducting Linear Accelerator)  $e^+e^-$  collider [52]. Accelerator design is based on the superconducting technology, recently accepted by International Technology Recommendation Panel as the best suited for the ILC project [5]. Each of the two linear accelerators, which accelerate  $e^+$  and  $e^-$  towards the interaction region, will consist of around 10000 one-meter-long superconducting cavities. Cavities made from niobium and cooled to temperature of 2 K can provide accelerating field with gradient well above 35 MV/m. As the average gradient equal to 23.4 MV/m is required for operation at the nominal total collision energy of 500 GeV, the opportunity emerges to increase the machine reach up to 800 GeV or even 1 TeV. With dumping rings and other additional accelerator components the total length of the machine is 33 km. Main machine parameters are listed in the table 3.1.

Description of the parameter	Value of the parameter
Accelerating gradient	23.4 MV/m
No. of accelerating structures	21024
Train repetition rate	5 Hz
No. of bunches per train	2820
Bunch spacing	337 ns
No. of $e^-(e^+)$ per bunch	$2 \cdot 10^{10}$
Beam size at IP ( $\sigma_x; \sigma_y$ )	553 nm; 5 nm
Bunch length at IP ( $\sigma_z$ )	0.3 mm
Luminosity	$3.4 \cdot 10^{34} \text{ cm}^{-2}\text{s}^{-1} = 34 \text{ nb}^{-1}\text{s}^{-1}$
Luminosity per year	$340 \text{ fb}^{-1}\text{y}^{-1}$

Table 3.1: Main parameters of TESLA Linear Collider for the 500 GeV design. One accelerator year [y] is assumed to be equal to  $10^7$  s.

## 3.2 A photon collider as an extension of the LC

Future linear  $e^+e^-$  colliders offer unique opportunities to study photon-photon interactions if the idea of a photon collider is realized. In this option the energy of the primary electron-electron<sup>1</sup> beams is “transferred” to photons in the process of Compton back-scattering [53]. Assuming the beam electron collides with one laser photon head-on, the highest energy of the scattered photon,  $E_\gamma^{\text{max1}}$ , is equal to:

$$E_\gamma^{\text{max1}} = \frac{x}{x+1} \frac{E_e + p_e}{2},$$

$$\text{where } x = \frac{2E_L(E_e + p_e)}{m_e^2}.$$

$E_L$ ,  $E_e$ ,  $p_e$  and  $m_e$  are the energy of laser photon, the energy of beam electron, its momentum and mass, respectively. As the energy of primary electrons will be of the order of 100 GeV, one can use an approximation  $p_e \approx E_e$ . In this case the simplified formulae are obtained:

$$E_\gamma^{\text{max1}} = \frac{x}{x+1} E_e,$$

$$x = \frac{4E_L E_e}{m_e^2}.$$

Collision of a high energy photon from Compton back-scattering with a laser photon in the conversion region can result in creation of  $e^+e^-$  pairs. This process would significantly limit the  $\gamma\gamma$ -luminosity as its cross section is comparable with that of the Compton scattering. Therefore, it is preferable to select laser parameters such that the threshold for  $e^+e^-$  pair creation is not reached. The condition which has to be imposed on the invariant mass of two photons is:

$$\sqrt{s_{\gamma_L \gamma_{\text{max1}}}} = 2\sqrt{E_L E_\gamma^{\text{max1}}} < 2m_e.$$

This is equivalent to the requirement:  $x < x_{\text{thr}} = 2 + 2\sqrt{2} \approx 4.83$ .

Leading order Compton cross section formula indicates that the approximate monochromaticity of the  $\gamma$  beams can be achieved for high polarizations of colliding electrons and of laser photons. Figures 3.1 and 3.2 show the expected distributions of production probability and of the circular polarization of high-energy photons,  $P_\gamma$ , as a function of the photon energy relative to the primary electron energy,  $y = E_\gamma/E_e$ , for various combinations of laser photon polarization,  $P_c$ , and electron polarization,  $P_e$ . With the choice  $P_e = 1$  and  $P_c = -1$  most of the back-scattered photons have energies close to  $E_\gamma^{\text{max1}}$  and are highly

---

<sup>1</sup>For the photon collider positron beam is not needed. Moreover, use of two electron beams has important advantages: higher photon polarization and reduced backgrounds in the interaction region.

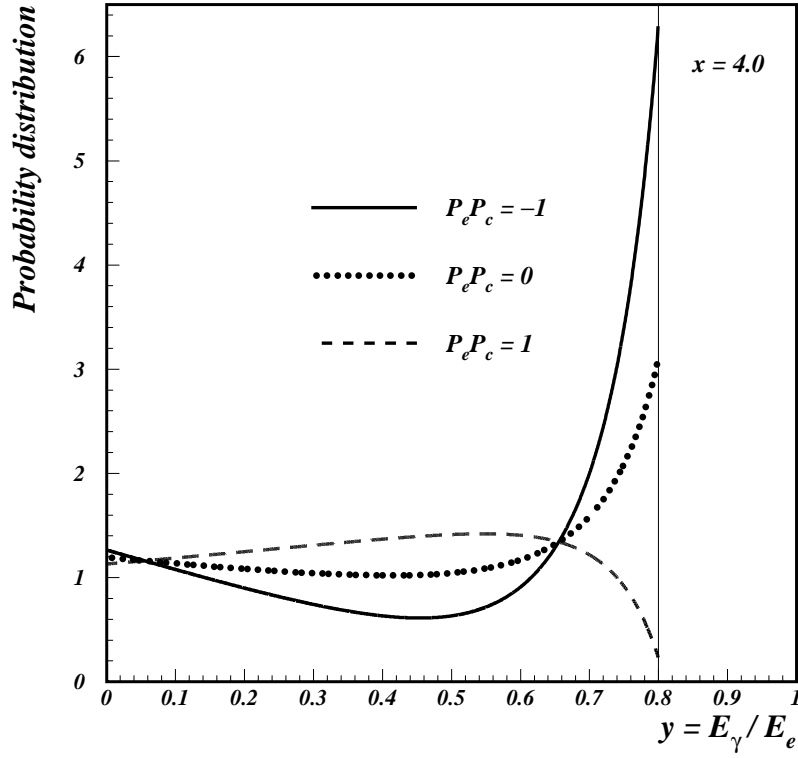


Figure 3.1: Probability distributions for production of photon with relative energy  $y = E_\gamma/E_e$ . Results for various combinations of laser and electron polarizations,  $P_c$  and  $P_e$ , are shown.

polarized.

In the laboratory frame photons from Compton back-scattering are strongly boosted in the electron-beam direction. The angular distribution has the width corresponding to the characteristic angle  $\theta_{ch} \approx 1/\gamma_e$  where  $\gamma_e$  is the relativistic factor for the beam electron,  $\gamma_e = E_e/m_e$ . For  $E_e = 250$  GeV one obtains  $\theta_{ch} \approx 2 \mu\text{rad}$ , *i.e.* the photon beam is strongly collimated along the incident electron beam direction. Therefore, two high energy photon beams produced in Compton back-scattering can be collided head on in the setup shown in Fig. 3.3. As the distance between conversion point (CP) and interaction point (IP),  $b$ , will be of the order of 3 mm, one can see that the additional spread of the photon bunch will be only about 6 nm which is much smaller than the transverse size of the  $e^-$ -bunch in the  $x$  direction and comparable with the  $e^-$ -bunch size in the  $y$  direction. Therefore, the  $\gamma\gamma$ -luminosity will be of the same order of magnitude as the  $e^-e^-$  geometrical luminosity.

Studies of the effects present in the conversion and interaction points revealed that also the following corrections should be included in a description of  $\gamma\gamma$ -luminosity spectra:

1. Correlations between energy and scattering angle of Compton photons. As more energetic photons scatter with smaller angles, high-energy photons in the 'core'

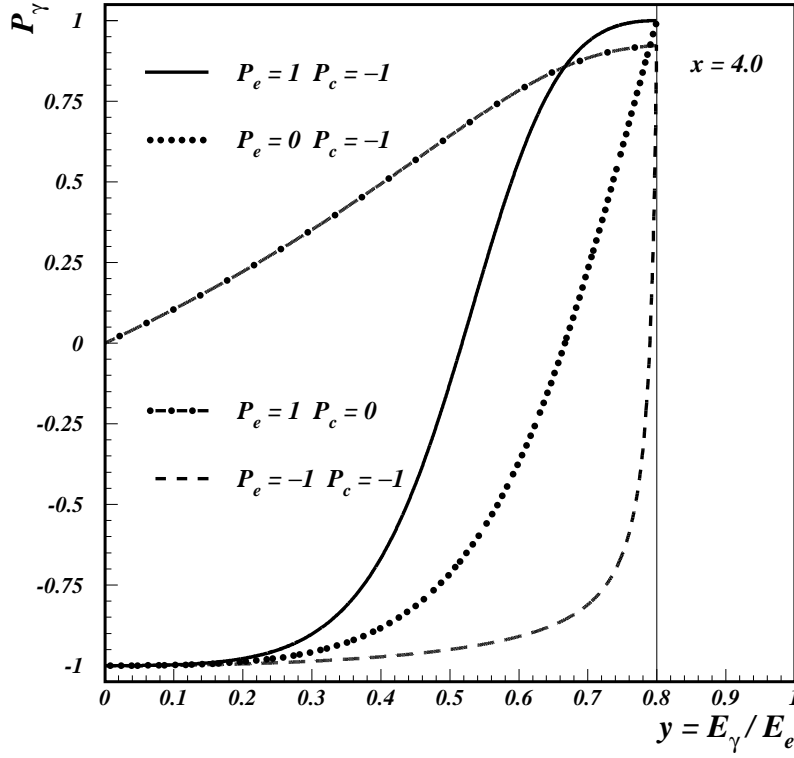


Figure 3.2: Circular polarization of scattered high energy photons,  $P_\gamma$ , as a function of relative photon energy,  $y = E_\gamma/E_e$ . Results for various combinations of laser and electron polarizations,  $P_c$  and  $P_e$ , are shown.

of the beam collide with high-energy photons of the opposite beam with greater probability than with low-energy photons forming beam 'halo'. Thanks to this effect high- $W_{\gamma\gamma}$  part of  $\gamma\gamma$ -luminosity is enhanced in comparison to the simple convolution of both spectra [58].

2. An effective increase of the electron mass due to its transverse motion in the strong electromagnetic field of the very intense laser beam:  $m_e^2 \rightarrow m_{eff}^2 = m_e^2(1 + \xi^2)$ . Here the  $\xi$  parameter is related to the strength of the electromagnetic field in the conversion region and is used to describe nonlinear effects.
3. Scattering of electrons on two laser photons:  $e^- + 2\gamma_L \rightarrow e^- + \gamma$ . Interactions with three and more laser photons are supposed to be negligible.
4. Interactions of laser photons with electrons which already scattered one or more times.
5. Nonlinear  $e^+e^-$  pair creation  $\gamma + n\gamma_L \rightarrow e^+e^-$  which should be taken into account even for  $x < x_{thr}$ .



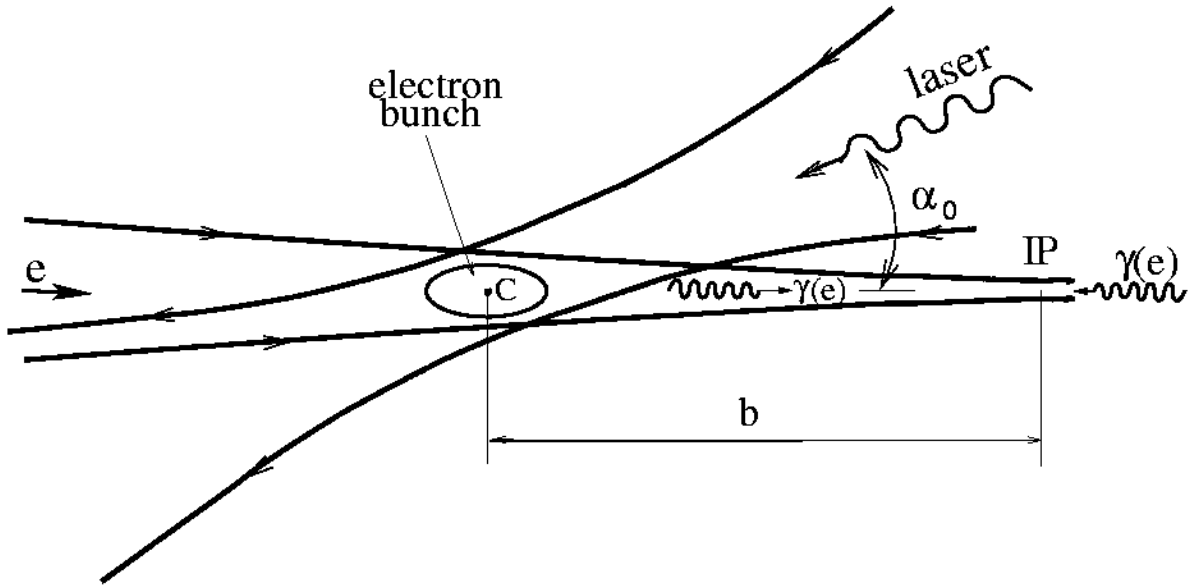


Figure 3.3: A basic scheme of the photon collider [54]. Primary electrons scatter on the laser photons (region C) at the distance  $b$  from the interaction point (IP). High-energy photons produced in the Compton back-scattering follow the electron-beam direction and collide with photons coming from the opposite side.

6. Coherent  $e^+e^-$  pair creation by a high energy photon in the electromagnetic field which is present in the interaction point.

Before the interaction point, to minimize some of aforementioned effects, the possibility was studied to remove electrons from the beam with special magnets. For a design with  $b \approx 1$  cm a small magnet was foreseen with magnetic field  $B = 5$  kG deflecting electrons before the IP. However, in the current design, optimized for highest luminosity, this is no longer possible due to the short distance of 3 mm between conversion point and IP.

The finite beams-crossing angle at the interaction point, with “crab-wise” tilted electron bunches [59] has been recently accepted as the solution for the linear collider. This is a preferred scheme for a photon collider because the removal of high-energy-photon bunches after the interaction would be very difficult with collinear beams. Crab-crossing solution preserves the same luminosity as for head-on collisions. However, electromagnetic interaction between beams must be included in the full simulation of  $\gamma\gamma$ -luminosity because primary electrons are traversing through interaction point.

The more complete description of processes outlined here and other effects influencing  $\gamma\gamma$ -luminosity spectra can be found in [55].

### 3.3 The Photon Collider at TESLA

According to the current design of the Photon Collider at TESLA [1], the energy of the laser photons is assumed to be fixed for all electron-beam energies. Laser photons are assumed to have circular polarization  $P_c = -1$ , while longitudinal polarization of electrons is  $P_e = 0.85$ . This configuration of polarizations corresponds to the energy spectra of back-scattered photons peaked at high energy (see Fig. 3.1). With the same choice of parameters for each beam we maximize probability that two high-energy photons will collide with the same polarization, *i.e.* in the state with total angular momentum,  $J$ , equal to zero, so a spinless resonance can be produced.

To profit from the peaked  $\gamma\gamma$ -luminosity spectra the energy of primary electrons has to be adjusted in order to enhance the resonance production signal at a particular mass. The use of a by-pass for electron beams is considered if the energy much lower than the nominal one is required. In this case the luminosity will be approximately proportional to the beam energy,  $L \propto E_e$ .

#### 3.3.1 Photon–photon luminosity spectra

As described in 3.2, the  $\gamma\gamma$ -luminosity spectrum is influenced by many various effects. To take them properly into account, a dedicated program for detailed beam simulation for the Photon Collider at TESLA has been developed [56]. Large samples of  $\gamma\gamma$  events were generated at selected energies and are available for further analysis. The simulated photon-photon events were directly used in this analysis when a proper description the low energy tail of the spectrum was crucial, *e.g.* for the so-called *overlaying events*<sup>2</sup>. However, in the high-energy part of the  $\gamma\gamma$  spectrum, *i.e.* for  $W_{\gamma\gamma} > 0.3 W_{\gamma\gamma}^{\max 1}$ , where  $W_{\gamma\gamma}^{\max 1} = 2E_{\gamma}^{\max 1}$ , the results of the full simulation are well described by the COMPAZ parametrization [57]. The subroutines of the COMPAZ package were used when “continuous” description was necessary. For example, in case of a very narrow resonance production the full simulation provides only a few  $\gamma\gamma$  events in the region of interest per one million of simulated photon-photon collisions. Hence, analytical approach is much more efficient. Also the NLO QCD program used for generating  $\gamma\gamma \rightarrow Q\bar{Q}(g)$  events required a functional description of the luminosity spectrum for a proper calculation of the cross section.

This analysis is based on the realistic  $\gamma\gamma$  luminosity simulation for the Photon Collider at TESLA [1]. Some earlier studies of Higgs-boson production in the process  $\gamma\gamma \rightarrow higgs \rightarrow b\bar{b}$  assumed other laser parameters and/or “ideal”  $\gamma\gamma$ -luminosity spectrum (*i.e.* spectrum corresponding to the LO Compton cross-section formula) [22, 23, 24]. The “ideal” spectrum, used in [23], is compared with COMPAZ parametrization of the realistic

---

<sup>2</sup>See Section 4.4 in Chapter 4.

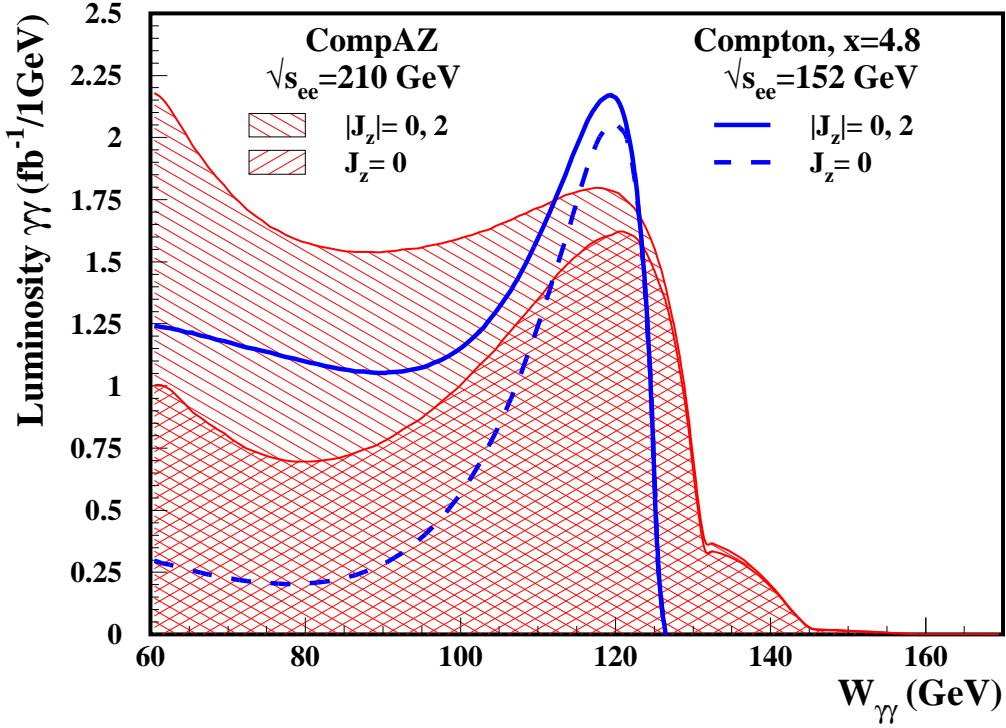


Figure 3.4: Photon-photon luminosity spectra used in the analysis of the SM Higgs-boson production with mass  $M_h = 120$  GeV, as a function of the invariant mass of the two colliding photons  $W_{\gamma\gamma}$ . The spectrum obtained from CompAZ parametrization is compared with the lowest order QED predictions for the Compton scattering, used in the earlier analysis (lines). The total luminosity distribution ( $J_z = 0, \pm 2$ ) and the  $J_z = 0$  contribution are shown, separately.

beam simulation results in Fig. 3.4. As can be seen, the “ideal” spectrum would be more advantageous for the narrow-resonance production. Additional effects, which have to be taken into account in the realistic study, increase the contribution of low energy  $\gamma\gamma$  collisions and make the high energy peak wider. Moreover, the leading order results for Compton process assume  $x = 4.8$  whereas fixed laser wave length is assumed in the present design for the whole energy range of electron beams, resulting in  $x$  parameter values smaller than the optimum value used in an “ideal” spectrum. Therefore, results obtained in this analysis, using the realistic spectra description, should not be directly compared to results obtained with “ideal” spectra.

Details of the  $W_{\gamma\gamma}$ -spectrum obtained with COMPAZ for  $\sqrt{s_{ee}} = 210$  GeV are shown in Fig. 3.5. Contributions from two polarization combinations are indicated separately, *i.e.*  $J_z = 0$  and  $|J_z| = 2$  where  $J_z$  is the total  $\gamma\gamma$  angular momentum projected on a collision ( $z$ ) axis.<sup>3</sup> The suppression of  $|J_z| = 2$  luminosity can be clearly seen in the high- $W_{\gamma\gamma}$

<sup>3</sup>The coordinate system used in this document is a right handed system, with the  $z$ -axis pointing in

part of the spectrum. The threshold at  $W_{\gamma\gamma}^{\text{max1}} = 131$  GeV, expected for collisions of two photons produced in the lowest order Compton scattering, is not sharp. There is a tail of collisions involving two photons from the second order process  $e^- + 2\gamma_L \rightarrow e^- + \gamma$  for which the highest possible energy is around 161 GeV. The intermediate structure emerges from “mixed” collisions with photons originating from different scattering processes.

If not stated explicitly otherwise, the results presented in this work are obtained for an integrated luminosity expected after one year of the TESLA Photon Collider running [56]. In Table 3.3.1 the total photon-photon luminosity per year,  $L_{\gamma\gamma}$ , is shown for different electron beam energies. Also shown are: the Higgs-boson mass corresponding to the maximum of  $J_z = 0$  luminosity spectrum for given beam energy, and the expected luminosity in the high energy part of the spectrum, *i.e.* for  $W_{\gamma\gamma} > W_{\gamma\gamma}^{\text{min}}$  where  $W_{\gamma\gamma}^{\text{min}} = 0.5 W_{\gamma\gamma}^{\text{max1}}$ .

### 3.3.2 Collision region

The  $e^-e^-$  beams used in the photon collider will have similar geometrical parameters as the  $e^+e^-$  beams of LC (they will be produced in the same damping rings, compressed by the same compression system etc.). However, beamstrahlung due to beam-beam interactions is not present and the  $e^-e^-$  beams can be focused on a smaller area at the interaction point (IP). For  $\sqrt{s_{ee}} = 200$  GeV electron bunches are assumed to have:  $\sigma_x = 140$  nm,  $\sigma_y = 6.8$  nm and  $\sigma_z = 0.3$  mm. The longitudinal ( $z$ ) photon-beam bunch size at the photon collider is approximately the same as the corresponding size of an electron bunch.

---

the direction of the electron beam in the  $e^+e^-$  mode, and the  $y$ -axis pointing upwards. The polar angle  $\theta$  and the azimuthal angle  $\phi$  are defined with respect to  $z$  and  $x$ , respectively, while  $r$  is the distance from the  $z$ -axis. When describing selection procedure the angle with respect to the beam direction is limited to  $0 \leq \theta \leq \pi/2$ .

$\sqrt{s_{ee}}$ [GeV]	$M_{higgs}$ [GeV]	$L_{\gamma\gamma}$ [fb $^{-1}$ ]	$W_{\gamma\gamma}^{\text{min}}$ [GeV]	$L_{\gamma\gamma}(W_{\gamma\gamma} > W_{\gamma\gamma}^{\text{min}})$ [fb $^{-1}$ ]
211	120	410	65	111
222	130	427	70	116
234	140	447	75	121
247	150	468	81	126
260	160	489	86	132
305	200	570	106	150
362	250	683	131	173
419	300	808	157	196
473	350	937	182	216

Table 3.2: Luminosity per year expected for the Photon Collider running at given  $\sqrt{s_{ee}}$ . One accelerator year [y] is assumed to be equal to  $10^7$  s. Also shown are: the Higgs-boson mass,  $M_{higgs}$ , corresponding to the maximum of the  $J_z = 0$  luminosity, and the expected luminosity in the high energy part of the spectrum, *i.e.* for  $W_{\gamma\gamma} > W_{\gamma\gamma}^{\text{min}}$  where  $W_{\gamma\gamma}^{\text{min}} = 0.5 W_{\gamma\gamma}^{\text{max1}}$ .

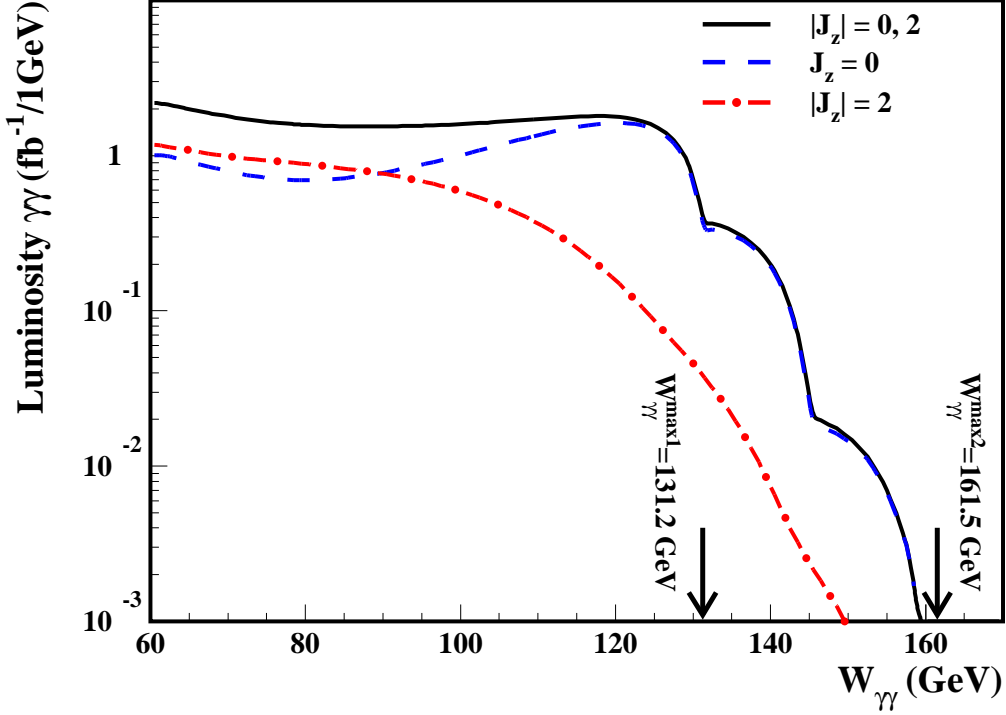


Figure 3.5: COMPАЗ parametrization of the photon-photon luminosity spectra for  $\sqrt{s_{ee}} = 210$  GeV as a function of the invariant mass of two colliding photons  $W_{\gamma\gamma}$ . The total luminosity and contributions with  $J_z=0$  and  $J_z = \pm 2$  are shown.

However, as a distance of  $b = 2.6$  mm is foreseen between CP and IP, transverse sizes of the photon bunch will be greater than that of the electron bunch due to the angular spread of the Compton scattering. This affects distribution in the  $y$  direction, as an additional spread is of the order of  $\sigma_y$ , but it does not influence the  $x$ -size of the bunch ( $\sigma_x \gg \sigma_y$ ).

For two head-on colliding bunches, which have Gaussian distribution with equal variances (and the same speed), the spacial distribution of collision probability follows 3-dimensional Gaussian distribution with all three variances two times smaller than corresponding bunch parameters, *i.e.*  $\sigma_a'^2 = \sigma_a^2/2$  ( $a = x, y, z$ ).

Transverse dimensions of a photon bunch decrease slightly with  $\sqrt{s_{ee}}$ . For  $\sqrt{s_{ee}} = 200$ -800 GeV  $x$  and  $y$  dispersions of the photon bunch are 140-70 nm and 15-5 nm, respectively. Vertical dimension of IP density,  $\sigma_y' = \sigma_y/\sqrt{2}$ , is about 10 nm or smaller, so distribution in this direction is too narrow to influence the event reconstruction and can be safely neglected. So would be the horizontal dimension  $\sigma_x'$  if the beams collided head-on. However, the crab crossing scheme results in modified collision density in the horizontal direction. This effect is schematically shown in Fig. 3.6. Assuming that beams collide with relative angle  $\alpha_c = 34$  mrad, the  $x$ -size of collision region is given by the

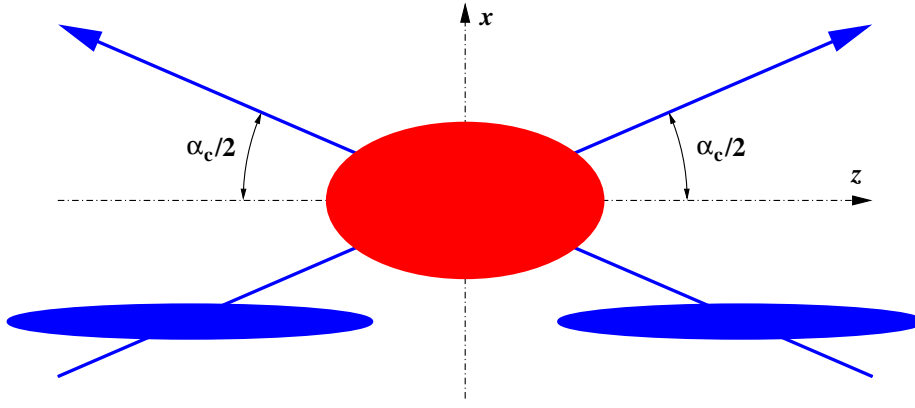


Figure 3.6: A scheme of the crab-wise bunch-bunch collision with the relative angle  $\alpha_c$  between beams. Bunches (the blue ellipses) are tilted to preserve the luminosity. The resulting primary vertex distribution, with  $\sigma'_z < \sigma_z$  and  $\sigma'_x > \sigma_x$ , is shown (the red ellipse).

following formula:

$$\sigma'_x = \sqrt{\frac{1}{2}(\sigma_x^2 + \sigma_z^2 \tan^2 \frac{\alpha_c}{2})}$$

This gives, for all considered collider energies,  $\sigma'_x \simeq 3.6 \mu\text{m}$ . This value is around 36 times greater than the spread  $\sigma_x/\sqrt{2}$  expected in case of collinear beams and comparable to the precision expected in the vertex position reconstruction. Therefore horizontal spread of the interaction point position cannot be neglected.

For the analysis presented in this thesis the longitudinal size of the collision region is most important. As this is of the order of  $100 \mu\text{m}$ , we can expect that additional tracks and clusters due to *overlaying events* (resulting in additional vertexes, changed jet characteristics etc.) can influence the flavour-tagging algorithm and affect the event selection. Therefore, generation of all event samples used in the described analysis took into account the Gaussian smearing of primary vertex with  $\sigma'_x = 3.6 \mu\text{m}$ ,  $\sigma'_y = 11 \text{ nm}$  and  $\sigma'_z = 0.21 \text{ mm}$ , and the beams crossing angle in horizontal plane,  $\alpha_c = 34 \text{ mrad}$ .

### 3.4 The detector at TESLA

The basic design of the TESLA detector for the Photon Collider is the same as for the  $e^+e^-$  TESLA mode. However, some modifications are needed due to the more complicated beam delivery system, including optical system which guides the laser beams to the conversion point. To protect detector components against the high-intensity low-angle radiation<sup>4</sup> the tungsten mask is placed between the beam system and the detector. In case of the

---

<sup>4</sup>Background arises from synchrotron radiation and from upstream or downstream sources of  $\gamma$ ,  $e^+$ ,  $e^-$  and  $n$ .

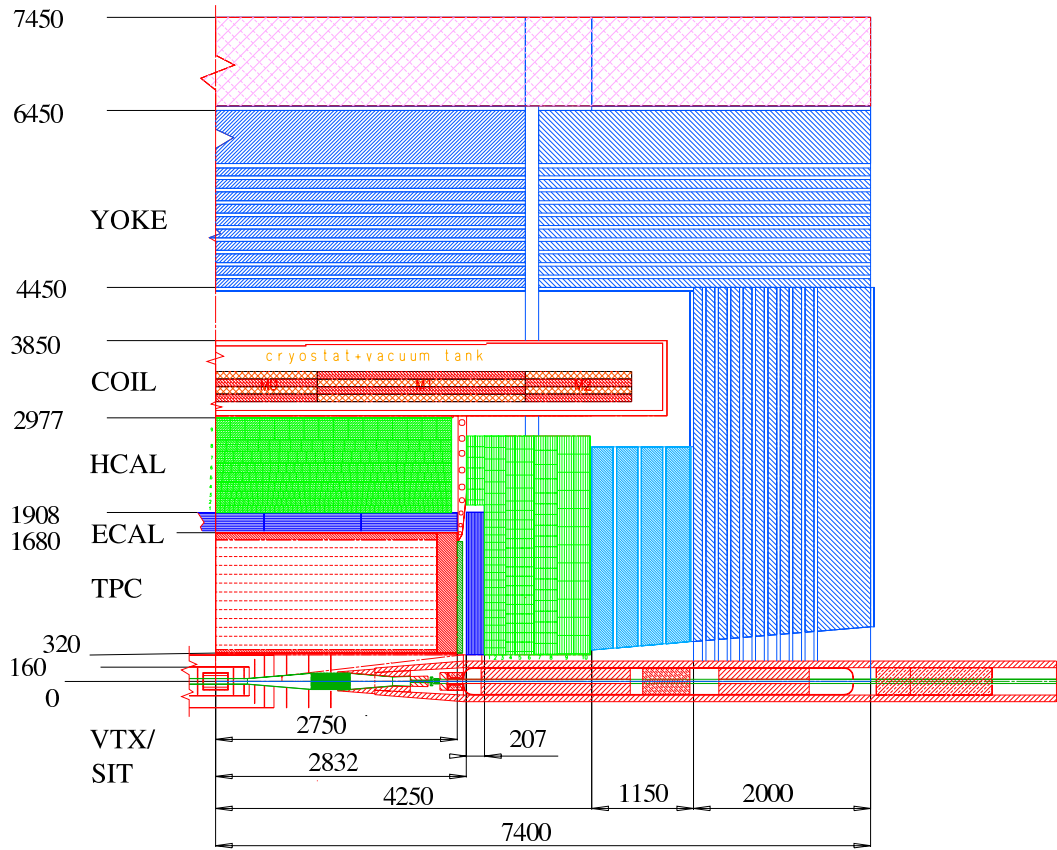


Figure 3.7: A scheme of one quadrant of the TESLA Detector [60]. Dimensions are in mm.

$e^+e^-$  collider the opening angle of the mask is  $\theta_{mask} = 83$  mrad. Particles produced at smaller angles will not enter the detector. In case of the Photon Collider the value of  $\theta_{mask} = 130$  mrad ( $7.5^\circ$ ) has been chosen as more space is required for optical system and beams removal. This results in moderate loss of hermeticity in comparison with the  $e^+e^-$ -detector. Moreover, in case of the  $e^+e^-$ -detector two forward calorimeters (Low Angle Tagger and Low Angle Calorimeter) are foreseen which together cover the region down to around 5 mrad. These components will not be installed in the Photon Collider option.

In the following, main components of the detector for the Photon Collider are described. The description is based on the TESLA Technical Design Report (TDR) [60] and the manual for the fast-simulation program SIMDET [61]. For many detector components different choices of technology and/or design were considered in the TDR. We discuss only these solutions which have been implemented in the SIMDET program and can be used to simulate the response of the detector. Because all proposed designs are expected to fulfill performance standards described in the TDR one can assume that our physical results should not worsen if alternative designs of the considered subdetectors are included in the final project.

The schematic view of the TESLA detector is shown in Fig. 3.7. The detector closest to the interaction point is a multi-layer microvertex detector with a total length of around 30 cm. Currently at least two technologies are considered for this detector: charge-coupled devices (CCD) and active pixel sensors (APS). In this work the CCD-based option is used. It has well-defined geometry, material budget and the highest established performance in terms of precision over a wide range of incident angles (for devices of the dimensions needed for this application, *i.e.* tens of cm<sup>2</sup>), and only for this version the fast-simulation program provides a parametrized track covariance matrix which is crucial for the realistic flavour tagging simulation. With this design precision of the position measurement of 3.5  $\mu\text{m}$  can be achieved.<sup>5</sup> To obtain a good reconstruction efficiency at least three detector layers are proposed so that, together with the silicon tracking subsystem (SIT), at least five silicon layers inside the TPC are available.

In addition to the vertex detector a tracker system consists of intermediate silicon tracking detectors (SIT), a large Time Projection Chamber (TPC) and forward chambers. Silicon tracking subsystem includes cylinders in the barrel (SIT) and disks in the forward region (FTD). In the barrel region two layers of silicon strip detectors cover the region down to  $\theta = 25^\circ$ . One of the cylinders, at  $r = 16$  cm, improves the track reconstruction efficiency mostly for long-lived particles which decay outside the vertex detector. Three pixel and four strip silicon detectors with point resolutions of 10  $\mu\text{m}$  and 50  $\mu\text{m}$ , respectively are placed on each side, in the forward region (the endcaps). The main role of these detectors is to improve the momentum resolution for tracks by adding a few very precise space points at comparatively large distance from the primary interaction point, and to help the pattern recognition in linking the tracks found in the TPC with tracks found in the vertex detector.

The central tracking system consists of two gas-filled chambers: a large volume time projection chamber (TPC) and a precise forward tracking chamber (FCH) located between the TPC endplate and the endcap calorimeter. The TPC, with 200 readout points in the radial direction ( $r = 32\text{--}170$  cm), provides a very precise measurement of a track curvature, which is used in the determination of particle momentum. Because of the high magnetic field of 4 T the minimal transverse momenta of a particle required to enter and traverse the TPC are around 200 MeV and 1 GeV, respectively, if the particle charge is equal to the electron charge. Precise measurement of the specific energy loss in the TPC can be also used for particle identification. For tracks traversing the TPC at large polar angles the expected errors on the transverse momentum and the energy loss measurements are  $\sigma(1/p_T) \approx 0.02\%/ \text{GeV}$  and  $\sigma(dE/dx)/dE/dx \approx 5\%$ , respectively. For example, in case of a charged particle with energy of 20 GeV at the polar angle of  $90^\circ$  the

---

<sup>5</sup>CCD vertex design implemented in SIMDET assumes the radius of the innermost layer of 1.5 cm, which is the optimum choice for  $e^+e^-$  based on the background considerations. In case of the Photon Collider the inner radius of the vertex detector will probably have to be increased to about 2 cm.



momentum resolution is about 80 MeV. From ionisation losses the separation of kaons and pions should be possible in the momentum range from 2 to 20 GeV. Electron identification will be improved compared to what can be done with calorimeters alone, especially for low momenta ( $p \lesssim 3$  GeV) where calorimetric identification is difficult.

Overall tracking system performance, when the track parameters are determined from combining vertex detector, SIT and TPC measurements, shows a very high precision of transverse momentum determination  $\sigma(1/p_T) \leq 0.005\%/GeV$  if systematic errors  $\leq 10 \mu m$  for point position measurements are achieved. It is worth noticing that the overall momentum-resolution has been improved by about 30% by adding a cylindrical silicon detector (SIT) inside the TPC, *i.e.* at  $r = 30$  cm.

A tracking electromagnetic calorimeter (ECAL), build of tungsten absorber plates and thin silicon sensors, is placed behind the TPC. The expected energy resolution  $\sigma_E/E$  is around 11–14%/ $\sqrt{E/GeV}$ , depending slightly on the energy. The project assumes very high 3D granularity of this detector, allowing measurement of the particle momentum direction. A hadronic calorimeter (HCAL) is an iron/scintillating tile calorimeter with fine transverse and longitudinal segmentations. The energy resolution for single hadrons, estimated from simulation of hadronic showers in both calorimeters (HCAL+ECAL), is<sup>6</sup>  $\sigma_E/E = 35\%/ \sqrt{E/GeV} \oplus 3\%$ .

A large superconducting coil, 6 m in diameter, produces a field of 4 T with very high uniformity ( $\leq 10^{-3}$ ). The coil is placed behind calorimeters to preserve high precision of energy measurement, reducing the amount of inactive material in front of the calorimeters. The iron return yoke serves also as a muon “separator”, absorbing other particles escaping from the HCAL.

For muon chambers, which are placed inside the yoke and behind it, resistive plate chamber (RPC) technology is considered. Although the basic task for a muon detector is to identify muons, it is also possible to use the inner muon chambers as the “tail catcher”, *i.e.* to detect hadronic cascades which are not fully contained in the hadronic calorimeter. Full efficiency of muon identification is reached for muons with energy above 5 GeV.

The total length and the diameter of the detector will be around 15 m each. In general, the detector is designed to measure particles properties with a very high accuracy in the collision energy range from about 90 GeV up to 1 TeV. Electrons below 150 GeV, muons and charged hadrons are best measured in the tracking detectors. Electrons above 150 GeV and photons by the electromagnetic calorimeter and neutral long-living hadrons by the combined response of the electromagnetic and hadronic calorimeters. In the event reconstruction the so-called energy-flow technique will be used which combines the information from tracking system and calorimeter to obtain the optimal estimate of the energy flow of produced particles and of the original parton four-momenta. For the energy-flow

---

<sup>6</sup>The operator  $\oplus$  means “adding in quadrature”:  $a \oplus b \equiv \sqrt{a^2 + b^2}$

objects an average energy resolution of  $\sigma_E/E \simeq 30\%/\sqrt{E/\text{GeV}}$  is expected.

Due to the sparse beam structure (a long time interval of 199 ms between two bunch trains, a separation of two bunches inside a train by 337 ns, a train length of 950  $\mu\text{s}$ ) no hardware trigger is foreseen. A total data volume of roughly 300 TByte per year will be stored for physical analyses.

### 3.4.1 Simulation setup

The fast simulation program for the TESLA detector, SIMDET version 4.01 [61], was used to model the detector performance. All detector components are implemented in the program according to the TESLA TDR. Parametrizations based on the full simulation of detector performance with the BRAHMS program [62] are used to describe energy and angular resolutions. The track reconstruction efficiency and charge misinterpretation probability are momentum dependent. An energy-flow algorithm is used to link information from tracking system and calorimeters. In the first stage energy deposits in the calorimeters are joined into clusters. Then energy flow objects are defined by linking clusters with tracks reconstructed in the tracking system<sup>7</sup>. For the reconstructed particle tracks a track covariance matrix is calculated in the base:  $xy, z, \theta, \phi, 1/p_T$ .

Because two forward calorimeters, Low Angle Tagger and Low Angle Calorimeter, cannot be installed in the detector at the PC, they are not used in our simulation setup. Also the information about energy loss measured in the TPC, which is not properly simulated yet, is not used for particle identification. Instead, an appropriate misidentification probability is assumed for each particle species.

Within the current SIMDET version it is not yet possible to set a wider opening angle of the forward mask as required for the Photon Collider. To take the modified mask setup into account all generator-level particles are removed from the event record, before entering the detector simulation, if their polar angle is less than  $\theta_{mask} = 130 \text{ mrad}$ .

---

<sup>7</sup>In the current SIMDET version the idealised pattern recognition is still used, *i.e.* clusters are linked with tracks relying on the information about originally generated particles.

# Chapter 4

## Signal and background

In this Chapter the signal and background processes, and methods used in their simulation are described. The signal of the Higgs-boson production considered in this thesis is the process  $\gamma\gamma \rightarrow higgs \rightarrow b\bar{b}$ , whereas the main background processes are  $\gamma\gamma \rightarrow b\bar{b}$  and  $\gamma\gamma \rightarrow c\bar{c}$ . The  $b\bar{b}$  pair production is an irreducible background which can be suppressed only by kinematic cuts. The  $c\bar{c}$  pair production contributes to the background due to the finite probability of being tagged as the  $b\bar{b}$  pair production. Background contributions from light quark and tau pair production,  $\gamma\gamma \rightarrow q\bar{q}/\tau^+\tau^-$  ( $q = u, d, s$ ), are also considered. The process  $\gamma\gamma \rightarrow hadrons$  is described in detail due to its contribution to *overlying events*. For heavy Higgs bosons,  $M_{higgs} \gtrsim 160$  GeV, also the process  $\gamma\gamma \rightarrow W^+W^-$  is taken into account. The underlying statistical principles used to describe the possibility of having more than one collision in single bunch crossing, and used in generation of the overlaying events are described in Appendix A.

### 4.1 Signal processes

As the Higgs boson is a spinless particle, the distribution of its two-body decay products is uniform in the three-dimensional space (in the Higgs-boson rest frame). In spherical coordinates the distribution is uniform in  $\cos\theta^*$  and  $\phi^*$ , where  $\theta^*$  and  $\phi^*$  are polar and azimuthal angle, respectively. In the Photon Collider *higgs* will be produced in collisions of photons which will have, in general, different energies. Thus, the center of mass system will be boosted with respect to the laboratory frame, resulting in a non-uniform distribution in  $\cos\theta$ , where  $\theta$  is the polar angle in the laboratory frame. However, as already mentioned in section 3.3.1, energy of the electron beam is assumed to be tuned for the highest resonance production rate. It means that most collisions will involve two photons with high and similar energies as in all considered cases the resonance is narrow (the total width,  $\Gamma_{higgs}$ , is much smaller than the width of the  $W_{\gamma\gamma}$ -distribution in the high energy part). Consequently, the Higgs boson will have small longitudinal momentum in comparison to

Symbol	$\mu$ [GeV]	$M_2$ [GeV]	$A_{\tilde{f}}$ [GeV]	$M_{\tilde{f}}$ [GeV]
<i>I</i>	200	200	1500	1000
<i>II</i>	-150	200	1500	1000
<i>III</i>	-200	200	1500	1000
<i>IV</i>	300	200	2450	1000

Table 4.1: MSSM parameter sets used in the described analysis.

the mass, and its decays will be nearly isotropic also in the laboratory frame.

Total widths and branching ratios of the Higgs bosons were calculated with the program HDECAY [70] (version 3.0), where higher order QCD corrections are included. The mass of the top quark equal to 174 GeV was assumed. The contributions from the decay  $higgs \rightarrow gg^* \rightarrow gb\bar{b}$  were not added to the branching ratio  $BR(higgs \rightarrow b\bar{b})$  as the kinematical characteristic of such events is different from the direct decay to the  $b\bar{b}$  pair.<sup>1</sup> For the considered mass range between 120 and 160 GeV the total width of the SM Higgs boson increases from about 3.6 to 77 MeV, and its branching ratios  $BR(h \rightarrow \gamma\gamma)$  and  $BR(h \rightarrow b\bar{b})$  decrease from 0.22% to 0.06% and from 68% to 4%, respectively, in the mass

Event generation for Higgs-boson production process was done with the PYTHIA program [71]. A parton shower algorithm implemented in PYTHIA was used to generate the final-state partons. The fragmentation into hadrons was also performed using the PYTHIA program, both for Higgs-boson production and for all background event samples.

In case of the MSSM Higgs-boson production the analysis has been developed assuming MSSM parameters similar to these used in [24], *i.e.*  $\tan\beta = 7$ ,  $\mu = \pm 200$  GeV and  $M_2 = 200$  GeV, taking into account decays to and loops of supersymmetric particles. The parameter value  $\tan\beta = 7$  is used in the event generation and obtained results are rescaled to the parameter range  $\tan\beta = 3 - 20$ . In the following, parameter sets from [24] will be denoted as *I* and *III*, see Tab. 4.1. Only the values of trilinear couplings are changed (from  $A_{\tilde{f}} = 0$  to  $A_{\tilde{f}} = 1500$  GeV), so that the mass of the lightest Higgs boson, instead of being around 105 GeV (for  $\tan\beta = 4$  and  $M_A = 300$  GeV) is above the current lower limit for the SM Higgs boson,  $M_h > 114.4$  GeV. Results for heavy neutral Higgs bosons are the same as for parameter sets proposed in [24]. The intermediate scenario *II* with  $\mu = -150$  GeV is also considered. For comparison with predictions presented by LHC experiments, the scenario *IV* used in [8] is also included. In all cases the common sfermion mass equal to 1 TeV was assumed. We have checked that all parameter sets imply masses of neutralinos, charginos, sleptons and squarks higher than current experimental limits.

---

<sup>1</sup>Inclusion of the decay  $higgs \rightarrow gg^* \rightarrow gb\bar{b}$  does not change the results of this analysis as  $BR(h \rightarrow b\bar{b})$  increases only by around 1% for the SM case, and for considered MSSM parameters  $BR(A/H \rightarrow gg)/BR(A/H \rightarrow b\bar{b}) \lesssim 1\%$ . However, if events with only one  $b$ -tagged jet were accepted, one would have to use inclusive branching ratio  $BR(h \rightarrow b\bar{b} + \dots)$ , measured at the  $e^+e^-$  LC, to obtain final results for  $\Gamma(h \rightarrow \gamma\gamma)$ .

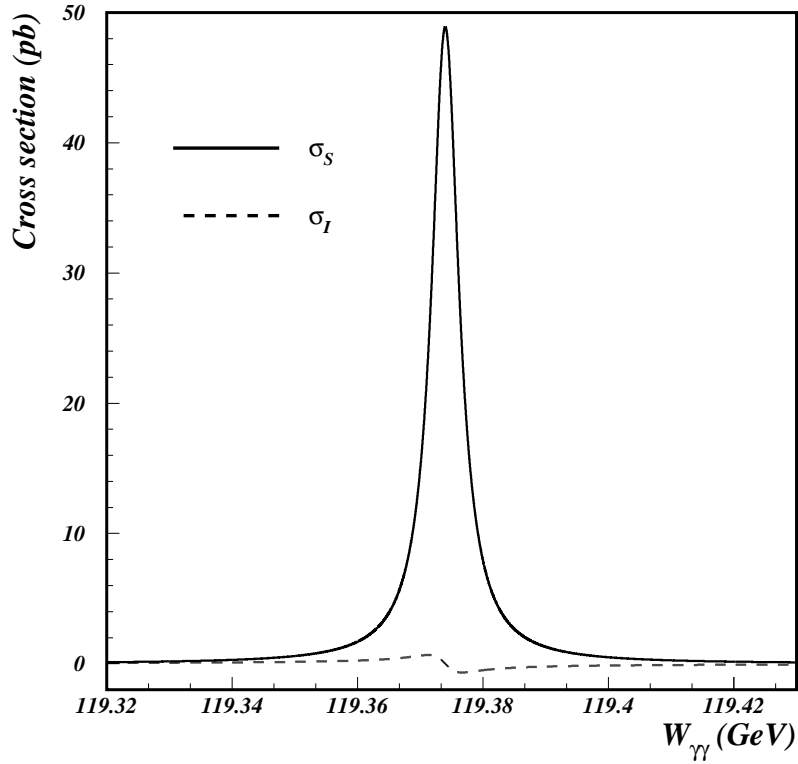


Figure 4.1: The total cross section for process  $\gamma\gamma \rightarrow h \rightarrow b\bar{b}$  for set I of the MSSM parameters values (see text) with  $M_A = 300$  GeV and  $\tan\beta = 7$ . The signal only,  $\sigma_S$ , and interference part,  $\sigma_I$ , are shown separately. As the other neutral Higgs bosons are narrow and heavy, they do not influence the  $h$  cross section.

For the wide range of parameter values the heavy neutral Higgs bosons,  $A$  and  $H$ , are nearly mass degenerate. The mass difference  $M_H - M_A$  decreases with increasing  $\tan\beta$  and  $M_A$  and is similar for all considered parameter sets. For  $M_A = 200$  GeV the mass difference decreases from  $M_H - M_A \approx 12$  GeV for  $\tan\beta = 3$  to 0.7 GeV for  $\tan\beta = 15$ . If  $M_A = 350$  GeV, the corresponding values are 6 GeV and 0.3 GeV. The mass difference is larger or comparable to the total widths of  $A$  and  $H$  which vary between 50 MeV and 4 GeV. The branching ratios relevant for this study change between 3% and 90% for  $\text{BR}(A/H \rightarrow b\bar{b})$ , and from  $2 \cdot 10^{-7}$  to  $9 \cdot 10^{-5}$  for  $\text{BR}(A/H \rightarrow \gamma\gamma)$ .

Processes  $\gamma\gamma \rightarrow H \rightarrow b\bar{b}$  and  $\gamma\gamma \rightarrow A \rightarrow b\bar{b}$  do not interfere<sup>2</sup> (*e.g.* see [22] eq. 3.15), and  $h - H$  interference is negligible due to the large difference in masses and relatively small widths of the bosons. Therefore total  $\gamma\gamma \rightarrow A, H \rightarrow b\bar{b}$  production rate is equal to the sum of both contributions.

However, for the complete description of the Higgs boson production we also have to

---

<sup>2</sup>Although in general case two processes with  $A$  and  $H$  in the intermediate state (different  $CP$  quantum numbers) can interfere. For example, there is interference between chargino production processes in  $\gamma\gamma$  collisions via  $A$  and  $H$ :  $\gamma\gamma \rightarrow A, H \rightarrow \tilde{\chi}_i^+ \tilde{\chi}_j^-$  (*e.g.* see [22] eq. 3.59).

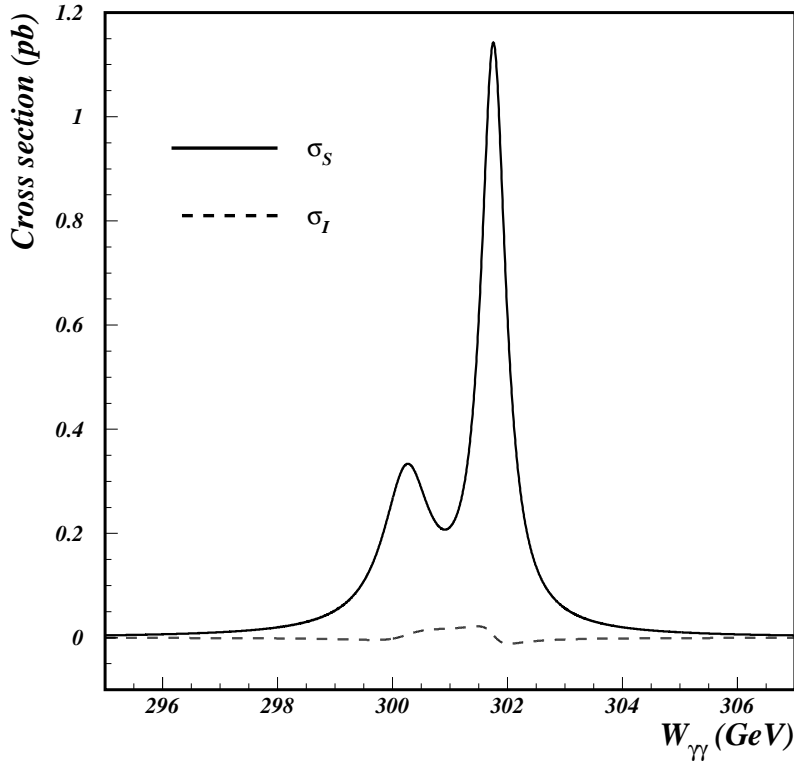


Figure 4.2: The total cross section for process  $\gamma\gamma \rightarrow A, H \rightarrow b\bar{b}$  for set I of the MSSM parameters values (see text) with  $M_A = 300$  GeV and  $\tan\beta = 7$ . The signal only,  $\sigma_S$ , and interference part,  $\sigma_I$ , are shown separately. As the light Higgs boson,  $h$ , has mass of around 120 GeV and is narrow, it does not influence the  $A, H$  cross section.

consider the interference between  $\gamma\gamma \rightarrow higgs \rightarrow b\bar{b}$  and non-resonant  $\gamma\gamma \rightarrow b\bar{b}$  production processes. The LO interference terms for  $h$  and  $H/A$  production are shown in Fig. 4.1 and 4.2, together with the signal cross sections  $\gamma\gamma \rightarrow h \rightarrow b\bar{b}$  and  $\gamma\gamma \rightarrow A, H \rightarrow b\bar{b}$ . For all considered cases these terms are proportional to the real part of the propagator:

$$\Re \frac{M^2}{s - M^2 + BM\Gamma} = \frac{M^2(s - M^2)}{(s - M^2)^2 + (M\Gamma)^2}$$

As on average (the integral over  $W_{\gamma\gamma} = \sqrt{s}$ ) this expression is near to zero for small  $\Gamma$  (of the order of  $\Gamma/M$ ), the interference contribution can be safely neglected. However, as discussed in the next section, the NLO corrections substantially modify predictions for heavy quark production. The NLO corrections for interference term were calculated in [22]. As described in [22], after selection cuts the interference term was below the level of  $10^{-3}$  of the signal. Although selection cuts were different than in our analysis, we can infer the total correction factor. The cuts decrease interference contribution by the order of magnitude and the signal rate by about 50%. Thus, one can estimate that the

interference part contributes no more than 1% of the total signal cross section. Because this is smaller than other uncertainties, we neglect the interference term in this analysis.

## 4.2 Heavy quark production background

The main background for the considered signal process,  $\gamma\gamma \rightarrow higgs \rightarrow b\bar{b}$ , is the heavy quark-pair production. An irreducible background consists of events with the  $b\bar{b}(g)$  final state, resulting from 'direct' nonresonant  $b\bar{b}$  production,  $\gamma\gamma \rightarrow b\bar{b}$ . In LO approximation the cross section for  $J_z = 0$  is suppressed and the dominant contribution is due to the  $|J_z| = 2$  state. This is very fortunate as the  $\gamma\gamma$ -luminosity spectrum is optimized to give highest  $J_z = 0$  luminosity and the  $|J_z| = 2$  component is small in the *higgs*-production region. Unfortunately, NLO corrections compensate partially the  $m_Q^2/s$ -suppression and, after taking into account luminosity spectra, both contributions (for  $J_z = 0$  and  $|J_z| = 2$ ) become comparable. The extensive comparison of NLO and LO results can be found for example in our work [27].

The other processes  $\gamma\gamma \rightarrow q\bar{q}(g)$ , where  $q = u, d, s, c$ , contribute to the reducible background. However, one has to consider these processes due to the non-zero probability of wrong flavour assignment in reconstruction (impurity of flavour-tagging). Events with  $c\bar{c}(g)$  in the final state have the highest mistagging probability. In comparison to the  $\gamma\gamma \rightarrow b\bar{b}$  process there is an enhancement factor of  $(e_c/e_b)^4 = 16$  in the  $\gamma\gamma \rightarrow c\bar{c}$  cross section. It turns out that after flavour tagging both processes give similar contribution to the background.

The background events due to processes  $\gamma\gamma \rightarrow b\bar{b}(g)$ ,  $c\bar{c}(g)$  were generated using the program written by G. Jikia [23], where a complete NLO QCD calculation for the production of massive quarks is performed in the massive-quark scheme. The program includes exact one-loop QCD corrections to the lowest order processes  $\gamma\gamma \rightarrow b\bar{b}$ ,  $c\bar{c}$  [17], and the non-Sudakov form factor in the double-logarithmic approximation, calculated up to four loops [21]. Events generated with NLO QCD program were transferred to PYTHIA program for hadronisation. To avoid double-counting of corrections due to real gluon emission, the parton shower algorithm was not applied. However, to estimate the influence of higher order corrections on the event selection efficiency we also prepared dedicated samples of  $\gamma\gamma \rightarrow b\bar{b}(g)$ ,  $c\bar{c}(g)$  events with parton shower included. Results of this comparison are presented in Appendix B.

## 4.3 Other background processes

In cases of the SM Higgs-boson production for  $M_h = 150$  and 160 GeV, and in the analysis of heavy neutral Higgs-bosons in the MSSM also the pair production of  $W$  bosons,

$\gamma\gamma \rightarrow W^+W^-$ , is considered as a possible background. The cross section for this process is very high for large  $W_{\gamma\gamma}$ , and it can contribute to the background if the event is clustered to two or three jets and at least one of these jets is  $b$ -tagged. This can be the case if two jets from hadronic  $W$  decays are merged together by the jet-clustering algorithm, or if some jets are ignored in the analysis because they are too close to the beam pipe. For generation of  $\gamma\gamma \rightarrow W^+W^-$  events the PYTHIA program is used. However, as only unpolarized cross section for this process is implemented in PYTHIA, we use polarized differential cross section formulae from [63] to obtain correct distributions for  $J_z = 0$  and  $|J_z| = 2$  contributions.

As there is non-zero probability of mistagging a light-quark jet as a  $b$ -jet, the process  $\gamma\gamma \rightarrow q\bar{q}$ , where  $q = u, d, s$ , is also taken into account as a possible background. Due to the strong dependence of the cross section for this process on the fermion charge ( $\sigma \sim e_f^4$ ), the  $\gamma\gamma \rightarrow u\bar{u}$  contribution dominates. The event generation is performed with PYTHIA using unpolarized LO cross section. We know that for  $J_z = 0$  the LO cross section for the process  $\gamma\gamma \rightarrow q\bar{q}$  is equal to zero for massless quarks. By convoluting the cross section for  $|J_z| = 2$  with the total luminosity spectrum (modulo factor 2) we overestimate the light quark production background. Comparing results for  $\gamma\gamma \rightarrow c\bar{c}(g)$  and  $\gamma\gamma \rightarrow u\bar{u}$  we have determined that the number of events with light quark-pair production is overestimated by a factor of about 2.6 for our SM analysis, and by a factor of about 4 for our MSSM analysis. We do not apply any corrections to decrease this effect. In the analysis of SM Higgs-boson production the light-quark contribution is negligible and does not change the results. In case of MSSM Higgs-boson production we use the overestimated contribution of  $\gamma\gamma \rightarrow q\bar{q}$ ,  $q = u, d, s$ , events to effectively take into account the contribution of  $\gamma\gamma \rightarrow \text{hadrons}$  events (without *direct* $\times$ *direct* interactions) from which no generated events passed all selection cuts. We estimated that in the mass window optimal for the cross-section measurement (see Chapters 5 and 6) the contribution of  $\gamma\gamma \rightarrow \text{hadrons}$  events would correspond to about 50% of the (overestimated) light-quark contribution.

A large number of  $\tau$ -pair production events will also be observed in the Photon Collider (the cross section about 1.7 times higher than the LO cross section for  $\gamma\gamma \rightarrow c\bar{c}$ ). Thus, even small  $\tau$  mistagging probability could in principle significantly influence our results. Fortunately, the  $J_z = 0$  contribution is negligible in this case due to the  $m_\tau^2/s$ -suppression (QED higher order corrections are small). In addition, considerable amount of energy is carried out by neutrinos. Consequently, the number of  $\tau^+\tau^-$  events reconstructed as two-jet events with high invariant mass should be very small. For this study  $\gamma\gamma \rightarrow \tau^+\tau^-$  production events were generated with PYTHIA using polarized cross section.



## 4.4 Overlaying events $\gamma\gamma \rightarrow \text{hadrons}$

Because of the large cross section and huge  $\gamma\gamma$ -luminosity at low  $W_{\gamma\gamma}$ , from one to two  $\gamma\gamma \rightarrow \text{hadrons}$  events<sup>3</sup> are expected at the TESLA Photon Collider per bunch crossing. These events hardly contribute to the background on their own. However, they can have a great impact on the reconstruction of other events produced in the same bunch crossing, by changing their kinematical and topological characteristics.

We generate  $\gamma\gamma \rightarrow \text{hadrons}$  events with PYTHIA, using the luminosity spectra from a full simulation of the photon-photon collisions [56], rescaled to the chosen beam energy. For each considered  $e^-e^-$  energy,  $\sqrt{s_{ee}}$ , an average number of the  $\gamma\gamma \rightarrow \text{hadrons}$  events per bunch crossing is calculated. Then, for every signal or background event, the  $\gamma\gamma \rightarrow \text{hadrons}$  events are overlaid (added to the event record) according to the Poisson distribution. In Appendix A principles of event generation and approximations used are discussed in detail.

The  $\gamma\gamma \rightarrow \text{hadrons}$  processes are classified according to the type of photon(s) interaction. If both photons interact as point-like, as described by QED, then we call the process *direct* $\times$ *direct*. However, if one or two photons interact as a hadronic state (vector meson or quantum fluctuation with gluons), then they are denoted as *hadron-like* $\times$ *direct* or *hadron-like* $\times$ *hadron-like*, respectively. As shown in Fig. 4.3 the biggest contribution to the cross section is due to processes with *hadron-like* $\times$ *hadron-like* photons. Fortunately, the  $\gamma\gamma \rightarrow \text{hadrons}$  cross section is very forward-peaked as seen in Fig. 4.4. A cut on the polar angle of tracks and clusters measured in the detector should greatly reduce contribution of particles from  $\gamma\gamma \rightarrow \text{hadrons}$  processes to selected events. Events with  $\gamma\gamma \rightarrow \text{hadrons}$  interactions only, without *direct* $\times$ *direct* interactions, are simulated as well. Such events can mimic signal if two or more of them are overlaid. As the generation of high-energy  $\gamma\gamma \rightarrow \text{hadrons}$  events with significant transverse energy is very inefficient, these events are included only in the SM analysis. In case of MSSM analysis we have estimated the contribution of  $\gamma\gamma \rightarrow \text{hadrons}$  events, and include it effectively as the part of light quark-pair production (see previous Section).

For more details concerning  $\gamma\gamma \rightarrow \text{hadrons}$  overlaying events and their influence on the reconstruction see Appendix C. The package ORLOP, created for including the  $\gamma\gamma \rightarrow \text{hadrons}$  events by the generation of hard  $\gamma\gamma$  scattering processes, is described in Appendix D.

---

<sup>3</sup>For technical reasons we consider only photon-photon events with  $W_{\gamma\gamma} > 4$  GeV. However, events with lower  $W_{\gamma\gamma}$  are mostly produced with high boost and particles going at very small angles do not enter the detector. For further detailed discussion see Appendix C.

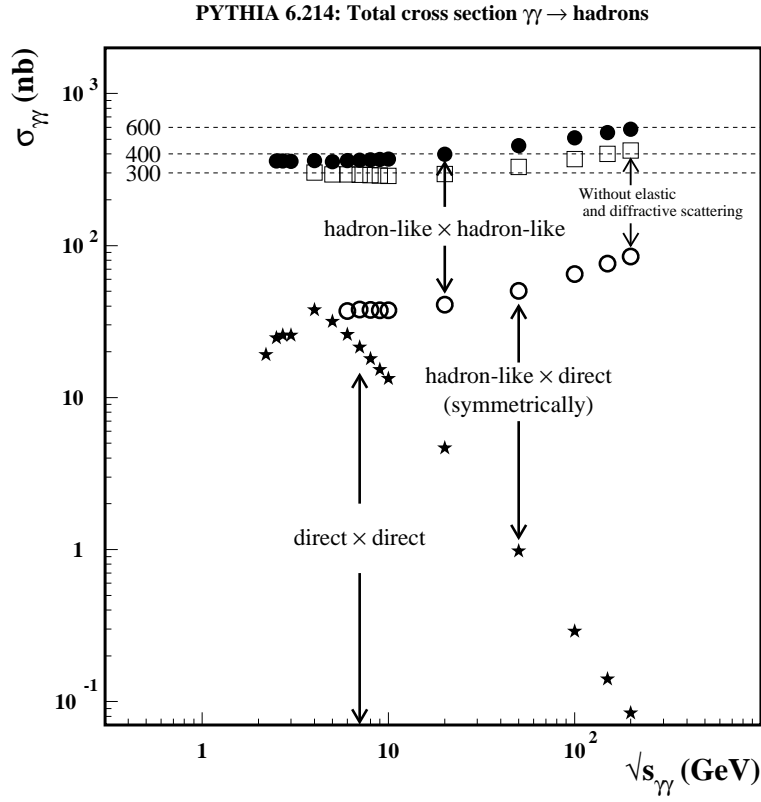


Figure 4.3: Cross sections for the process  $\gamma\gamma \rightarrow \text{hadrons}$  obtained with the PYTHIA program. Contributions from various event classes are indicated. Also the magnitude of the cross section for elastic and diffractive processes is indicated.

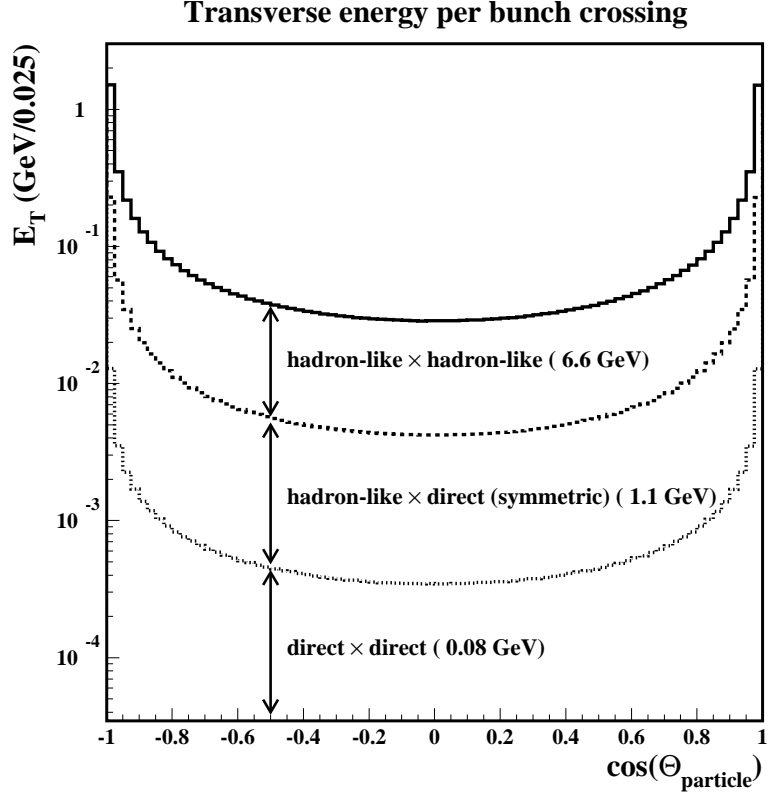


Figure 4.4: Angular distributions of the transverse energy flow,  $E_T$ , for overlaying events  $\gamma\gamma \rightarrow \text{hadrons}$  per bunch crossing. Various components and their total contributions (numbers in parentheses) are indicated. PYTHIA generation results with luminosity spectrum for  $\sqrt{s_{ee}} = 210.5$  GeV.



# Chapter 5

## Standard Model Higgs-boson production

In this Chapter the measurement of the Standard Model Higgs-boson production cross section at the TESLA Photon Collider is discussed. Following steps of the analysis are described: selection of energy-flow objects, jet reconstruction, kinematical and topological selection cuts optimized for cross section measurement, and the role of  $b$ -tagging in selection of signal events. To simplify the description, the analysis is presented in detail for the Higgs-boson mass  $M_h = 120$  GeV. For other considered masses of the Higgs boson,  $M_h = 130, 140, 150$  and  $160$  GeV, the same procedure was performed with independent optimization of selection thresholds. The cuts dedicated to suppress  $\gamma\gamma \rightarrow W^+W^-$  background, which is not relevant for lower Higgs-boson masses, are described for  $M_h = 160$  GeV. Expected precisions of the measurement obtained in this analysis are compared with results of our earlier works in which some of experimental aspects and background contributions considered here were not yet taken into account.

### 5.1 Preselection of energy-flow objects and jet reconstruction

In the energy range  $\sqrt{s_{ee}} = 210\text{--}260$  GeV about one  $\gamma\gamma \rightarrow \textit{hadrons}$  event takes place on average at each bunch crossing. The contribution from these overlaying events is expected to affect observed particle and energy flow mainly at low polar angles (see Section 4.4). Therefore, we introduce an angle  $\theta_{TC}$  defining the region strongly contaminated by this contribution; tracks and clusters with polar angle less than  $\theta_{TC}$  are not taken into account when applying energy-flow algorithm. In spite of that energy-flow objects with polar angle less than  $\theta_{TC}$  can still be formed; they are also ignored in further steps of analysis. A few values of  $\theta_{TC}$  were considered in the analysis as discussed in detail in Appendix C. We

decided to use the value  $\theta_{TC} = 0.85$  as with this choice almost the whole contribution from hadron-like photon interactions is suppressed and distributions of jet transverse momentum and jet mass are similar to those obtained without overlaying events and without  $\theta_{TC}$  cut. It was checked that  $\theta_{TC} = 0.85$  results also in the best final cross section measurement precision.

For the signal process considered in this analysis we expect that the produced partonic state is well reproduced by jets reconstructed from energy-flow objects. In the presented study jets are reconstructed using the Durham algorithm [64] where the distance measure between two jets,  $i$  and  $j$ , is defined as

$$y_{ij} = 2 \min(E_i^2, E_j^2)(1 - \cos \theta_{ij})/E^2;$$

$E_i$  and  $E_j$  are energies of jets,  $\theta_{ij}$  is the relative angle between jets and  $E$  is the total energy measured in the detector. The list of energy-flow objects reconstructed in the detector is used as the input to the algorithm, assuming that each energy-flow object is a jet. In following steps a pair of jets which has the smallest value of  $y_{ij}$  is searched for and these two jets are merged into one jet. The algorithm terminates when all possible values of  $y_{ij}$  are greater than the value of the cut-off parameter,  $y_{cut}$ . The choice of the distance measure  $y_{ij}$  and of the parameter  $y_{cut}$  value used in this analysis is based on the approach adopted in the NLO QCD [23] program which is used for generation of background events  $\gamma\gamma \rightarrow Q\bar{Q}(g)$ . In this program the real gluon emission is considered only for  $y_{qg} > 0.01$ . Soft gluon emissions, *i.e.* emissions with  $y_{qg} \leq 0.01$ , are absorbed in the cross-section calculation for  $Q\bar{Q}$  final state. For consistency with this approach jets have to be reconstructed with  $y_{cut} > 0.01$ , as for lower  $y_{cut}$  values additional jets expected from soft-gluons emission would not be described by the generator. Moreover, the distance measure used in the NLO generator is calculated using true values of kinematic variables and is inversely proportional to the  $\gamma\gamma$  invariant mass squared,  $y_{ij}^{gen} \propto 1/s_{\gamma\gamma}$ , whereas the visible energy is used in the jet reconstruction,  $y_{ij} \propto 1/E^2$ . In the significant fraction of events we expect that due to detector acceptance  $E^2 < s_{\gamma\gamma}$ . Therefore, the value  $y_{cut} = 0.02$ , two times larger than the one used in generator, has been chosen. With this value, reconstructed jets can be relatively wide. For example, two perpendicular jets will be joined together if one of them has energy of 12 GeV or below (assuming  $E \approx 120$  GeV, most probable value for  $M_h = 120$  GeV).

As the NLO QCD generator does not include additional gluon emissions due to higher order corrections, we study the resulting systematic uncertainty of the result, by applying the parton shower algorithm to the NLO heavy quark background events. Although some gluon contributions are double counted in such procedure, it allows us to determine the sensitivity of the analysis to the higher order corrections. Results are presented in

## Appendix B.

To correct for the non-zero beam crossing angle, all reconstructed jets are transformed from the laboratory frame to the frame moving with the speed factor  $\beta = \sin \frac{\alpha_c}{2} \approx \frac{\alpha_c}{2} = 0.017$  in the  $x$  direction, where  $\alpha_c$  is the beam crossing angle. After this correction the average value of the measured transverse momentum in the horizontal direction,  $P_x$ , is zero.

## 5.2 Kinematical and topological cuts

The first cut applied after detector simulation is introduced to exclude possible influence of the cut  $W_{\gamma\gamma}^{\min}$ , the lower limit on the  $\gamma\gamma$  invariant mass, used in the event generation. Therefore, the condition  $W_{rec} > 1.2 W_{\gamma\gamma}^{\min}$  is imposed for all considered events, where  $W_{rec}$  is the total reconstructed invariant mass of the event (calculated from all energy-flow objects above  $\theta_{TC}$ ).

Higgs-boson decay events are expected to consist mainly of two  $b$ -tagged jets with large transverse momentum and nearly isotropic distribution of the jet directions. The significant number of events ( $\sim 25\%$ ) contains the third jet due to the real gluon emissions which are approximated in this analysis by the parton shower algorithm, as implemented in the PYTHIA.

The following cuts are used to select properly reconstructed  $b\bar{b}$  events coming from Higgs decay.

1. Number of selected jets should be 2 or 3. In addition to two  $b$ -quark jets we allow for one additional jet from hard gluon emission. The signal-to-background ratio is similar for both jet multiplicities. Moreover, the NLO QCD generator used for heavy-quark background generation does not include resummation of the so-called Sudakov logarithms which would be relevant if 2- and 3-jet events classes were considered separately.
2. The condition  $|\cos \theta_{jet}| < \mathcal{C}_\theta$  is imposed for all jets in the event where  $\theta_{jet}$  is the jet polar angle, *i.e.* the angle between the jet axis and the beam line. This cut should improve signal-to-background ratio as the signal is almost uniform in  $\cos \theta$ , while the background is peaked at  $|\cos \theta| = 1$ .
3. Since the Higgs bosons are expected to be produced almost at rest, the ratio of the total longitudinal momentum calculated from all jets in the event,  $P_z$ , to the total energy,  $E$ , should fulfill condition  $|P_z|/E < \mathcal{C}_{P_z}$ .

To determine the cut parameter values  $\mathcal{C}_\theta$  and  $\mathcal{C}_{P_z}$  the corresponding distributions of the signal and heavy quark background events were compared (other background contributions were not considered at this stage). After cut 1 the optimal value of parameter  $\mathcal{C}_\theta$

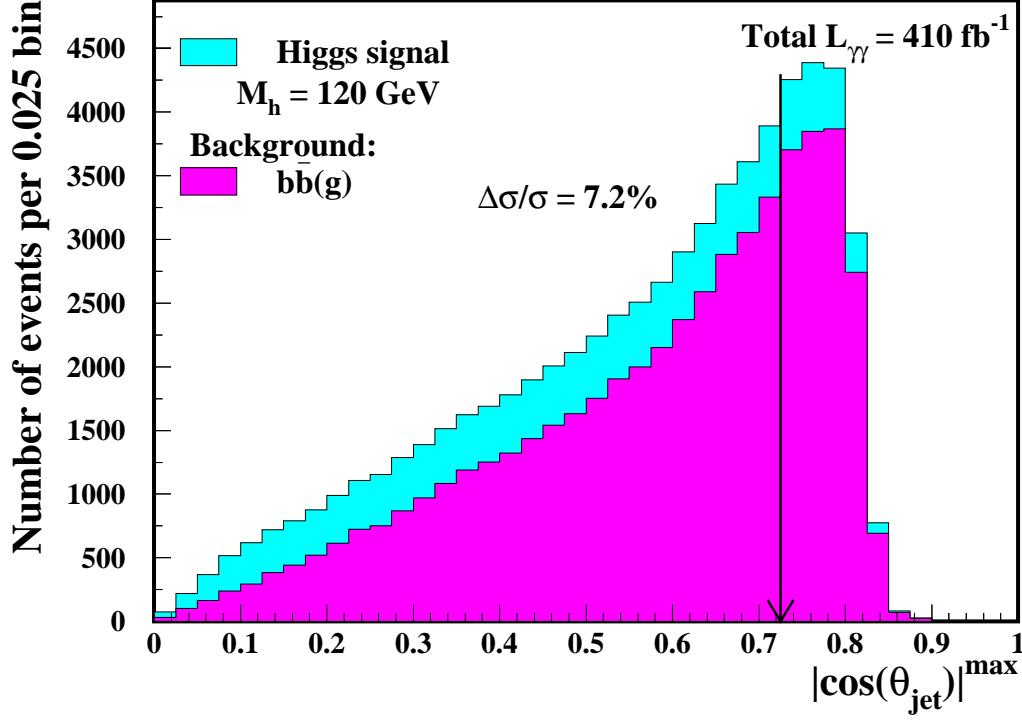


Figure 5.1: Distributions of  $|\cos\theta_{jet}|^{\max}$  (maximal value of  $|\cos\theta_{jet}|$  over all jets) for signal and background events. For background only  $\gamma\gamma \rightarrow b\bar{b}(g)$  events are shown. The signal measurement precision  $\Delta\sigma/\sigma$  of about 7% is obtained for  $|\cos\theta_{jet}|^{\max} < \mathcal{C}_\theta = 0.725$ .

(cut 2) is found as the one which minimizes the estimated statistical uncertainty of the measurement:

$$\frac{\Delta\sigma(\gamma\gamma \rightarrow h \rightarrow b\bar{b})}{\sigma(\gamma\gamma \rightarrow h \rightarrow b\bar{b})} = \frac{\sqrt{\mu_S + \mu_B}}{\mu_S},$$

where  $\mu_S$  and  $\mu_B$  are the numbers of expected signal and background events after the cut, respectively. With optimized cut 2 the same procedure is repeated for parameter  $\mathcal{C}_{P_z}$  (cut 3). The expected event distributions for  $|\cos\theta_{jet}|^{\max}$  (the maximum value of  $|\cos\theta_{jet}|$  over all jets in the event) and  $|P_z|/E$  are shown in Fig. 5.1 and 5.2, respectively. For simplicity only  $\gamma\gamma \rightarrow b\bar{b}(g)$  background contribution is shown. The  $\gamma\gamma \rightarrow c\bar{c}(g)$  contribution, which is around 16 times larger, has a very similar shape. Both background contributions are taken into account in cut optimization. For  $M_h = 120 \text{ GeV}$  the optimized cut values are  $\mathcal{C}_\theta = 0.725$  and  $\mathcal{C}_{P_z} = 0.1$ , as indicated in the figures (vertical arrows). The measurement precision is estimated to be around 7% and 5% after the  $|\cos\theta_{jet}|$  cut and after the  $|P_z|/E$  cut, respectively. Angular cuts used in the event selection procedure are compared in Fig. 5.3.



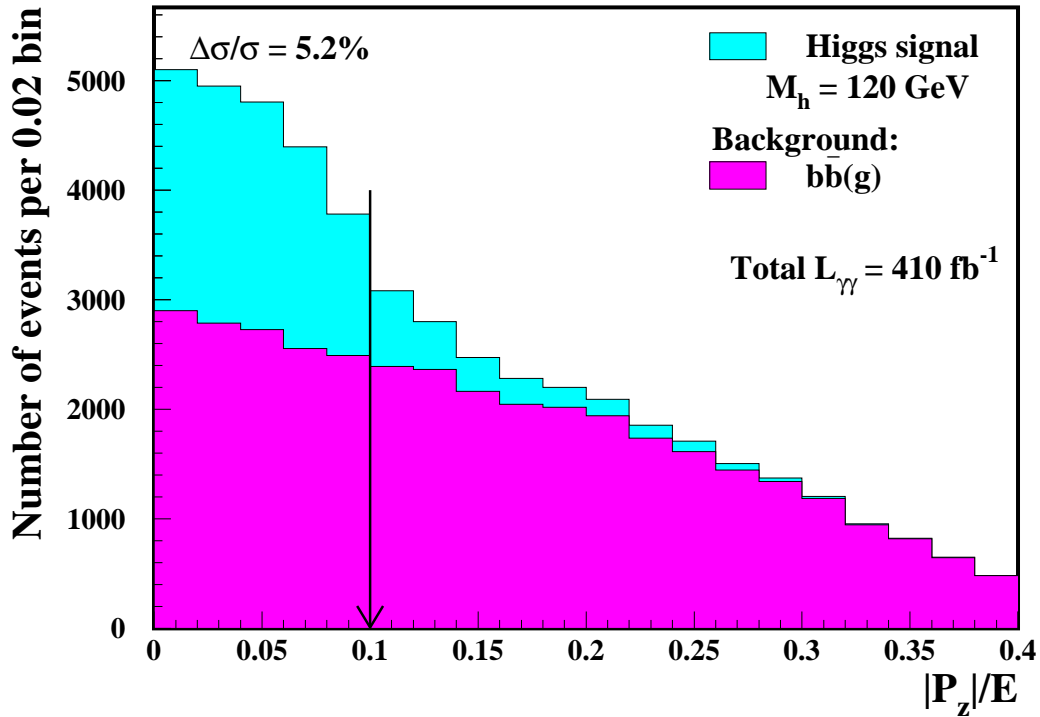


Figure 5.2: Distributions of  $|P_z|/E$  for signal and background events. For background only  $\gamma\gamma \rightarrow b\bar{b}(g)$  events are shown. The signal measurement precision  $\Delta\sigma/\sigma$  of about 5% is obtained for  $|P_z|/E < \mathcal{C}_{P_z} = 0.1$ .

### 5.3 $b$ -tagging algorithm

For  $b$ -tagging the ZVTOP-B-HADRON-TAGGER package prepared for the TESLA project was used [65, 66, 67]. The flavour tagging algorithm is based primarily on ZVTOP, the topological vertex finding procedure developed at SLD [68]. In addition to the ZVTOP results, a one-prong charm tag [65] and an impact parameter joint probability tag [69] outputs are used to train a neural net. Following parameters are given as an input to the neural-network algorithm (for all tracks or all vertices):

1. Impact parameters in  $r-\phi$  and  $r-z$ . Impact parameter in the  $r-\phi$  plane is defined as the minimal distance between the track trajectory and the beam axis; impact parameter in  $r-z$  plane is defined as the distance between the reconstructed primary vertex position and the point on the beam axis nearest to the track trajectory.
2. Significance of the track impact parameters – the ratio of the impact parameters to their estimated errors.
3. Vertex decay length – the distance between the primary vertex and the secondary

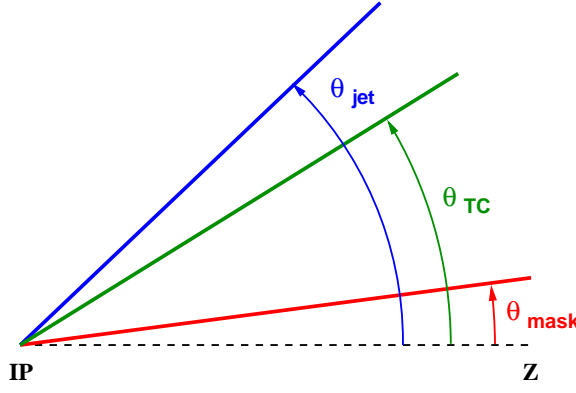


Figure 5.3: Comparison of the angular cuts used in the selection procedure of the Higgs-boson production events for  $M_h = 120$  GeV.

or tertiary vertex.

4. Vertex decay length significance – the ratio of the vertex decay length to its measurement error.
5.  $p_t$ -corrected mass of the secondary vertex – the invariant mass of particles coming from the vertex. As only charged particles (tracks) are considered, the correction for neutral particles is applied. The correction is based on the assumption that the total momentum of all particles coming from the secondary vertex must be parallel to the vector between the primary and secondary vertex positions.
6. Vertex momentum – the total momentum of all tracks belonging to the vertex.
7. Secondary vertex track multiplicity.
8. Secondary vertex probability – the probability that all tracks assigned by the ZV-TOP algorithm to the secondary vertex belong to this one vertex.

The neural-network algorithm was trained on the  $Z$  decays. For each jet the routine returns a “ $b$ -tag” value – the number between 0 and 1 corresponding to “ $b$ -jet” likelihood.

In order to optimize the signal cross-section measurement, the two-dimensional cut on  $b$ -tag values is used. In the signal events two jets with the highest transverse momentum are most likely to originate from  $b$  quarks. Therefore, all jets in the event are sorted according to the value of their transverse momentum. The distribution of  $b$ -tag values for 2 and 3-jet events is considered in the plane  $b\text{-tag}(\text{jet}_1) \otimes b\text{-tag}(\text{jet}_2)$  where indices 1 and 2 correspond to two jets with the highest transverse momenta. The two-dimensional distributions of  $b$ -tag values for the signal,  $\gamma\gamma \rightarrow h \rightarrow b\bar{b}$ , and for the background,  $\gamma\gamma \rightarrow b\bar{b}(g)$ , events are shown in Fig. 5.4. The corresponding distributions for other considered background contributions,  $\gamma\gamma \rightarrow c\bar{c}(g)$  and  $\gamma\gamma \rightarrow q\bar{q}$  ( $q = u, d, s$ ), are shown

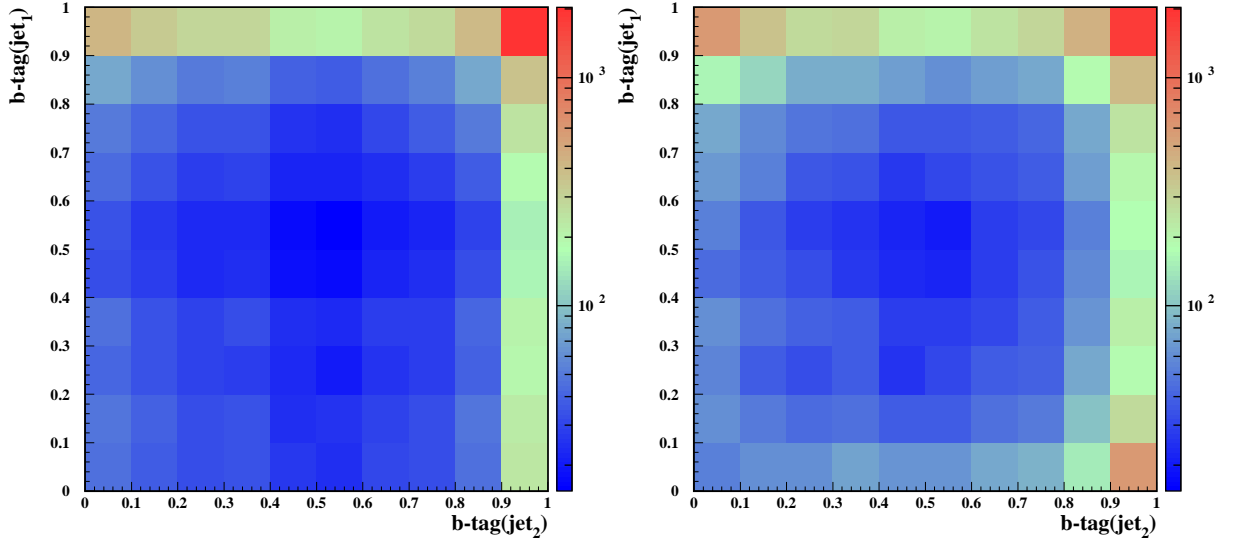


Figure 5.4: Distributions of  $\gamma\gamma \rightarrow h \rightarrow b\bar{b}$  (left) and  $\gamma\gamma \rightarrow b\bar{b}(g)$  (right) events in the plane  $b\text{-tag}(\text{jet}_1) \otimes b\text{-tag}(\text{jet}_2)$ .

in Fig. 5.5. Events considered in the  $b$ -tagging studies fulfill fore-mentioned, optimized selection cuts and an additional cut  $W_{rec} > 0.7 M_h$  which removes low-mass events not relevant for the final result (this cut is used only for tagging optimization). As expected, for processes  $\gamma\gamma \rightarrow h \rightarrow b\bar{b}$  and  $\gamma\gamma \rightarrow b\bar{b}(g)$  most events populate the regions with high  $b$ -tag values (Fig. 5.4), whereas most  $\gamma\gamma \rightarrow c\bar{c}(g)$  and  $\gamma\gamma \rightarrow q\bar{q}$  events have small  $b$ -tag values (Fig. 5.5). Nevertheless, significant fraction of  $\gamma\gamma \rightarrow c\bar{c}(g)$  events populates the region of high  $b$ -tag values, and the event distribution is more flat than the one for  $\gamma\gamma \rightarrow q\bar{q}$  events. The optimal *higgs*-tagging cut is found by considering the value of the signal to background ratio  $S/B$ , where  $S$  and  $B$  denote the expected numbers of events for the signal  $\gamma\gamma \rightarrow h \rightarrow b\bar{b}$  and for the sum of background contributions from processes  $\gamma\gamma \rightarrow Q\bar{Q}(g)$  ( $Q=c, b$ ) and  $\gamma\gamma \rightarrow q\bar{q}$  ( $q=u, d, s$ ), respectively. Obtained  $S/B$  distribution in the  $b\text{-tag}(\text{jet}_1) \otimes b\text{-tag}(\text{jet}_2)$  plane for Higgs-boson production with  $M_h = 120$  GeV is shown in Fig. 5.6. The selection criteria which results in the best precision of the  $\Gamma(h \rightarrow \gamma\gamma)\text{BR}(h \rightarrow b\bar{b})$  measurement corresponds to  $S/B > 0.19$  as indicated in the figure (stars).

The obtained efficiencies for tagging *higgs* events,  $b\bar{b}$  background events, and the probabilities for mistagging of the  $c\bar{c}$  and  $q\bar{q}$  ( $q=u, d, s$ ) events are  $\varepsilon_h = 58\%$ ,  $\varepsilon_{bb} = 50\%$ ,  $\varepsilon_{cc} = 2.2\%$  and  $\varepsilon_{uds} = 0.16\%$ , respectively. Similar efficiencies were obtained for other considered electron-beam energies. We call this procedure 'higgs-tagging' as the efficiency for tagging signal events,  $\varepsilon_h$ , is significantly higher than the efficiency for tagging  $b\bar{b}(g)$  background events,  $\varepsilon_{bb}$ . This is because large fraction of background events is reconstructed as 3-jet events (LO contribution is suppressed for  $J_z = 0$ ) in which the gluon

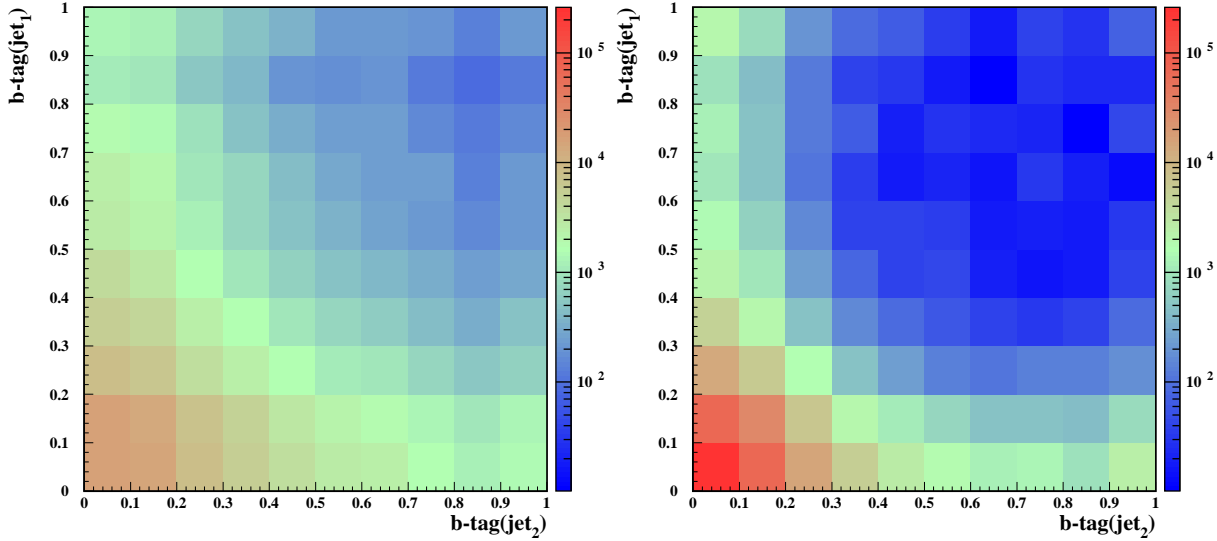


Figure 5.5: Distributions of  $\gamma\gamma \rightarrow c\bar{c}(g)$  (left) and  $\gamma\gamma \rightarrow q\bar{q}$ ,  $q=u, d, s$ , (right) events in the plane  $b\text{-tag}(\text{jet}_1) \otimes b\text{-tag}(\text{jet}_2)$ .

jet is often one of the two jets with highest transverse momenta. In the earlier analyses [23, 27] a fixed  $b\bar{b}$ -tagging efficiency,  $\varepsilon_h = \varepsilon_{bb} = 70\%$ , and a fixed  $c\bar{c}$ -mistagging efficiency,  $\varepsilon_{cc} = 3.5\%$ , were assumed. Although the efficiencies resulting from the optimized selection are much lower, signal to background ratio  $\varepsilon_h/\varepsilon_{cc}$  improves significantly.

Particles from  $\gamma\gamma \rightarrow \text{hadrons}$  overlaying events can significantly change properties of the jet to which they are assigned by the jet clustering algorithm. For example, the invariant mass of the jet increases on average by 3 GeV, if the angular cut is not applied (*i.e.* parameter  $\theta_{TC} = \theta_{mask}$ ; see Fig. C.11 in Appendix C). Although the average invariant mass of the jet after the cut corresponding to  $\cos\theta_{TC} = 0.85$  is similar to the jet mass without overlaying-events contribution, the jet structure can still be affected by the remaining particles from  $\gamma\gamma \rightarrow \text{hadrons}$  interactions, and by rejection of some particles coming from the signal process. These effects influence also the flavour tagging algorithm and cause a significant change in the results of the  $b\bar{b}$ -tagging optimization. To quantify the influence of overlaying events we repeated the optimization procedure, for production of the SM Higgs boson with  $M_h = 120$  GeV, without overlaying events and with  $\cos\theta_{TC} = 0.99$ . The resulting efficiencies, corresponding to optimal cut  $S/B > 0.16$ , are  $\varepsilon_h = 71\%$ ,  $\varepsilon_{bb} = 64\%$ ,  $\varepsilon_{cc} = 2.9\%$  and  $\varepsilon_{uds} = 0.11\%$ . The corresponding selection region in the  $b\text{-tag}(\text{jet}_1) \otimes b\text{-tag}(\text{jet}_2)$  plane is significantly wider than for the nominal analysis, but the  $c\bar{c}$  background suppression factor  $\varepsilon_{bb}/\varepsilon_{cc}$  is similar.

Although the selection region is smaller when overlaying events are taken into account, the efficiency for  $\gamma\gamma \rightarrow q\bar{q}$ ,  $q=u, d, s$ , is greater by about 50%. Jets coming from light-quark production can be significantly modified by  $\gamma\gamma \rightarrow \text{hadrons}$  events, and are more

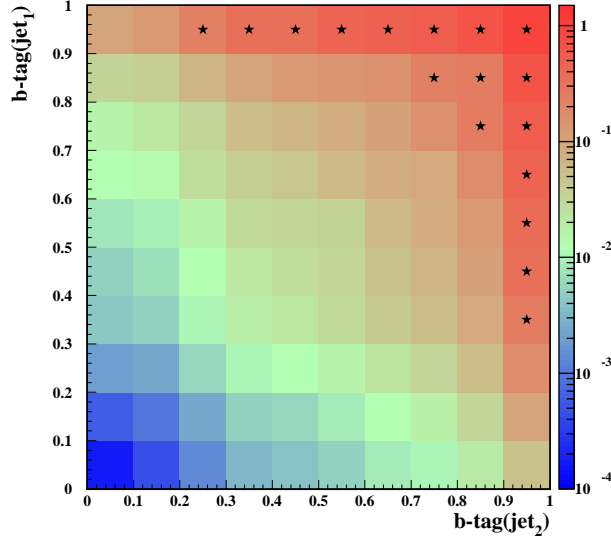


Figure 5.6: The expected ratio of signal ( $\gamma\gamma \rightarrow h \rightarrow b\bar{b}$ ) to background ( $\gamma\gamma \rightarrow Q\bar{Q}(g)$ ,  $Q=c, b$ , and  $\gamma\gamma \rightarrow q\bar{q}$ ,  $q=u, d, s$ ) event distributions in the plane  $\text{btag}(\text{jet}_1) \otimes \text{btag}(\text{jet}_2)$ . The region which results in the best precision measurement for the cross-section measurement is indicated by stars.

likely to be recognized as  $b$ -jets. One of important reasons is that the primary vertex of the overlaying event is usually shifted with respect to the primary vertex of the hard interaction. If particles from both interactions are combined in the reconstructed hadronic jet, the vertex finding algorithm is likely to reconstruct two vertices treating one of them as a primary vertex, and the second one as the vertex resulting from  $b$  decay. The effect of tagging deterioration is even stronger for higher beam energies as more overlaying events per bunch crossing are produced due to higher luminosity and cross section. The influence of overlaying events on the event reconstruction is clearly seen also in case of the heavy MSSM Higgs-bosons production as will be discussed in Chapter 6.

The influence of the optimized *higgs*-tagging criteria on the reconstructed invariant-mass,  $W_{rec}$ , distribution is shown in Fig. 5.7 for signal events  $\gamma\gamma \rightarrow h \rightarrow b\bar{b}$  after all described selection cuts. These results were obtained without overlaying events  $\gamma\gamma \rightarrow \text{hadrons}$ . The tail towards low masses is due to events with energetic neutrinos coming from semileptonic decays of  $D$  and  $B$  mesons (see [27] for more details). Contribution of these events can be suppressed by an additional cut  $P_T/E_T < 0.04$ , where  $P_T$  and  $E_T$  are the absolute values of the total transverse momentum of an event,  $\vec{P}_T$ , and the total transverse energy, respectively. We see that the efficiency of  $b$ -tagging is similar for events with and without energetic neutrinos as the algorithm does not significantly influence the shape of the distributions.

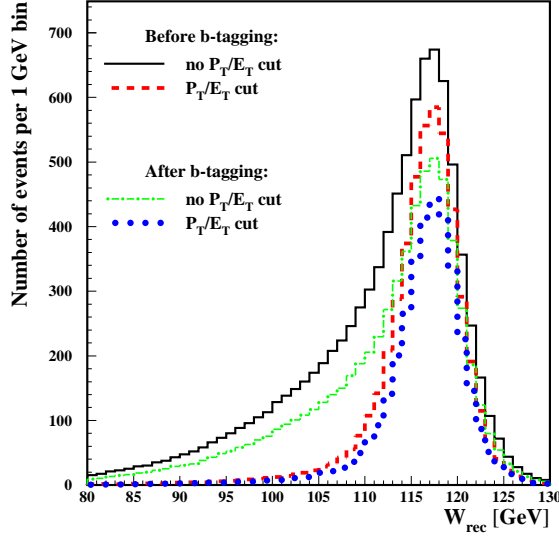


Figure 5.7: Distributions of the reconstructed invariant mass,  $W_{rec}$ , for selected  $\gamma\gamma \rightarrow h \rightarrow b\bar{b}$  events, for  $M_h = 120$  GeV. Distributions obtained before and after applying the  $b$ -tagging algorithm, without and with the additional  $P_T/E_T < 0.04$  cut are compared. Overlaying events are not included.

## 5.4 Results

The invariant-mass distributions for signal events passing all optimized selection cuts, before and after taking into account the overlaying events  $\gamma\gamma \rightarrow hadrons$  are compared in Fig. 5.8 (left). Mass resolution, derived from the Gaussian fit in the region from  $\mu - 1.3\sigma$  to  $\mu + 1.3\sigma$ , is about 4 and 6 GeV, respectively. The overlaying events and cuts suppressing their contribution significantly influence the mass reconstruction and result in an increase of distribution width by about 2 GeV, and in a shift of the mean value,  $\mu$ , by about 3 GeV. A drop in a selection efficiency, resulting in the reduced number of events expected after selection cuts (from about 6450 to 5530 events), is also observed. This is because tighter  $b$ -tagging cuts have to be imposed to reduce influence of overlaying events. More events are also rejected by the cut on the longitudinal momentum. Some drop in the selection efficiency is also due to the fact that the energy deposits from the  $\gamma\gamma \rightarrow hadrons$  processes, remaining after the  $\theta_{TC}$  cut, “shift” jets nearer to the beam axis and the event can be rejected by the jet-angle cut.

Distributions of the reconstructed invariant mass,  $W_{rec}$ , expected after applying all selection cuts and  $b$ -tagging algorithm, for the signal ( $\gamma\gamma \rightarrow h \rightarrow b\bar{b}$ ) and all considered background contributions are shown in Fig. 5.9. Beside the heavy quark production,  $\gamma\gamma \rightarrow b\bar{b}(g)$  and  $\gamma\gamma \rightarrow c\bar{c}(g)$ , all background contributions are small, of the order of 30%, 15% and 5% of the signal for  $\gamma\gamma \rightarrow hadrons$ ,  $\gamma\gamma \rightarrow q\bar{q}$  and  $\gamma\gamma \rightarrow \tau^+\tau^-$ , respectively.

We assume that the number of observed Higgs-boson production events will be ex-

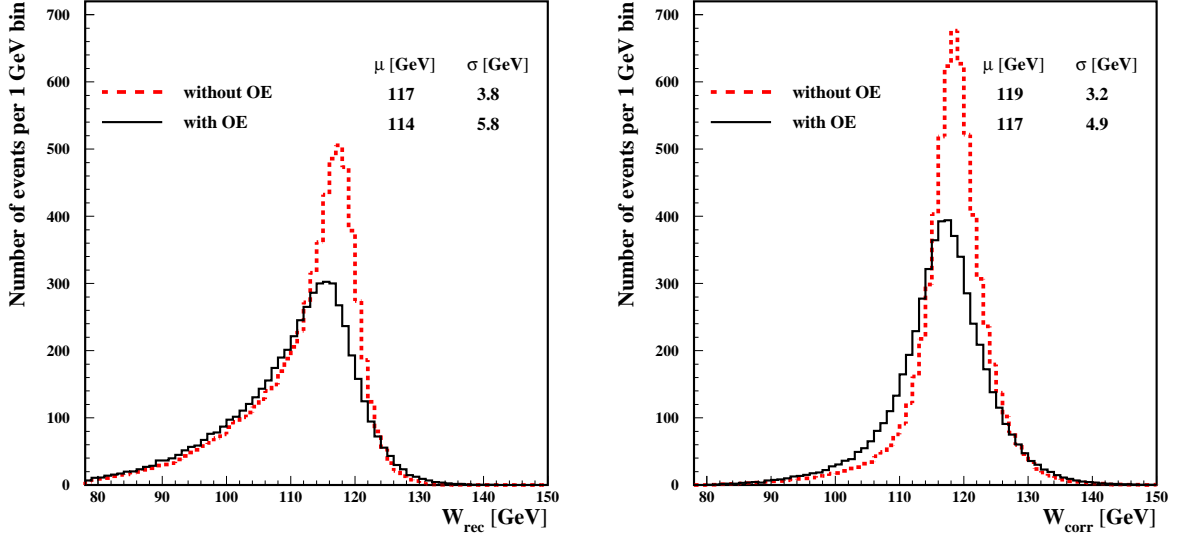


Figure 5.8: Reconstructed invariant-mass,  $W_{rec}$ , (left) and corrected invariant-mass,  $W_{corr}$ , (right) distributions for selected  $\gamma\gamma \rightarrow h \rightarrow b\bar{b}$  events, for  $M_h = 120$  GeV. Distributions obtained without and with overlaying events (OE) are compared. Results for the mean  $\mu$  and dispersion  $\sigma$  from the Gaussian fit in the region from  $\mu - 1.3\sigma$  to  $\mu + 1.3\sigma$ , are also shown.

tracted by counting the number of  $b\bar{b}$  events in the mass window around the Higgs-boson mass peak,  $N_{obs}$ , and subtracting the expected contribution of background events,  $\mu_B$ . The relative statistical error expected in the measurement of the Higgs-boson production cross section  $\sigma(\gamma\gamma \rightarrow h \rightarrow b\bar{b})$ , or of the partial width multiplied by the branching ratio  $\Gamma(h \rightarrow \gamma\gamma)\text{BR}(h \rightarrow b\bar{b})$ , can be estimated from the following formula:

$$\frac{\Delta\sigma(\gamma\gamma \rightarrow h \rightarrow b\bar{b})}{\sigma(\gamma\gamma \rightarrow h \rightarrow b\bar{b})} = \frac{\Delta[\Gamma(h \rightarrow \gamma\gamma)\text{BR}(h \rightarrow b\bar{b})]}{\Gamma(h \rightarrow \gamma\gamma)\text{BR}(h \rightarrow b\bar{b})} = \frac{\sqrt{\mu_S + \mu_B}}{\mu_S} \quad (5.1)$$

where  $\mu_s$  is expected number of signal events, and the expected number of observed events is  $\langle N_{obs} \rangle = \mu_S + \mu_B$ . The accuracy obtained from the reconstructed invariant-mass distribution for  $M_h = 120$  GeV is equal to 2.3%. The mass window used to calculate the signal measurement precision is again optimized to obtain the lowest relative error. For  $M_h = 120$  GeV the selected mass window is 100 to 127.5 GeV as indicated in Fig. 5.9 (vertical arrows). The obtained result is consistent with results of our previous analyses [27, 30] which however did not take into account many aspects of the measurement considered here. In the current analysis additional background contributions deteriorate the precision of the cross section measurement. However, the effect is partially compensated by the performed optimization of selection procedure.

Significant part of the energy in the signal events can be lost due to escaping neutrinos. As shown in Fig. 5.7, this effect worsens the mass resolution and, as a result, the cross

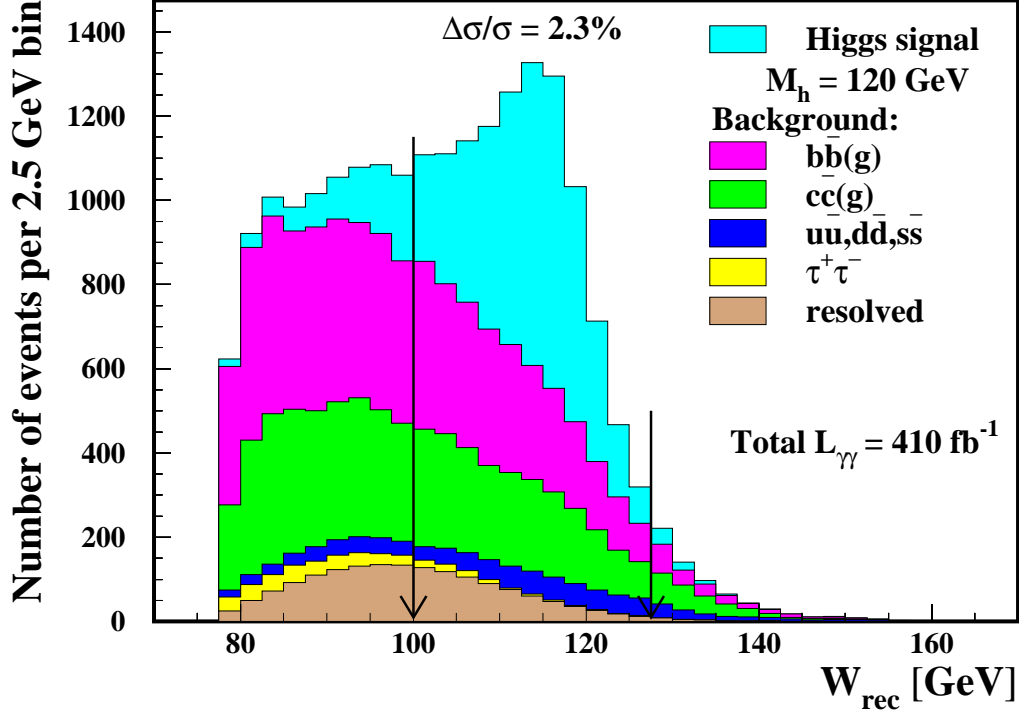


Figure 5.9: Distributions of the reconstructed invariant mass,  $W_{rec}$ , for selected  $b\bar{b}$  events. Contributions of the signal, for  $M_h = 120$  GeV, and of the background processes, *i.e.*  $\gamma\gamma \rightarrow q\bar{q}$  for  $q=u, d, s$ ,  $\gamma\gamma \rightarrow \tau^+\tau^-$ , and  $\gamma\gamma \rightarrow hadrons$  (as a separate contribution with *hadron-like* $\times$ *hadron-like* interactions only, indicated as 'resolved'), are shown separately. Arrows indicate the mass window, 100 to 127.5 GeV, optimized for the measurement of the  $\Gamma(h \rightarrow \gamma\gamma)\text{BR}(h \rightarrow b\bar{b})$ , which leads to the statistical precision of 2.3%.

section measurement precision. We have looked for a correction method which would improve the mass resolution without reducing the event statistics. Unfortunately, due to a large spread of the photon beam energy, no unambiguous constraint can be imposed on the reconstructed longitudinal momentum. We have considered four methods of correcting the measured invariant mass:

1. The value of the measured transverse momentum is added to the total energy and the transverse momentum is balanced. This is equivalent to the assumption that the missing transverse momentum is due to a single neutrino emitted perpendicularly to the beam line. The procedure is illustrated in Fig. 5.10 where the 2-jet  $\gamma\gamma \rightarrow h \rightarrow b\bar{b}$  event is shown with energy and momentum carried out by two neutrinos. As the total longitudinal momentum,  $P_L$ , is not constrained, the missing longitudinal momentum,  $P_L^{miss}$ , cannot be estimated. However, the total transverse momentum should be balanced. Thus, the missing transverse momentum,  $P_T^{miss}$ ,



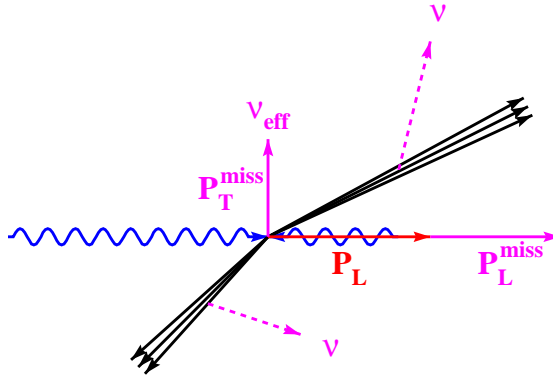


Figure 5.10: The 2-jet  $\gamma\gamma \rightarrow h \rightarrow b\bar{b}$  event in which part of energy is carried out by neutrinos. As the total longitudinal momentum,  $P_L$ , is unknown, the missing longitudinal momentum,  $P_L^{miss}$ , cannot be estimated. However, the total transverse momentum should be balanced and the missing transverse momentum,  $P_T^{miss}$ , can be attributed to the 'effective' neutrino,  $\nu_{eff}$ .

can be attributed to the 'effective' neutrino. This correction was introduced in our earlier analysis [27].

2. The transverse momentum,  $p_T$ , of the jet with lowest  $p_T$  is increased by a value of the total missing transverse momentum and the longitudinal jet momentum is rescaled to preserve its original direction. This method is applied for 2-jet events and assumes that the missing  $P_T$  is due to the single neutrino emitted along the jet with lower  $p_T$ . In general the total transverse momentum is still unbalanced after this correction.
3. The transverse momentum of 2-jet event is balanced under assumption that the missing  $P_T$  is due to the neutrino emitted under the polar angle equal to the polar angle of the jet with lowest  $p_T$ .
4. The transverse momentum of 3-jet events is balanced by rescaling momenta of two jets. All combinations are checked and the most "reasonable" one is chosen, *i.e.* the one satisfying the requirement that each of two rescaling factors is greater than 1 and less than 1.3.

Approaches combining these methods were also taken into account. Moreover, we also considered the algorithms where the correction were limited to events with transverse momentum greater than some threshold value, which was varied to obtain the best mass resolution. Surprisingly, the first (and simplest) procedure proved to be the best one when applied to all events. Other correction methods introduce systematic bias in the corrected invariant mass distributions and sometimes result even in the deterioration of the final

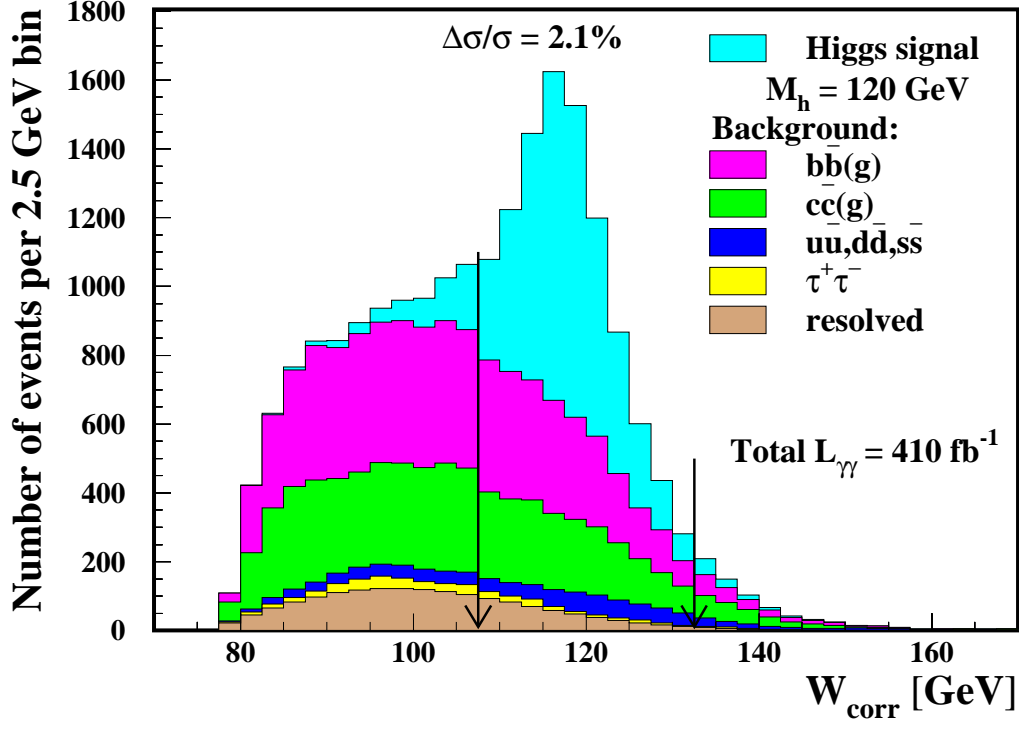


Figure 5.11: As in Fig. 5.9, for the corrected invariant mass,  $W_{corr}$ , distributions. Arrows indicate the mass window, 107.5 to 132.5 GeV, optimized for the measurement of the  $\Gamma(h \rightarrow \gamma\gamma)\text{BR}(h \rightarrow b\bar{b})$ , which leads to the statistical precision of 2.1%.

cross-section measurement precision. Thus, the corrected reconstructed invariant mass used for the final analysis was defined as [27]:

$$W_{corr} \equiv \sqrt{W_{rec}^2 + 2P_T(E + P_T)}. \quad (5.2)$$

In Fig. 5.8 (right) the distributions of  $W_{corr}$  for the selected signal events, without and with overlaying events, are presented. The tail of events with invariant masses below  $\sim 110$  GeV is much smaller than for the  $W_{rec}$  distributions (compare with the left figure). The mass resolutions, derived from the Gaussian fits to the  $W_{corr}$  distributions in the region from  $\mu - 1.3\sigma$  to  $\mu + 1.3\sigma$ , are equal to 3.2 and 4.9 GeV, without and with overlaying events, respectively. Also the mean values obtained from the fit are closer to  $M_h$  than the values when  $W_{rec}$  was used.

The final  $W_{corr}$  distributions for the signal and background events (with overlaying events included) are shown in Fig. 5.11. For  $M_h = 120$  GeV the most precise measurement of the Higgs-boson production cross section is obtained for the mass window between 108 and 133 GeV, as indicated by arrows. In the selected  $W_{corr}$  region one expects, after

one year of the Photon Collider running at nominal luminosity, about 4900 reconstructed signal events and 5400 background events (*i.e.*  $\mu_S/\mu_B \approx 0.9$ ). This corresponds to the statistical precision of:

$$\frac{\Delta [\Gamma(h \rightarrow \gamma\gamma)\text{BR}(h \rightarrow b\bar{b})]}{\Gamma(h \rightarrow \gamma\gamma)\text{BR}(h \rightarrow b\bar{b})} = 2.1\%.$$

The statistical precision calculated with the formula 5.1 should be considered a conservative estimate as it does not take into account our knowledge of the shape of the signal and background contributions. To exploit this additional information we can determine the measured number of signal events by the maximum likelihood method. In this procedure the background contribution is assumed to be fixed and the likelihood function depends only on the total number of signal events. The Poissonian distribution of events in each bin is assumed. For the production of the Higgs boson with  $M_h = 120$  GeV we find that precision of the signal cross-section determination from the measured  $W_{corr}$  distribution (without mass window cut) is 2.0%.

The maximum likelihood method can also be used to estimate the systematic uncertainty of the cross section measurement. With this approach the systematic uncertainties of the estimated total background contribution and of the luminosity determination are included. We assume that both uncertainties are described by Gaussian distributions. The systematic uncertainty of the total background contribution is estimated to be about 2%. This is based on the assumption that the background can be constrained from the dedicated run of the Photon Collider at lower value of  $\sqrt{s_{ee}}$ . If the center-of-mass-system energy is reduced by about 10 GeV, then only background events are measured (the Higgs boson will not be produced due to very low luminosity at  $W_{\gamma\gamma} = M_h$ ) while the detector performance remains almost unchanged. During half a year of the Photon Collider running about 3000 events can be selected in the invariant-mass range corresponding to the optimal mass window for the Higgs-boson production measurement. The statistical uncertainty of 2% on the background contribution can be obtained which could be reduced by in a longer run if required. This uncertainty will result in the corresponding systematic error in the (independent) Higgs-boson production measurement. The  $J_z = 0$  luminosity contribution will be measured with precision of around 1% [72] and this is assumed to be the expected uncertainty for the total luminosity (the  $|J_z| = 2$  luminosity contribution will be known with much better precision but it is small in the Higgs-resonance region). Using maximal likelihood procedure with assumed systematic uncertainties we obtain precision of 2.7% for  $\sigma(\gamma\gamma \rightarrow h \rightarrow b\bar{b})$  measurement at  $M_h = 120$  GeV. Therefore we can conclude that the systematic error of the measurement is of the order of 1.8%.

The final result for  $\Gamma(h \rightarrow \gamma\gamma)\text{BR}(h \rightarrow b\bar{b})$  should be extracted from the measured event rate by applying correction for the selection efficiency. In our analysis the total

efficiency for signal events is only about 30%. The significant reduction of the signal events is due to the  $b$ -tagging cut. Therefore a very precise determination of flavour tagging efficiency will be crucial. To minimize influence of the uncertainties resulting from the Monte Carlo description of the detector performance we propose to use hadronic decays of  $Z$  bosons for  $b$ -tagging studies. After one year of the Photon Collider running at  $\sqrt{s_{ee}} = 419$  GeV, the sample of about 26000  $\gamma\gamma \rightarrow ZZ$  events will be collected [49]. Taking into account branching ratios and the selection efficiency of about 80%, the expected number of  $Z \rightarrow b\bar{b}$  decays will be about 5000. This sample will allow us to determine the flavour tagging efficiency for  $b$ -jets with statistical precision of about 1.4%.

There is also an alternative solution: taking  $e^+e^-$  data at  $\sqrt{s_{ee}} = M_Z$  for two to three months (the so-called GigaZ project), using the same detector and selection procedure as described above. Having about  $10^9$  events of  $Z$ -boson production we could determine flavour-tagging efficiencies with exceptional statistical precision of about  $10^{-4}$ . Also other systematic uncertainties could be significantly reduced with such a large sample of  $Z$  decays. Therefore we would like to stress that the possibility of  $e^+e^-$  operation in the collision point designed for the  $\gamma\gamma$  mode should be guaranteed to make full use of the physics potential of the Photon Collider.

For all methods, results for systematic uncertainties will require some extrapolation. However, we estimate that after a year of additional running, the total systematic uncertainty of the  $\Gamma(h \rightarrow \gamma\gamma)\text{BR}(h \rightarrow b\bar{b})$  measurement can be reduced to about 2%.

The background contribution due to  $\gamma\gamma \rightarrow W^+W^-$  production is included in the analysis for  $M_h = 150$  and 160 GeV. Hadronic decays of  $W^+W^-$  pairs result in 4-jet final state. However, in significant fraction of events only 3 or 2 jets are reconstructed. As cross section for  $W^+W^-$  production is very high, additional cuts, dedicated to suppress  $\gamma\gamma \rightarrow W^+W^-$  background are introduced:

1. Events are rejected if  $M_{jet}^{\max} > \mathcal{C}_{M_{jet}}$ , where  $M_{jet}^{\max}$  is the highest invariant mass of the jet in the event.
2. Total energy measured below  $\theta_{TC}$ ,  $E_{TC}$ , should be less than  $\mathcal{C}_{E_{TC}}$ .
3. Each jet in the event should contain at least  $\mathcal{C}_{N_T}$  tracks, *i.e.*  $N_{trk}^{\min} \geq \mathcal{C}_{N_T}$  where  $N_{trk}^{\min}$  is the minimal number of tracks in jet for a given event.

The first cut removes the events in which two jets from decay of one  $W$  boson have been joined into one jet by the jet-clustering algorithm. The second condition rejects events with substantial energy in the forward region, below  $\theta_{TC}$ , where one or two jets from  $W^+W^-$  decay could deposit their energy. The last cut, with the parameter value  $\mathcal{C}_{N_T} = 4$ , suppresses leptonic decays of  $W$ . For  $M_h = 160$  GeV the optimal values for the two other thresholds are  $\mathcal{C}_{M_{jet}} = 70$  GeV and  $\mathcal{C}_{E_{TC}} = 90$  GeV.

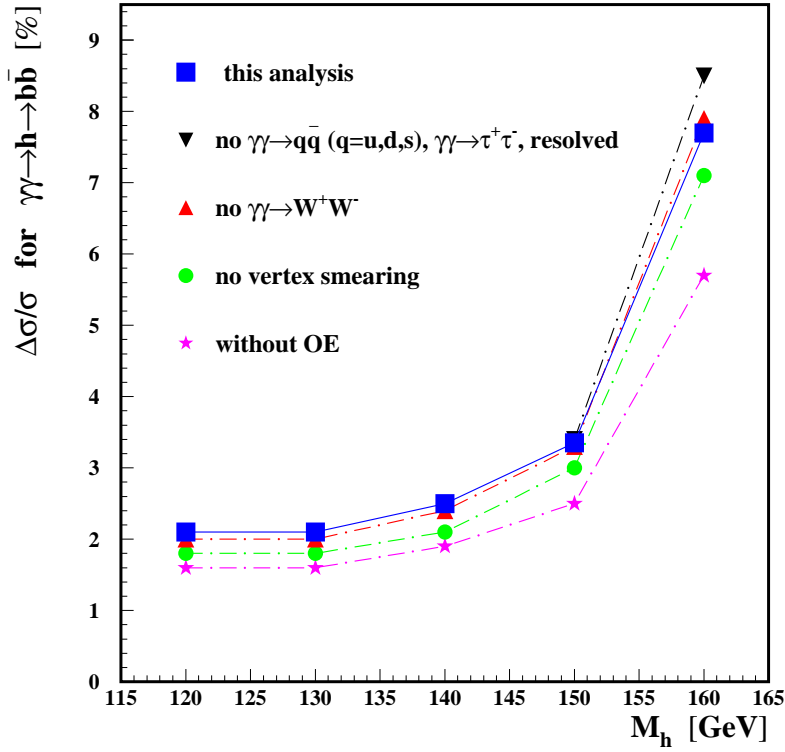


Figure 5.12: Statistical precision of  $\Gamma(h \rightarrow \gamma\gamma)\text{BR}(h \rightarrow b\bar{b})$  measurement for the SM Higgs boson with mass 120–160 GeV. Final results of this analysis are compared with our earlier results, which did not take into account some of the background contributions, distribution of the interaction point or overlaying events. The lines are drawn to guide the eye.

We have performed a full simulation of signal and background events also for  $M_h = 130, 140, 150$  and 160 GeV choosing optimal  $e^-e^-$  beam energy for each Higgs-boson mass. Statistical precision of  $\Gamma(h \rightarrow \gamma\gamma)\text{BR}(h \rightarrow b\bar{b})$  measurement was estimated in each case. It is equal to 2.1%, 2.5%, 3.4% and 7.7%, respectively. These results, together with the result for  $M_h = 120$  GeV described above, are presented in Fig. 5.12. For comparison, our earlier results obtained without overlaying events, without various background contributions or without distribution of interaction point are also shown. For  $M_h = 160$  GeV, after the full optimization of the selection cuts, better precision is obtained than in earlier analyses, which did not take into account some background contributions.



# Chapter 6

## Production of heavy neutral Higgs bosons in the MSSM

The analysis of the MSSM Higgs-bosons production closely follows the SM study described in Chapter 5. Therefore only these parts of the analysis which differ from the SM case are discussed in detail below.

The analysis was developed for set *I* of the MSSM parameters, as defined in Section 4.1, with  $\tan\beta = 7$ . To simplify the description the procedure is first presented for  $M_A = 300$  GeV, and later extended to  $M_A = 200, 250$  and  $350$  GeV. In each case the beam energy was chosen in such a way, as to provide the highest luminosity for  $\gamma\gamma$  collisions with  $J_z = 0$  at  $W_{\gamma\gamma} = M_A$ . For detailed information about beam energies and  $\gamma\gamma$ -luminosities, for the considered Higgs-boson masses, see Tab. 3.3.1.

For  $\sqrt{s_{ee}} \approx 400$  GeV about two  $\gamma\gamma \rightarrow \text{hadrons}$  events are expected on average in each bunch crossing. To suppress the influence of these events optimization of the  $\theta_{TC}$  cut was repeated, as described in Appendix C and the value  $\theta_{TC} = 0.85$ , used in the SM analysis, turned out to be optimal also for the MSSM case.

Selection criteria were optimized for the measurement of the *higgs* production cross section. The event distributions for  $|\cos\theta^{jet}|^{\max}$  and  $|P_z|/E$  are shown in Fig. 6.1 and 6.2, respectively. For  $M_A = 300$  GeV the optimized cut values are  $\mathcal{C}_\theta = 0.65$  and  $\mathcal{C}_{P_z} = 0.06$  (indicated by arrows). The measurement precision is estimated to be around 32% and 22%, after the  $|\cos\theta^{jet}|$  cut and after the  $|P_z|/E$  cut, respectively.

As in the SM case,  $b\bar{b}$  events were selected by considering *b*-tag values for two jets with highest transverse momentum. For  $M_A = 300$  GeV the selection region in the  $\text{btag}(\text{jet}_1) \otimes \text{btag}(\text{jet}_2)$  plane which gives the best precision of the  $\sigma(\gamma\gamma \rightarrow A, H \rightarrow b\bar{b})$  measurement is shown in Fig. 6.3. Optimal  $b\bar{b}$  selection, when overlaying events are taken into account, corresponds to the efficiencies  $\varepsilon_h = 53\%$ ,  $\varepsilon_{bb} = 47\%$ ,  $\varepsilon_{cc} = 2.9\%$ , and  $\varepsilon_{uds} = 0.5\%$ , *i.e.*  $c\bar{c}$  background suppression by a factor of  $\varepsilon_{bb}/\varepsilon_{cc} \approx 16$ . This should be compared to results obtained when overlaying events are not included – then the optimized

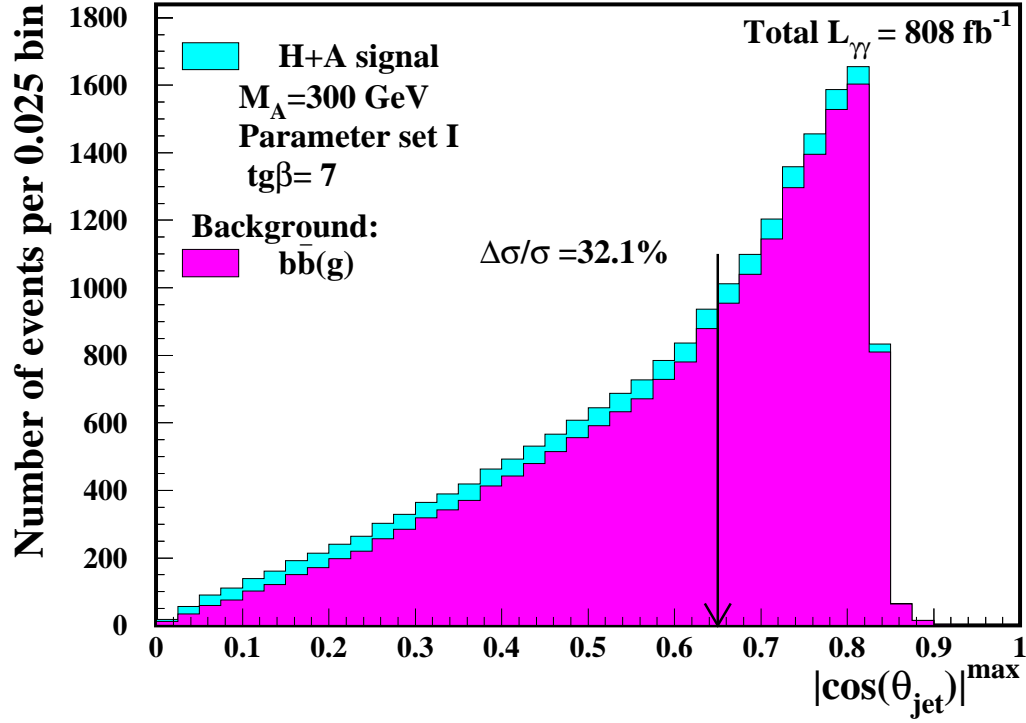


Figure 6.1: Distributions of  $|\cos\theta_{jet}|^{\text{max}}$  for signal and background events. Only  $\gamma\gamma \rightarrow b\bar{b}(g)$  events are shown for the background. The signal measurement precision for events fulfilling the cut  $|\cos\theta_{jet}|^{\text{max}} < \mathcal{C}_\theta = 0.65$ ,  $\Delta\sigma/\sigma$ , is around 32%.



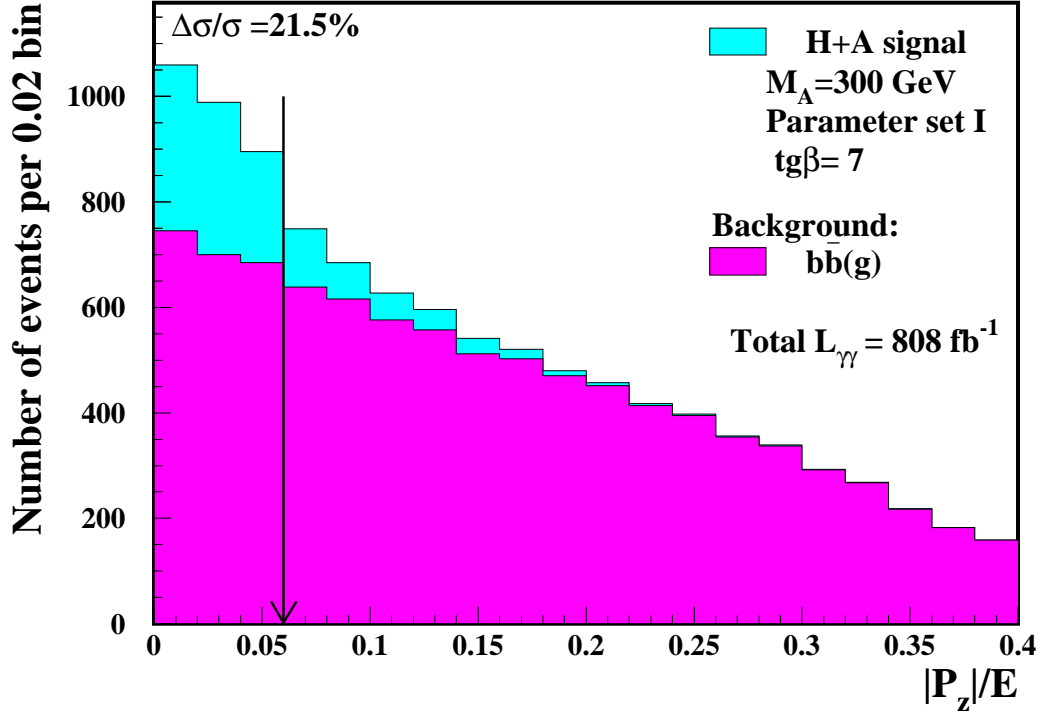


Figure 6.2: Distributions of  $|P_z|/E$  for signal and background events. Only  $\gamma\gamma \rightarrow b\bar{b}(g)$  events are shown for the background. The signal measurement precision for events fulfilling the cut  $|P_z|/E < \mathcal{C}_{P_z} = 0.06$ ,  $\Delta\sigma/\sigma$ , is around 22%.

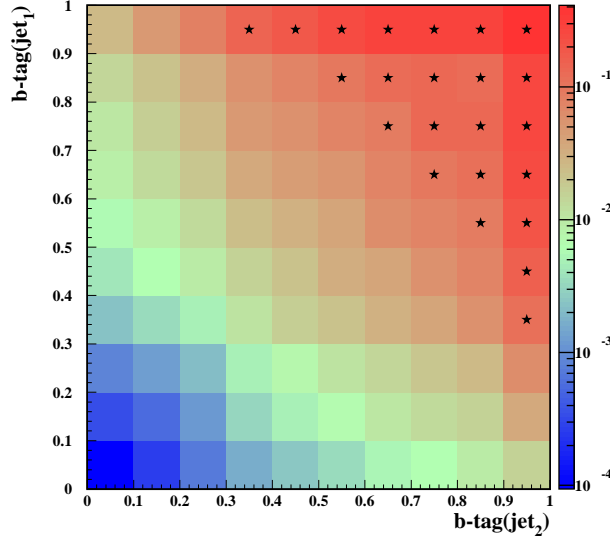


Figure 6.3: Ratio of  $\gamma\gamma \rightarrow A, H \rightarrow b\bar{b}$  events to  $\gamma\gamma \rightarrow b\bar{b}(g)$ ,  $\gamma\gamma \rightarrow c\bar{c}(g)$  and  $\gamma\gamma \rightarrow q\bar{q}$ ,  $q=u, d, s$ , events distributions in the plane  $\text{btag}(\text{jet}_1) \otimes \text{btag}(\text{jet}_2)$ . The region is indicated by stars which gives the best precision measurement for  $\sigma(\gamma\gamma \rightarrow A, H \rightarrow b\bar{b})$ .

selection corresponds to the efficiencies  $\varepsilon_h = 57\%$ ,  $\varepsilon_{bb} = 52\%$ ,  $\varepsilon_{cc} = 1.8\%$ , and  $\varepsilon_{uds} = 0.1\%$ , *i.e.*  $\varepsilon_{bb}/\varepsilon_{cc} \approx 29$ . This comparison shows that for heavy Higgs bosons overlaying events increase relative probability of  $c\bar{c}$ -mistagging by a factor of about 2. Even larger effect is observed for light quark-pair production as we observe increase of  $\varepsilon_{uds}$  by a factor of 5 despite the tighter selection cut.

In Fig. 6.4 we compare the  $(W_{rec} - W_{\gamma\gamma})$  distributions, for signal events  $\gamma\gamma \rightarrow A \rightarrow b\bar{b}$ , before and after taking into account the overlaying events. Mass resolution, derived from the Gaussian fit in the region from  $\mu - 1.3\sigma$  to  $\mu + 1.3\sigma$ , is about 8 and 12 GeV, respectively. The overlaying events and cut  $\theta_{TC}$  suppressing their contribution significantly influence the reconstructed mass distribution and result in a deterioration of the mass resolution. However, no significant drop in the selection efficiency is observed (the number of selected events is about 220 in both cases), in contrary to the SM case. Corresponding distributions of  $(W_{corr} - W_{\gamma\gamma})$  are compared in Fig. 6.4. The mass resolution for  $\gamma\gamma \rightarrow A \rightarrow b\bar{b}$  events, for  $M_A = 300$  GeV, is about 7 GeV without and about 10 GeV with overlaying events. As the mass resolution is much bigger than the mass difference between heavy neutral Higgs bosons  $H$  and  $A$ ,  $M_H - M_A \approx 1.5$  GeV, the separation of these two contributions will be impossible for the considered parameter set. Even for  $\tan\beta = 3$  the mass difference ( $M_H - M_A \approx 6.8$  GeV) will be too small to resolve  $A$  and  $H$  contributions, see Fig. 6.5.

The influence of overlaying events on the Higgs-boson production measurement is also illustrated in Fig. 6.6 and 6.7 where the  $W_{rec}$  and  $W_{corr}$  distributions, respectively, are shown for signal and background events (for this comparison only quark-pair production

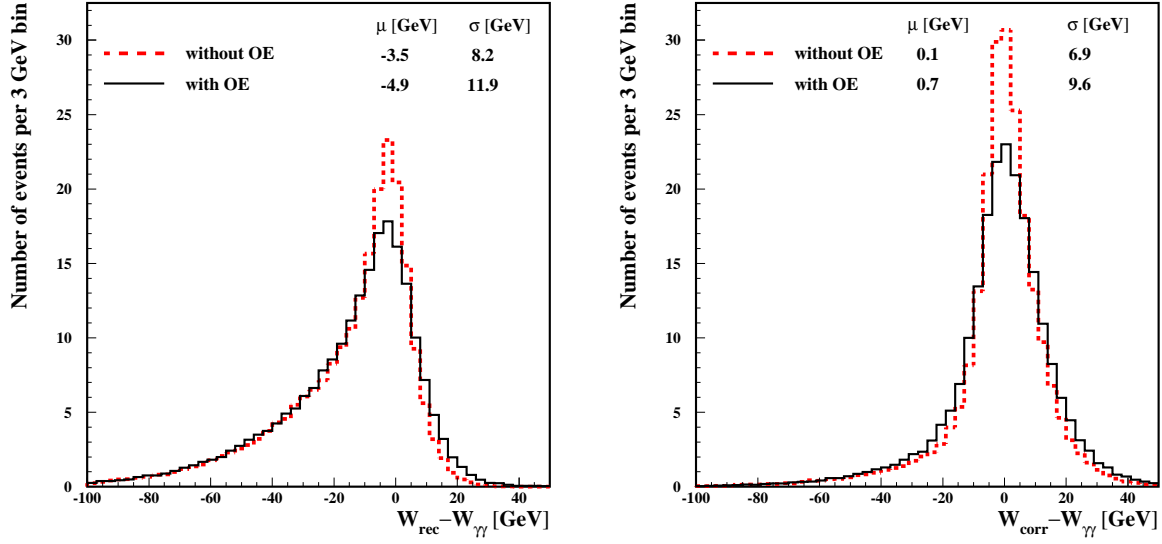


Figure 6.4: Mass resolution of the Higgs-boson  $A$ ,  $W_{rec} - W_{\gamma\gamma}$  (left), and  $W_{corr} - W_{\gamma\gamma}$  (right), for the selected events for  $M_A = 300$  GeV, obtained without and with overlaying events (OE). Mean and dispersion values,  $\mu$  and  $\sigma$ , from the Gaussian fit between  $\mu - 1.3\sigma$  and  $\mu + 1.3\sigma$  are indicated.

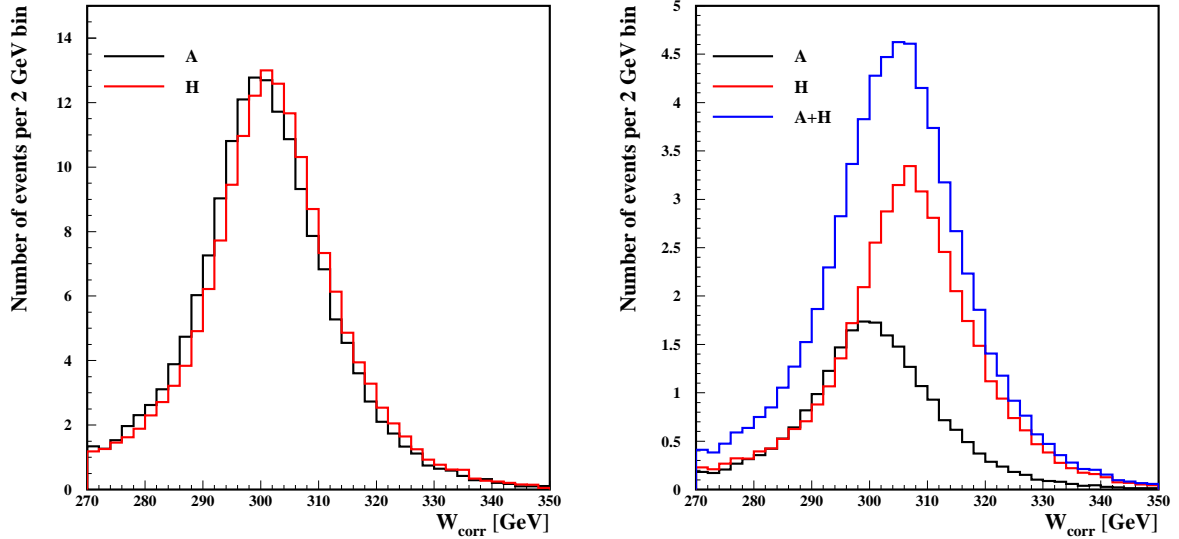


Figure 6.5: Corrected invariant mass,  $W_{corr}$ , distributions for the selected  $\gamma\gamma \rightarrow H \rightarrow b\bar{b}$  and  $\gamma\gamma \rightarrow A \rightarrow b\bar{b}$  events ( $M_A = 300$  GeV), with overlaying events, for  $\tan\beta = 7$  (left) and  $\tan\beta = 3$  (right), respectively. For  $\tan\beta = 3$  also the sum of both contributions is shown.

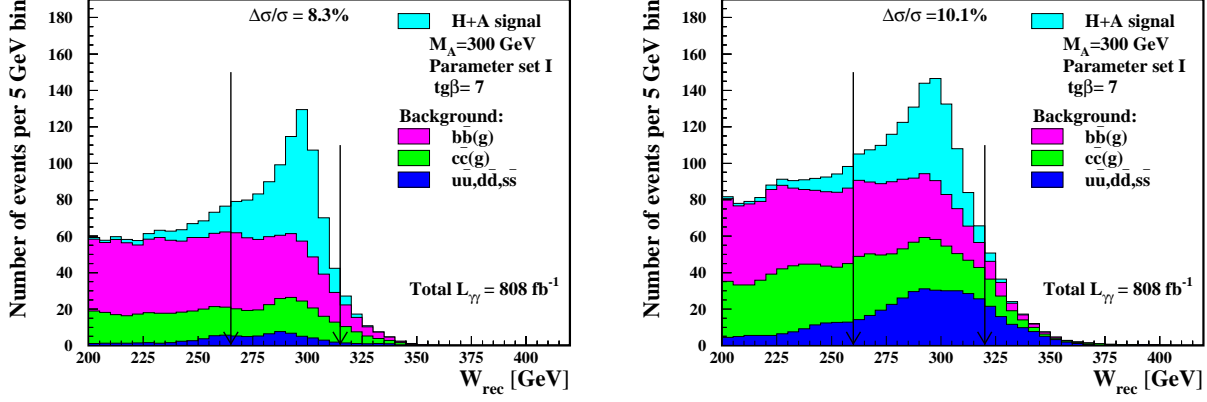


Figure 6.6: Distribution of the reconstructed invariant mass,  $W_{rec}$ , for  $b\bar{b}$  events ( $M_A = 300$  GeV) selected before (left plot) and after (right plot) taking into account overlaying events. Contributions of the  $H$  and  $A$  signal and of the quark-pair backgrounds are shown separately. Arrows indicate the mass windows optimized for the measurement of  $\sigma(\gamma\gamma \rightarrow A, H \rightarrow b\bar{b})$ .

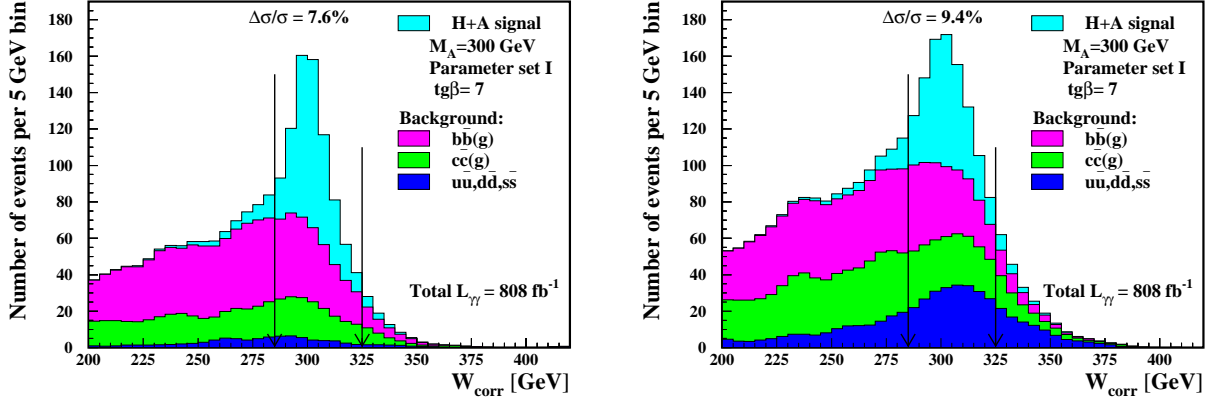


Figure 6.7: As in Figs. 6.6, for the corrected invariant-mass,  $W_{corr}$ , distributions. The statistical precision is 7.6% without overlaying events (left plot) and 9.4% with overlaying events (right plot).

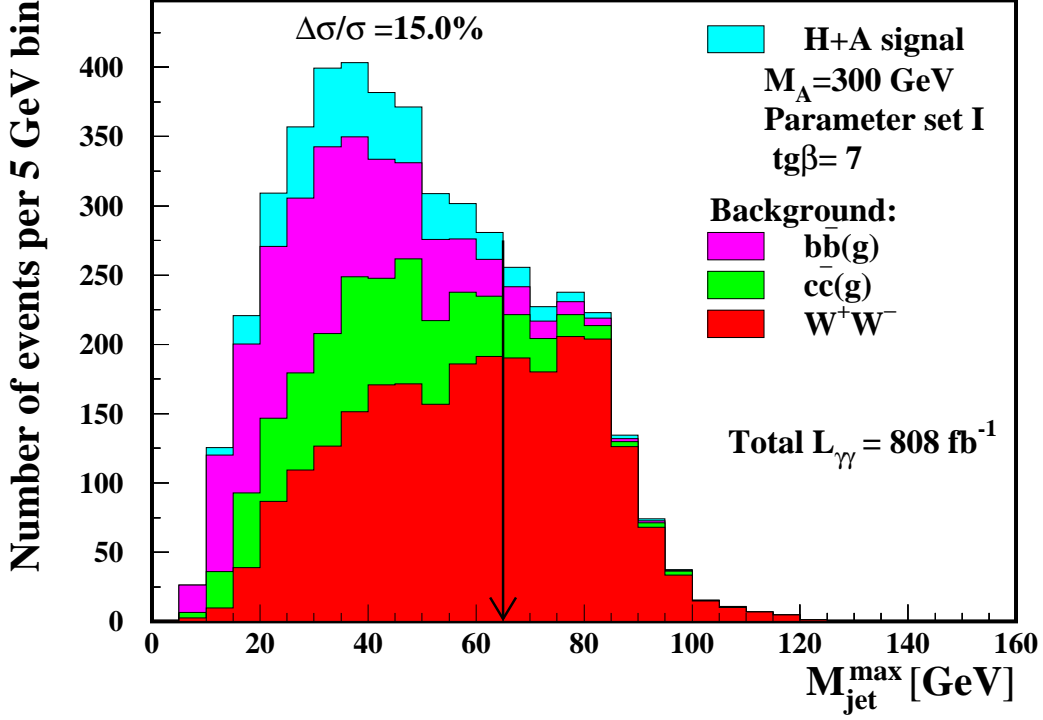


Figure 6.8: Distributions of the maximal jet mass,  $M_{jet}^{\max}$ , expected for signal and background contributions (overlying events included).

is taken as the background). In both cases distributions obtained without and with overlying events are compared. We conclude that overlying events significantly deteriorate the cross section measurement by increasing the selection efficiency of background contributions. As in the SM case, better estimates for measurement error  $\Delta\sigma(\gamma\gamma \rightarrow A, H \rightarrow b\bar{b})/\sigma(\gamma\gamma \rightarrow A, H \rightarrow b\bar{b})$  are obtained when using the variable  $W_{corr}$ .

For all considered heavy Higgs-boson masses in the MSSM, additional cuts to suppress  $\gamma\gamma \rightarrow W^+W^-$  background were also applied, as described for the SM Higgs boson with  $M_h = 160$  GeV. For  $M_A = 300$  GeV the optimal threshold values are  $\mathcal{C}_{M_{jet}} = 65$  GeV and  $\mathcal{C}_{ETC} = 80$  GeV. The corresponding distributions of events are shown in Fig. 6.8 and 6.9. The resulting estimate of the cross-section measurement precision is about 14%. After the additional cut on the number of tracks in each jet ( $\mathcal{C}_{N_T} = 4$ ), the final result for  $M_A = 300$  GeV is shown in Fig. 6.10. For the optimized  $W_{corr}$  window the cross-section measurement precision of 11% is obtained.

After discovery or a 'hint' of the resonant-like excess of events at LHC or ILC the Photon Collider can be used to confirm the existence and to measure the cross section for production of the new state. In this case the beam energy will also be optimized for the production of the observed resonance. Under this assumption, we estimate precision ex-

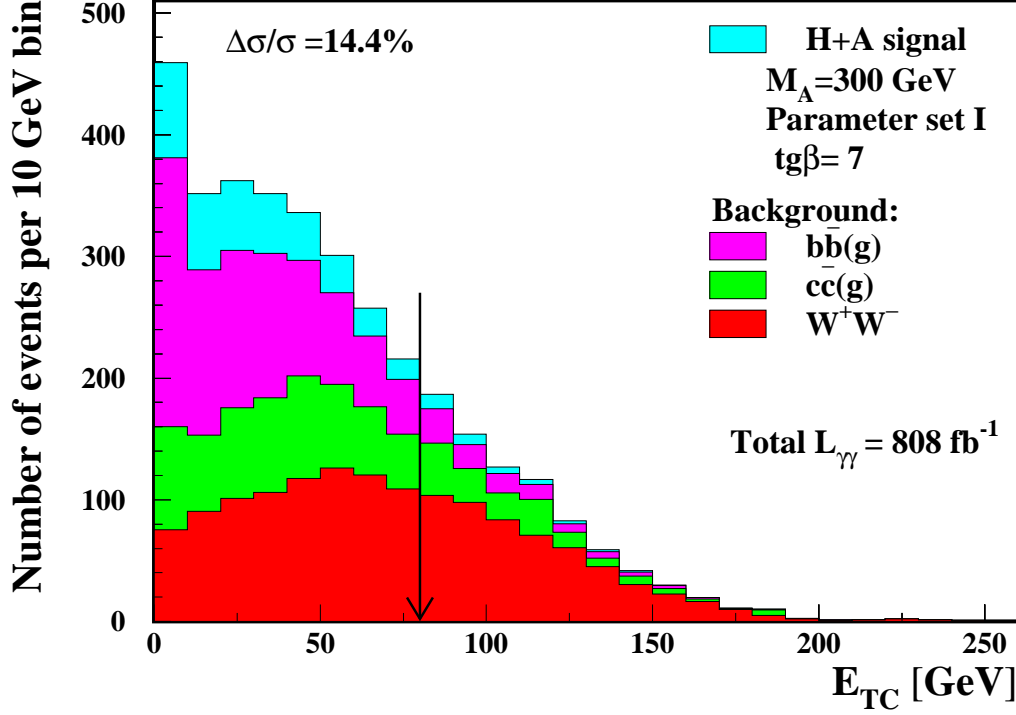


Figure 6.9: Distributions of the energy below  $\theta_{TC}$  measured in the calorimeters,  $E_{CAL}$ , for signal and background contributions, with overlaying events included.

pected for  $\gamma\gamma \rightarrow A, H \rightarrow b\bar{b}$  cross section measurement in the considered MSSM scenario after one year of experimentation. In Fig. 6.11 the precisions for all considered values of  $M_A$  are shown and compared with our previous results. Thanks to the cuts optimization better estimated precision for  $M_A = 200$  GeV has been obtained; earlier results were obtained with cuts optimized for Higgs-bosons production for  $M_A = 300$  GeV.

Presented results were also used to estimate precision of the cross-section measurement at the Photon Collider for other parameter sets described in Section 4.1. For all sets the total widths of the Higgs bosons  $A$  and  $H$  are comparable or smaller than for the set  $I$  and their masses are nearly degenerated (the mass difference is smaller or comparable with detector resolution). Precision estimates for  $\sigma(\gamma\gamma \rightarrow A, H \rightarrow b\bar{b})$  measurement for all considered parameter sets, assuming  $\tan\beta = 7$  are compared in Fig. 6.12. The most precise measurement is expected for parameter sets  $II$  and  $III$  — precision hardly depends on  $M_A$  and is about 10%. The worst measurement is expected for scenario  $IV$ , *i.e.* the one considered by the CMS collaboration.

For all considered values of  $M_A$  the dependence of the measurement precision on  $\tan\beta$  was studied and the results are shown in Fig. 6.13. The precision weakly depends on  $\tan\beta$  if parameter sets  $II$  or  $III$  are considered. In case of parameter sets  $I$  or  $IV$  the precise

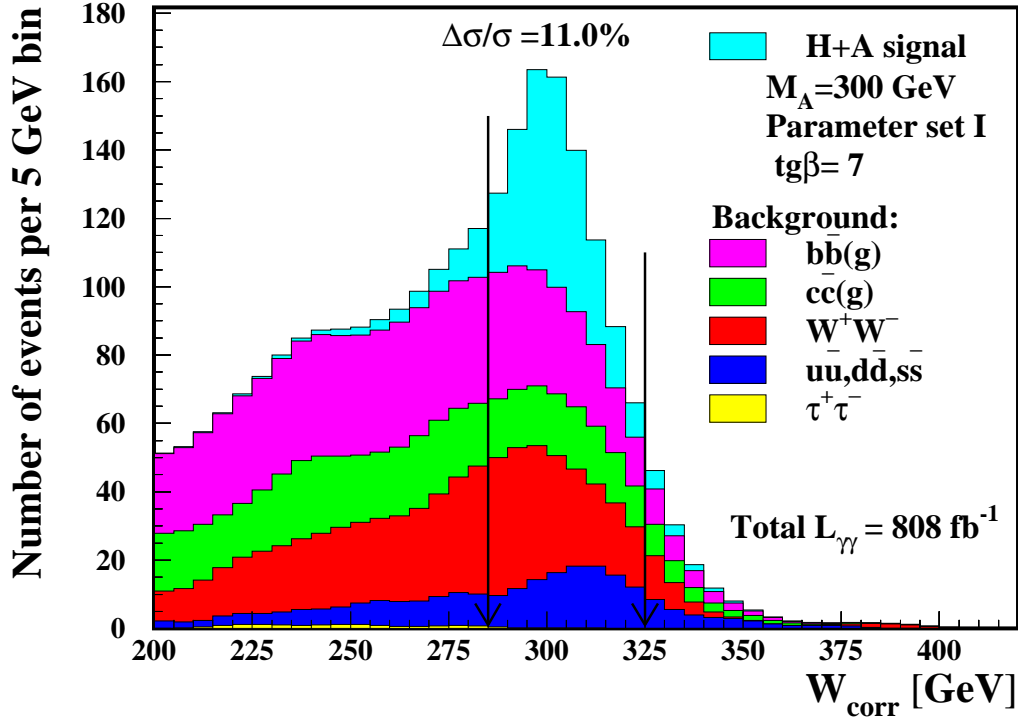


Figure 6.10: Distributions of the corrected invariant mass,  $W_{corr}$ , for signal and all considered background contributions, with overlaying events included. The best precision of 11% for  $\gamma\gamma \rightarrow A, H \rightarrow b\bar{b}$  cross section measurement is achieved in the  $W_{corr}$  window between 285 and 325 GeV.

measurement will not be possible for low  $\tan\beta$  values,  $\tan\beta \lesssim 5$ .

As already mentioned in Chapter 2 considered range of MSSM parameters covers the region of so-called LHC wedge where the expected number of reconstructed  $A$  and  $H$  production events will be too small to claim  $5\sigma$  discovery. Also the heavy MSSM Higgs-boson production signal at the ILC may not be sufficient. In such a case the Photon Collider was considered as the only machine which will be able to confirm the existence of the heavy neutral *higgses*. For  $M_A = 300$  GeV, assuming parameter set  $I$  and  $\tan\beta = 7$ , the expected statistical significance  $\delta$  of the  $A + H$  signal measurement at the Photon Collider is  $\delta = \mu_S/\sqrt{\mu_B} = 7.2$ , in the optimal mass window. The significance of the Higgs-bosons measurement,  $\delta$ , for different parameter sets considered in this analysis is shown in Fig. 6.14. The bands widths indicate the level of possible statistical fluctuations of the actual measurement:

$$\delta = \frac{\mu_S}{\sqrt{\mu_B}} \pm \sqrt{1 + \frac{\mu_S}{\mu_B}}$$

In three from the four considered MSSM scenarios, assuming  $\tan\beta = 7$ ,  $5\sigma$  discovery of heavy, neutral *higgses* will be possible in the whole range of  $M_A$ , if only the optimum beam

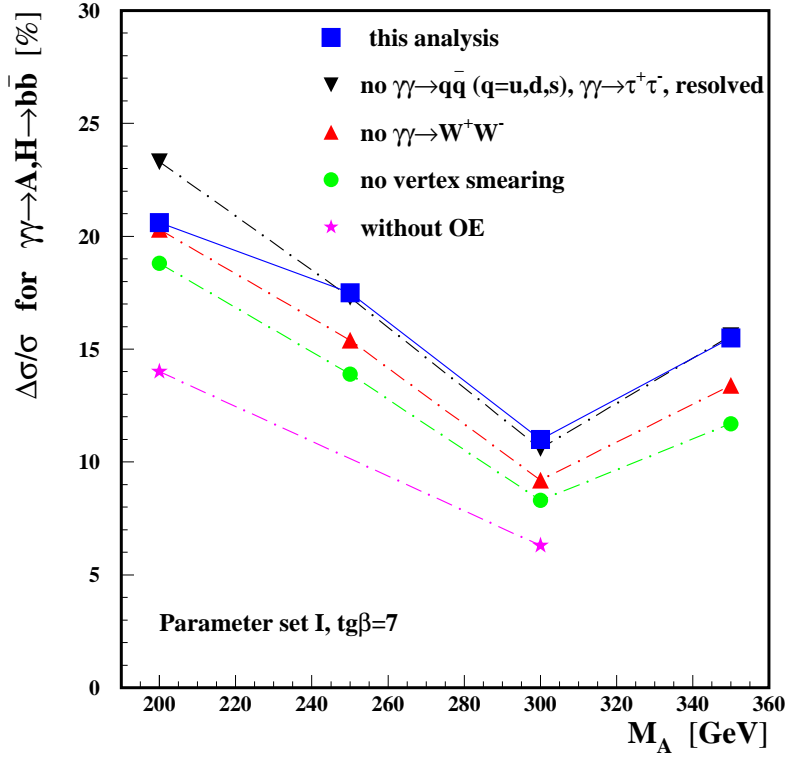


Figure 6.11: Precisions of  $\sigma(\gamma\gamma \rightarrow A, H \rightarrow b\bar{b})$  measurement for MSSM parameter set  $I$ , for  $M_A = 200\text{--}350$  GeV and  $\tan\beta = 7$ . Final results of this analysis are compared with our earlier results, which did not take into account some of the background contributions,  $\gamma\gamma \rightarrow W^+W^-$ , distribution of primary vertex or overlaying events. The lines are drawn to guide the eye.

energy is chosen (some hint for  $M_A$  value is expected from LHC and ILC measurements).

For all considered values of  $M_A$  we also studied the significance of signal measurement as a function of  $\tan\beta$ , for  $\tan\beta = 3\text{--}20$ . Results obtained for different parameter sets are compared in Fig. 6.15. The estimated lower limit of the discovery region of LHC experiments (as presented by CMS collaboration [8]) is indicated by arrows. For all parameter sets the expected statistics of signal events for  $M_A = 200\text{--}350$  GeV will be sufficient to cover most of the considered MSSM parameters space. We can conclude that for  $M_A \gtrsim 300$  GeV the Photon Collider should be able to discover Higgs bosons for much lower values of  $\tan\beta$  than experiments at the LHC.



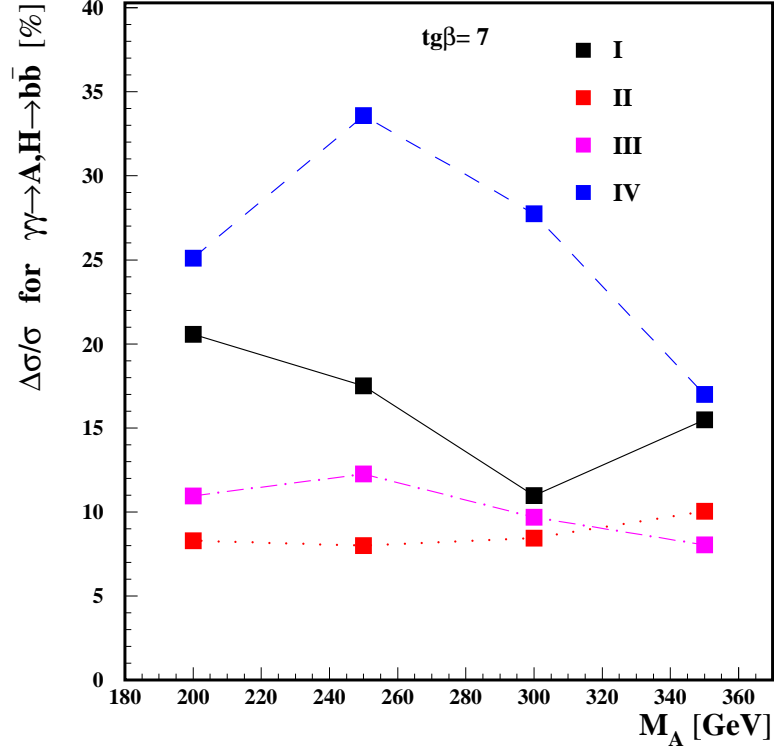


Figure 6.12: Precisions of  $\sigma(\gamma\gamma \rightarrow A, H \rightarrow b\bar{b})$  measurement are shown for MSSM parameter sets *I-IV*, for  $M_A = 200\text{--}350$  GeV and  $\tan\beta = 7$ . The lines are drawn to guide the eye.

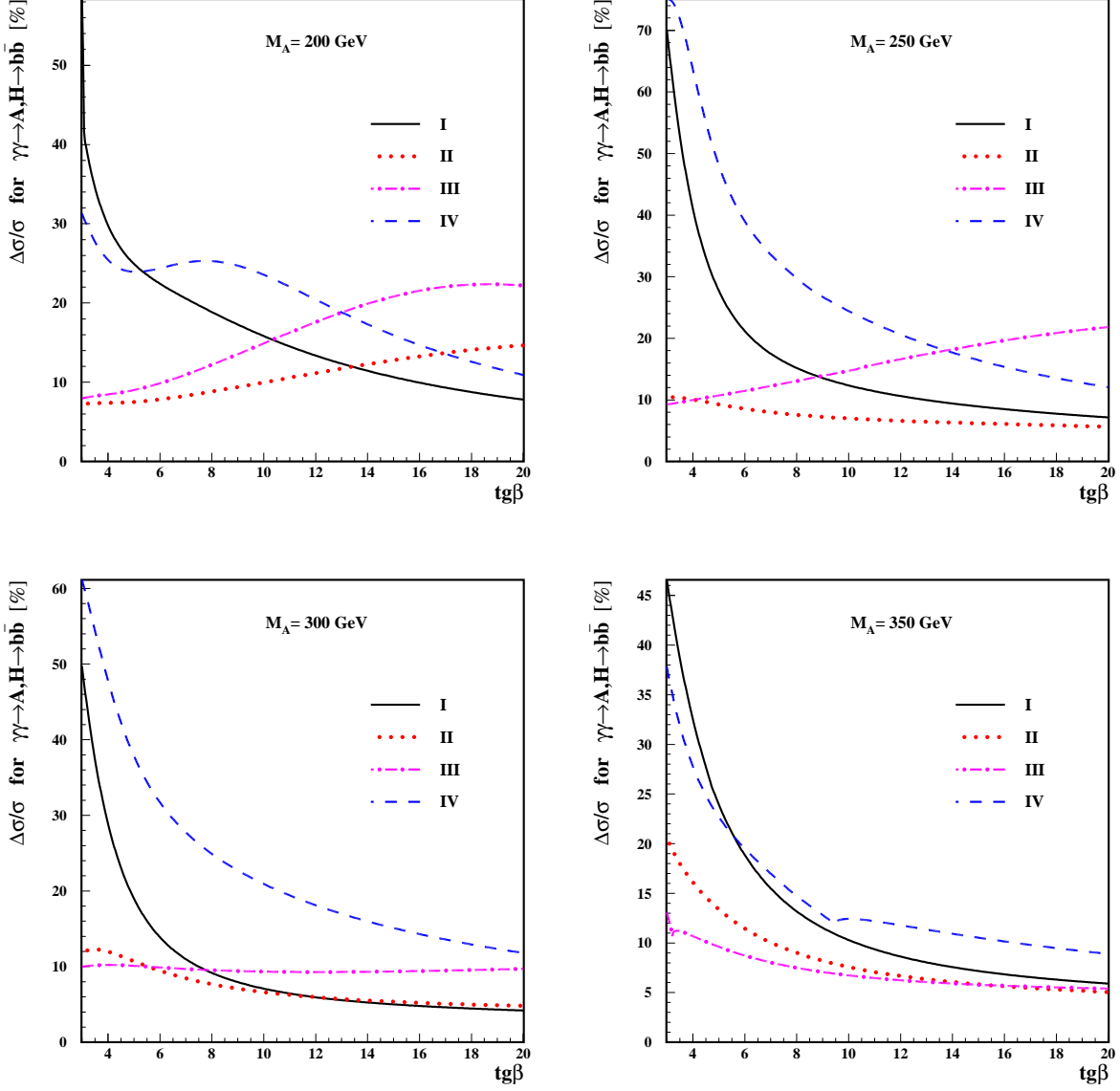


Figure 6.13: Precisions of  $\sigma(\gamma\gamma \rightarrow A, H \rightarrow b\bar{b})$  measurement are shown for  $M_A = 200, 250, 300$  and  $350$  GeV, for MSSM parameter sets *I-IV* with  $\tan\beta = 3-20$ .

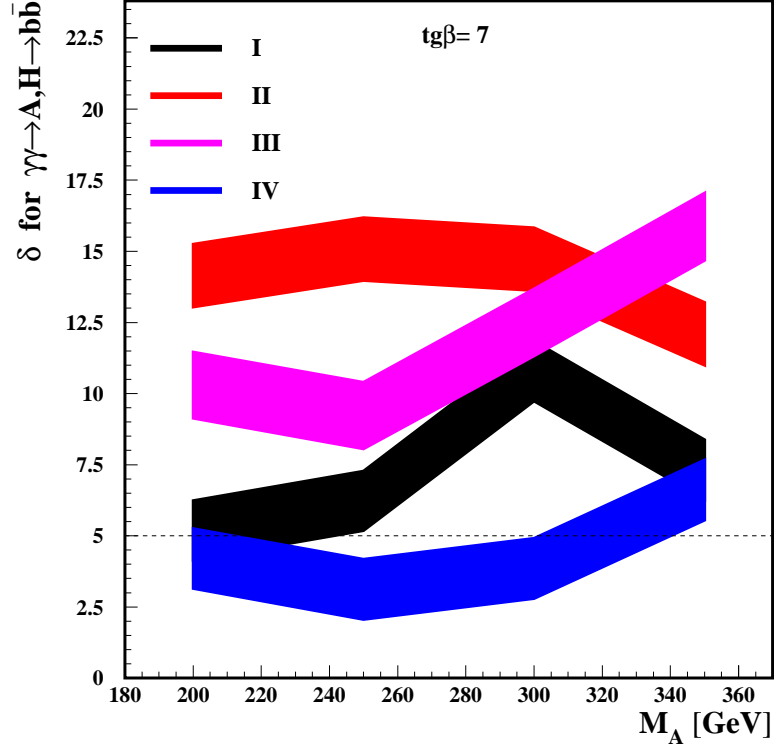


Figure 6.14: Significances of  $\sigma(\gamma\gamma \rightarrow A, H \rightarrow b\bar{b})$  measurement for MSSM parameter sets *I-IV*, for  $M_A = 200\text{--}350$  GeV and  $\tan\beta = 7$ . The band widths indicate the level of possible statistical fluctuations of the actual measurement.

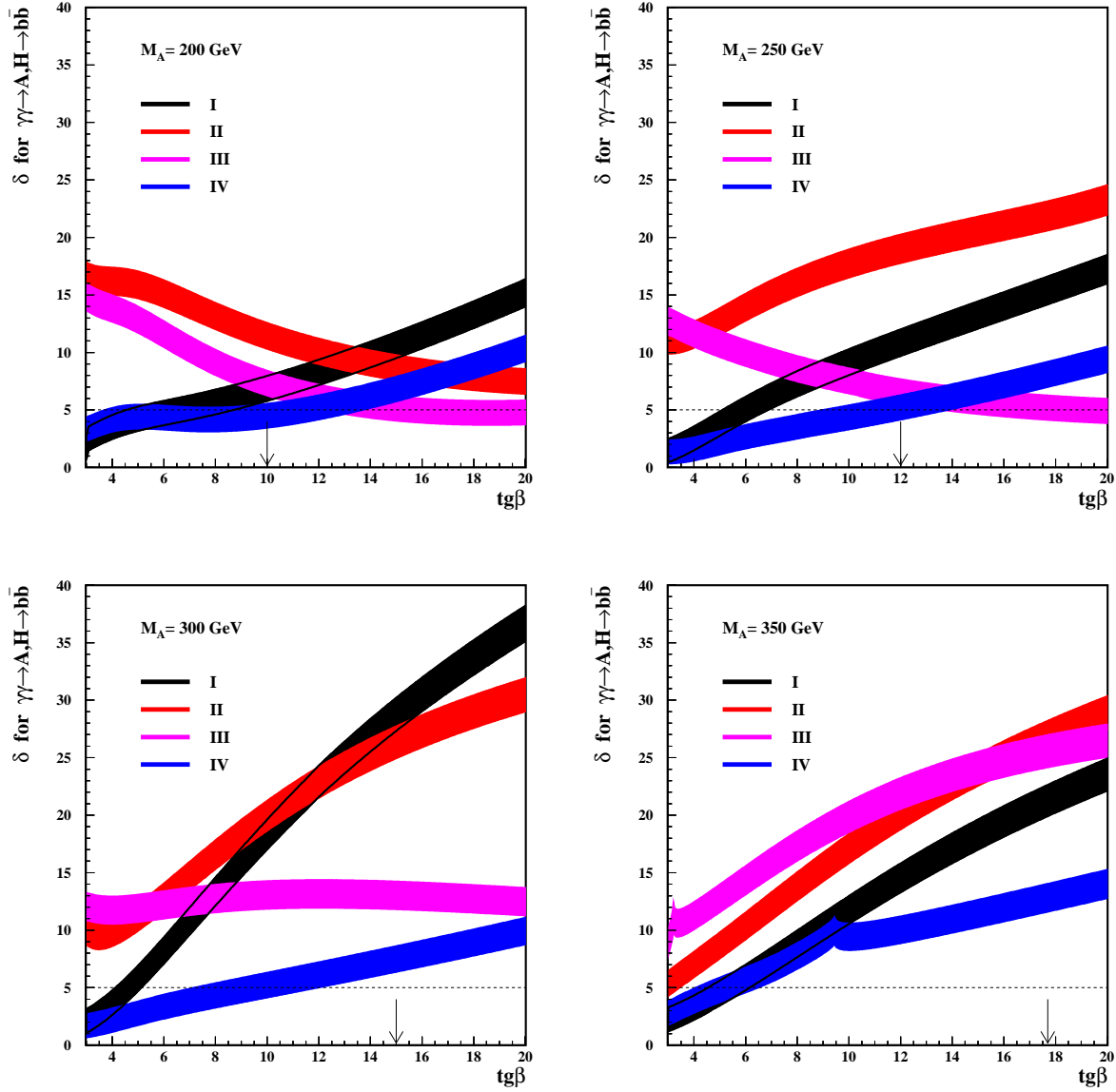


Figure 6.15: Significances of  $\sigma(\gamma\gamma \rightarrow A, H \rightarrow b\bar{b})$  measurement for MSSM parameter sets I-IV, for  $M_A = 200, 250, 300$  and  $350$  GeV, and  $\tan\beta = 3-20$ . The band widths indicate the level of possible statistical fluctuations of the actual measurement.

# Chapter 7

## Summary

Search for the Higgs boson and precise measurement of its properties are among most important tasks of all future colliders. One of the measurements crucial for understanding of the Higgs sector and for the verification of the particle physics models is the measurement of  $\Gamma(h \rightarrow \gamma\gamma)$ . The Photon Collider, which has been proposed as an extension of the  $e^+e^-$  linear collider project, is considered the best place to do this measurement.

In this thesis the first fully realistic estimates for the precision of  $\gamma\gamma \rightarrow higgs \rightarrow b\bar{b}$  cross-section measurement at the Photon Collider are obtained. Assumed photon collider parameters correspond to the superconducting Linear Collider project TESLA. The analysis is based on the realistic  $\gamma\gamma$ -luminosity spectrum simulation. Due to the high beam intensity, resulting in high  $\gamma\gamma$ -luminosity per bunch crossing, the contribution of overlaying events  $\gamma\gamma \rightarrow hadrons$  turns out to be sizable and affects event reconstruction. Crossing angle between beams resulting in the significant broadening of the interaction region is also taken into account. These two factors significantly affect the performance of the  $b$ -tagging algorithm. It is shown that the contamination of  $\gamma\gamma \rightarrow hadrons$  overlaying events in the signal can be reduced by rejecting low-angle tracks and clusters in the event. Additional cuts are proposed to suppress contributions from other background sources which are taken into account. For the realistic estimate of the heavy quark production background which is considered to be the most important one, the NLO QCD results are used. Other processes are taken into account using the LO cross sections implemented in PYTHIA:  $\tau$ -pair production, light-quark production  $\gamma\gamma \rightarrow q\bar{q}$ ,  $\gamma\gamma \rightarrow hadrons$  events (without *direct* $\times$ *direct* processes and without other events in the bunch crossing), and  $\gamma\gamma \rightarrow W^+W^-$  (with modified cross section to take into account polarization).

After optimizing selection cuts and applying correction for escaping neutrinos from  $D$ - and  $B$ -meson decays the quantity  $\Gamma(h \rightarrow \gamma\gamma)\text{BR}(h \rightarrow b\bar{b})$  for the SM Higgs boson with mass around 120 GeV can be measured with the precision of about 2% already after one year of the Photon Collider running. The systematic uncertainties of the measurement are estimated to be of the order of 2%. The statistical precision of the measurement decreases

up to 7.7% for the SM Higgs boson with mass  $M_h = 160$  GeV. For higher masses of the SM Higgs boson other decay channels are expected to give better precision of  $\Gamma(h \rightarrow \gamma\gamma)$  measurement, see *e.g.* [49].

The measurement discussed in this paper can be used to derive the partial width  $\Gamma(h \rightarrow \gamma\gamma)$ , taking  $\text{BR}(h \rightarrow b\bar{b})$  value from precise measurement at the  $e^+e^-$  International Linear Collider. With 2% accuracy on  $\Gamma(h \rightarrow \gamma\gamma)\text{BR}(h \rightarrow b\bar{b})$ , as obtained in this analysis, and assuming  $\text{BR}(h \rightarrow b\bar{b})$  will be measured to 1.5% [43], Higgs-boson partial width  $\Gamma(h \rightarrow \gamma\gamma)$  can be extracted with accuracy of about 2.5%. With this precision the measurement will be sensitive to the deviations from the SM coming from loop contributions of new heavy charged particles. For example, heavy charged *higgs* contribution in the SM-like 2HDM is expected to change  $\Gamma(h \rightarrow \gamma\gamma)$  by 5–10% [47]. Using in addition the result from the  $e^+e^-$  Linear Collider for  $\text{BR}(h \rightarrow \gamma\gamma)$  [42], one can also extract  $\Gamma_h$  with precision of 10%.

The presented analysis has been extended to the MSSM case by considering signal of heavy MSSM Higgs bosons  $A$  and  $H$  production with decays into  $b\bar{b}$ . We study masses  $M_A = 200, 250, 300$  and  $350$  GeV, and for each mass we choose an optimal  $e^-e^-$  beam energy and selection cuts, as in SM case. Following [24], we study MSSM parameter range which corresponds to the so-called “LHC wedge”, where  $A$  and  $H$  are almost degenerate in mass.

Our analysis shows that, for  $M_A \sim 300$  GeV, the cross section for the MSSM Higgs-bosons production  $\sigma(\gamma\gamma \rightarrow A, H \rightarrow b\bar{b})$  can be measured with a statistical precision of about 11% already after one year of Photon Collider running. For other considered values of  $M_A$  it turns out to be lower – from 16% to 21%. Although this result is less optimistic than the earlier estimate [24], still the photon–photon collider gives opportunity of a precision measurement of  $\sigma(\gamma\gamma \rightarrow A, H \rightarrow b\bar{b})$ , assuming that we know the mass of the Higgs boson(s). Unfortunately, separation of  $A$  and  $H$  will not be possible as the mass resolution is about 15 GeV.

A discovery of MSSM Higgs-bosons requires energy scanning or a run with a broad luminosity spectrum, perhaps followed by the run with a peaked one. We estimate the significance expected for the Higgs production measurement for four different parameter sets and for  $\tan\beta = 3\text{--}20$ . The discovery reach of the Photon Collider is compared with the estimated reach of the CMS experiment. For the optimum energy choice the photon–photon collisions allow for the discovery of the Higgs bosons even for  $\tan\beta$  values lower than the expected reach of the LHC experiments. Thus, at least partially, the Photon Collider will cover the so-called “LHC wedge”. For low  $\tan\beta$  values the measurement could probably profit from use of additional channels: decays of  $A$  and  $H$  to charginos and neutralinos, and in case of  $H$  also decays to  $hh$ .

Presented analysis takes into account all corrections which were available to date. However, some aspects of the analysis can probably be improved in the future. The first

one is the cut on the number of selected jets. In the current analysis 2 or 3 jets are required. These are the 'natural' jet multiplicities for the signal. However, when full NLO generators with 'matrix element – parton shower matching' will become available for the heavy quark background, then this study should be repeated and the cuts depending on the number of jets should be considered. Secondly, the jet-clustering algorithm with smaller  $y_{cut}$  values could be used. Narrower jets (possibly including tracks and clusters rejected by  $\theta_{TC}$ -cut) could be used in the 4-jet kinematical fit to discriminate  $\gamma\gamma \rightarrow W^+W^-$  background events more effectively. It is also not excluded that further minimization of the  $\gamma\gamma \rightarrow hadrons$  overlaying-events contribution is possible. We have not found any effect due to overlaying events on the spacial distributions of jet primary vertices, probably because tracks with largest impact parameters are rejected by the vertex fit. However, the cut on the impact parameter of single tracks and rejection of accompanying clusters could still be considered.





# Acknowledgments

First of all, I would like to thank my supervisor Aleksander Filip Żarnecki for the enormous amount of time and work he devoted to me. His ingenuity has been a constant inspiration and challenge for me. During our discussions and collaboration I have learnt a lot about physics and started to believe that I can obtain important results.

I am very grateful to Krzysztof Doroba for his friendliness and support. He introduced me to particle physics, especially to photon-photon collisions. He also encouraged me to continue my studies when I had difficult time and considered giving up.

The subject of this thesis was suggested to me by Maria Krawczyk who invited me to work on the Photon Collider. I thank her for this brave proposition, and for our fruitful collaboration.

Thinking about my journey as a physicist, I would like to thank my teacher Bożena Bugaj, who initiated me into the realm of experiments and equations, for her warmth and for my first joy from solved exercises when she was organizing 'tajne komplety' without being paid for it.

I thank my mother and my sister for their love, support and encouragement during my research work.

My special thanks go to my wife for her great love and endless patience. I am very grateful to her for taking over all my home duties during last months of my work.

This work was partially supported by the Polish Committee for Scientific Research, grant no. 2 P03B 128 25 and no. 1 P03B 040 26.



# Appendix A

## Event generation with overlaying events

In this Appendix we discuss the statistical principles of event generation, with emphasis on the possibility of having multiple events in single bunch crossing. We assume that for a given invariant mass of colliding photons,  $W_{\gamma\gamma}$ , we know how to calculate the total cross section for the process  $a$ ,  $\sigma_a(W_{\gamma\gamma})$ . In the general case, for the  $\gamma\gamma$ -luminosity spectrum (integrated over time), given by  $dL(W_{\gamma\gamma})/dW_{\gamma\gamma}$ , the expected total number of events,  $N_a$ , is:

$$N_a = \int dW_{\gamma\gamma} \frac{dL(W_{\gamma\gamma})}{dW_{\gamma\gamma}} \sigma_a(W_{\gamma\gamma}).$$

If we take the luminosity spectrum corresponding to one bunch crossing only then we obtain an average number of events of the process  $a$  per one crossing,  $\mu_a$ . In the realistic event generation one must take into account the possibility that two or more  $\gamma\gamma$  collisions in channel  $a$  take place in one crossing. Therefore in each generated event, corresponding to one bunch crossing,  $k_a$  physical events of process  $a$  should be included, where  $k_a$  is the random number from Poisson distribution with mean  $\mu_a$ :

$$P(k_a, \mu_a) = \frac{\mu_a^{k_a}}{k_a!} e^{-\mu_a}.$$

In this analysis the exact algorithm based on the Poisson distribution is used to generate  $\gamma\gamma \rightarrow \text{hadrons}$  events for which  $\mu \sim 1$ .

For small values of  $\mu_a$ ,  $\mu_a \ll 1$ , an approximation is valid in which one generates  $N_a$  bunch crossings with one event of the process  $a$  in each crossing, *i.e.* one assumes that the fraction of bunch crossings with exactly one  $a$  event is  $\mu_a$ . Actually, this fraction is smaller and is equal to  $P(k_a = 1, \mu_a) = \mu_a e^{-\mu_a}$ . Moreover, in this simple approach bunch crossings with more than one  $a$  event are neglected; they contribute to the fraction  $P(k_a > 1, \mu_a)$  of crossings. Inaccuracy of this procedure is of the order of  $\mu_a^2$ . Therefore it can be safely used for processes with  $\mu_a \ll 1$ . In this work this approach is used for following processes:  $\gamma\gamma \rightarrow \text{higgs} \rightarrow b\bar{b}$ ,  $\gamma\gamma \rightarrow Q\bar{Q}(g)$ ,  $\gamma\gamma \rightarrow q\bar{q}$ ,  $\gamma\gamma \rightarrow W^+W^-$ ,  $\gamma\gamma \rightarrow \tau^+\tau^-$  (for the process with the highest cross section,  $\gamma\gamma \rightarrow Q\bar{Q}(g)$ ,  $\mu \sim 10^{-4}$ ).

In general one would like to consider many independent physical processes. Here, to simplify the description, we assume that only three different processes have to be taken into account:  $a$ ,  $b$  and  $c$ , with  $\mu_a, \mu_b \leq 0.01$  and  $\mu_c \sim 1$ . In the exact (but very ineffective) generation algorithm one would have to include  $k_a$ ,  $k_b$  and  $k_c$  events of corresponding processes for each bunch crossing where  $k_i$  are random numbers coming from Poisson distributions  $P(k_i, \mu_i)$ . However, for small  $\mu_a$  and  $\mu_b$  one can neglect bunch crossings in which events of both process  $a$  and process  $b$  are present; the fraction of such crossings is  $P(k_a > 0, \mu_a)P(k_b > 0, \mu_b) \approx \mu_a \mu_b \leq 10^{-4}$ . Therefore only bunch crossings with  $a$  and  $c$ , or  $b$  and  $c$  processes can be considered. As already pointed out, only bunch crossings with  $k_a = 1$  and  $k_b = 1$  can be taken into account in generation. In this case  $c$  events, with  $k_c$  given by the Poisson distribution, are called *overlaying events*. However, one has to include also events with  $c$  process only. The fraction of bunch crossings with  $k_c > 0$  and  $k_a = k_b = 0$  is equal to  $P(k_c > 0, \mu_c)P(k_a = 0, \mu_a)P(k_b = 0, \mu_b)$ . As values of  $\mu_a$  and  $\mu_b$  are small  $P(k_a = 0, \mu_a)P(k_b = 0, \mu_b) \approx 1$ , and it is enough to generate a sample of  $P(k_c > 0, \mu_c)N_c/\mu_c$  bunch crossings with random number  $k_c$  ( $k_c > 0$ ) of  $c$  events in each crossing. In this analysis processes  $\gamma\gamma \rightarrow higgs \rightarrow b\bar{b}$ ,  $\gamma\gamma \rightarrow W^+W^-$  and  $\gamma\gamma \rightarrow \tau^+\tau^-$  (corresponding to processes  $a$  or  $b$ ) with overlaying events  $\gamma\gamma \rightarrow hadrons$  (process  $c$ ) are generated according to this approach.<sup>1</sup>

Slightly different procedure can be applied if process  $a$  is a subclass of overlaying event process. Let us first consider the generation of processes  $a$  with overlaying events  $c$  in more detail. The fraction of bunch crossings in which there are two  $a$  events is  $P(k_a = 2, \mu_a) \approx \mu_a^2/2$ . Using simple approach for generation of  $a$  events, *i.e.* generating  $N_a$  bunch crossings with  $k_a = 1$ , and overlaying a random number of  $c$  events,  $k_c$ , one overestimates number of crossings with one  $a$  event by about  $\mu_a^2$  and – by neglecting a possibility of having  $k_a > 1$  – underestimates number of bunch crossings with two  $a$  events by about  $\mu_a^2/2$ . However, there is also an alternative version of the generation algorithm. Instead of generating  $k_c$  overlaying events from class  $c$ , one can generate  $k_{a+c}$  overlaying events from joined class  $a+c$  where  $k_{a+c}$  is a random number from distribution  $P(k_{a+c}, \mu_a + \mu_c)$ . Then, one obtains almost correct fraction of bunch crossings with  $k_a = 1$  (about  $\mu_a - \mu_a^2$ ) and overestimates a fraction of crossings with  $k_a = 2$  (by about  $\mu_a^2/2$ ). This approach is applied in this work for processes  $\gamma\gamma \rightarrow Q\bar{Q}(g)$  and  $\gamma\gamma \rightarrow q\bar{q}$  (corresponding to the process  $a$ ) with overlaying events  $\gamma\gamma \rightarrow hadrons$  ( $a+c$ ) because the first two processes are included in generation of  $\gamma\gamma \rightarrow hadrons$  events.<sup>2</sup>

---

<sup>1</sup>When the  $\gamma\gamma \rightarrow hadrons$  process is considered as a separate background contribution (only overlaying events) the direct processes  $\gamma\gamma \rightarrow q\bar{q}$  with  $q = u, d, s, c, b$  are excluded from generation as they are taken into account individually ( $\gamma\gamma \rightarrow Q\bar{Q}(g)$  for  $Q = b, c$  and  $\gamma\gamma \rightarrow q\bar{q}$  for  $q = u, d, s$ ).

<sup>2</sup>The processes  $\gamma\gamma \rightarrow Q\bar{Q}(g)$  are included in  $\gamma\gamma \rightarrow hadrons$  events generated with PYTHIA in the LO approximation for the process  $\gamma\gamma \rightarrow q\bar{q}$  with  $q = c, b$ , and assuming unpolarized photon-photon collisions.

# Appendix B

## Influence of higher order corrections

In this Appendix we try to estimate the uncertainty of the presented results due to higher order corrections to the NLO QCD background process  $\gamma\gamma \rightarrow Q\bar{Q}(g)$ . As explained in Section 4.2, the parton shower algorithm was not applied in the generation of heavy-quark background events as it would lead to double-counting of some gluon emissions. However, we can use it to estimate influence of higher order QCD corrections which are not included in the NLO generating program. The parton shower algorithm was applied to the  $Q\bar{Q}(g)$  final state generated with the NLO code, and the full analysis including cut optimization was repeated for the SM Higgs boson with mass of 120 GeV ( $\sqrt{s_{ee}} = 210$  GeV) and for the MSSM Higgs bosons  $H$  and  $A$  for  $M_A = 300$  GeV ( $\sqrt{s_{ee}} = 419$  GeV). However, here background contributions due to  $\gamma\gamma \rightarrow \tau^+\tau^-$  and resolved  $\gamma\gamma \rightarrow \text{hadrons}$  events were not included. The cut suppressing overlaying event contribution was not varied:  $\cos\theta_{TC} = 0.85$ . As some gluon emissions are neglected in the generation without parton shower (our standard analysis), and with parton shower some emissions are double counted, we can expect that the actual event distributions will be somewhere in between. Thus, the difference between results obtained without and with parton shower can indicate the size of effects which are expected after higher QCD corrections are taken into account.

In Table B results obtained with and without parton shower are compared. The precisions of cross section measurement for both cases are nearly the same. After applying the parton shower algorithm the  $\gamma\gamma \rightarrow b\bar{b}(g)$  events have on average slightly lower  $b$ -tag values as  $B$ -mesons are slower due to the additional gluon emissions. It can be clearly seen in the analysis of SM Higgs-boson production when in both cases we obtain similar optimal region of acceptance in the  $b\text{-tag}(\text{jet}_1) \otimes b\text{-tag}(\text{jet}_2)$  plane (nearly the same efficiencies for *higgs* signal) but  $\varepsilon_{bb}$  is smaller if the parton shower algorithm is applied. Moreover, the increase of  $c\bar{c}$ -mistagging probability is observed. It is due to the fact that additional soft gluons broaden a  $c$ -jet and some tracks appear which are not present in events without parton shower. These modifications can cause the  $c$ -jet being sometimes similar to the  $b$ -jet.

$\sqrt{s_{ee}}$ [GeV]	Signal process	$\Delta\sigma/\sigma$ [%]	$\varepsilon_h$ [%]	$\varepsilon_{bb}$ [%]	$\varepsilon_{cc}$ [%]	$\varepsilon_{uds}$ [%]
210	$\gamma\gamma \rightarrow h \rightarrow b\bar{b}$	1.96 (2.03)	57 (58)	43 (50)	2.8 (2.2)	0.16 (0.16)
419	$\gamma\gamma \rightarrow A, H \rightarrow b\bar{b}$	10.6 (11.0)	59 (53)	50 (47)	5.2 (2.9)	0.6 (0.5)

Table B.1: Results for precision measurement of signal  $\gamma\gamma \rightarrow h \rightarrow b\bar{b}$  ( $M_h = 120$  GeV) and  $\gamma\gamma \rightarrow A, H \rightarrow b\bar{b}$  ( $M_A = 300$  GeV), and optimal tagging efficiencies  $\varepsilon_h$ ,  $\varepsilon_{bb}$ ,  $\varepsilon_{cc}$ , and  $\varepsilon_{uds}$ . Values obtained with parton shower algorithm applied to  $Q\bar{Q}(g)$  parton system. In parentheses values for generation without parton shower are shown (our standard analysis). All cases were subject to the same procedure with cuts and *higgs*-tagging optimization.

In case of the MSSM analysis the situation is more complicated as the wider optimal acceptance region in the  $b$ -tag( $\text{jet}_1$ ) $\otimes$  $b$ -tag( $\text{jet}_2$ ) plane is chosen if parton shower is included (greater  $\varepsilon_h$ ). Then it is advantageous to take also signal events with jets having lower  $b$ -tag value because the  $\gamma\gamma \rightarrow b\bar{b}(g)$  background events have slightly lower  $b\bar{b}$ -tagging efficiency.

We conclude that our results are not sensitive to the higher order corrections for the heavy-quark background process under assumption than these corrections do not change significantly the overall normalization of the  $\gamma\gamma \rightarrow Q\bar{Q}(g)$  cross section.

# Appendix C

## Studies on the influence of overlaying events

In this Appendix the contribution of the  $\gamma\gamma \rightarrow \text{hadrons}$  overlaying events to the hard  $\gamma\gamma$  scattering events in the detector is studied in detail. To understand better properties of overlaying events we first study particle distributions on the generator level. The expected distributions of the particle, energy and transverse energy flows in  $\cos(\theta_{particle})$ , where  $\theta_{particle}$  is the particle polar angle, are shown in Fig. C.1 for *hadron-like* $\times$ *hadron-like* events at  $\sqrt{s_{ee}} = 210$  GeV. The average number of  $\gamma\gamma \rightarrow \text{hadrons}$  events per bunch crossing,  $\mu$ , is about 0.9. All distributions are strongly forward-peaked. This behaviour, expected for soft hadron-hadron interactions, is intensified in majority of events by the strong Lorentz boost of the  $\gamma\gamma$  center of mass system. As shown in Fig. C.2 and C.3, the same behaviour is observed for *hadron-like* $\times$ *direct* and *direct* $\times$ *direct* processes for which  $\mu \approx 0.1$  and 0.01, respectively. Therefore, the cut on the particle polar angle seems to be the simplest way to reduce the contamination of particles coming from overlaying events. We studied the average contribution of overlaying events to the energy measured in the detector after a cut  $\theta_{min}$  on the minimal polar angle of particle. In Fig. C.4 and C.5 the probability distributions for the energy and transverse energy flows are shown for two  $\theta_{min}$  values. The significant decrease of the average energy and transverse energy is clearly observed: the average energy changes from around 60 GeV without  $\theta_{min}$  cut to 20 and 10 GeV for  $\theta_{min} = 80$  and 250 mrad, respectively.

After these promising results on the generator level, we studied the detector response to the overlaying events. The influence of low-angle particles can be reduced by ignoring tracks and clusters with polar angle less than  $\theta_{TC}$ . Following values of  $\theta_{TC}$  were considered: 131, 315, 450, 555, 643 and 722 mrad, corresponding to  $\cos\theta_{TC}$  values of (approximately) 0.99, 0.95, 0.90, 0.85, 0.80 and 0.75. The lowest value  $\theta_{TC} = 131$  mrad corresponds to the expected size of the mask,  $\theta_{mask}$ . Probability distributions for reconstructed energy,  $E_{rec}$ , for various values of  $\theta_{TC}$  are shown in Fig. C.6 and C.7 for

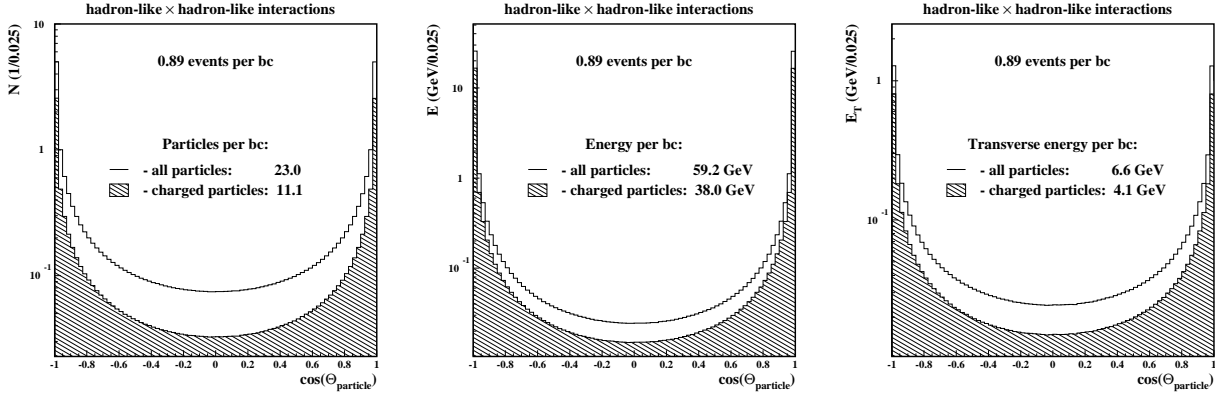


Figure C.1: Distributions of particle, energy and transverse energy flow in  $\cos(\theta_{particle})$  for *hadron-like*  $\times$  *hadron-like* case for  $\sqrt{s_{ee}} = 210$  GeV.

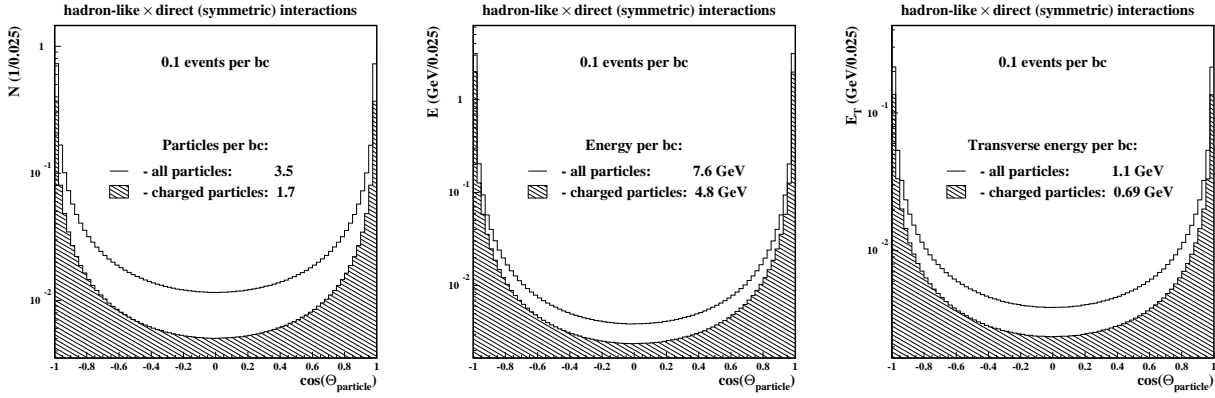


Figure C.2: Distributions of particle, energy and transverse energy flow in  $\cos(\theta_{particle})$  for *hadron-like*  $\times$  *direct* case for  $\sqrt{s_{ee}} = 210$  GeV.

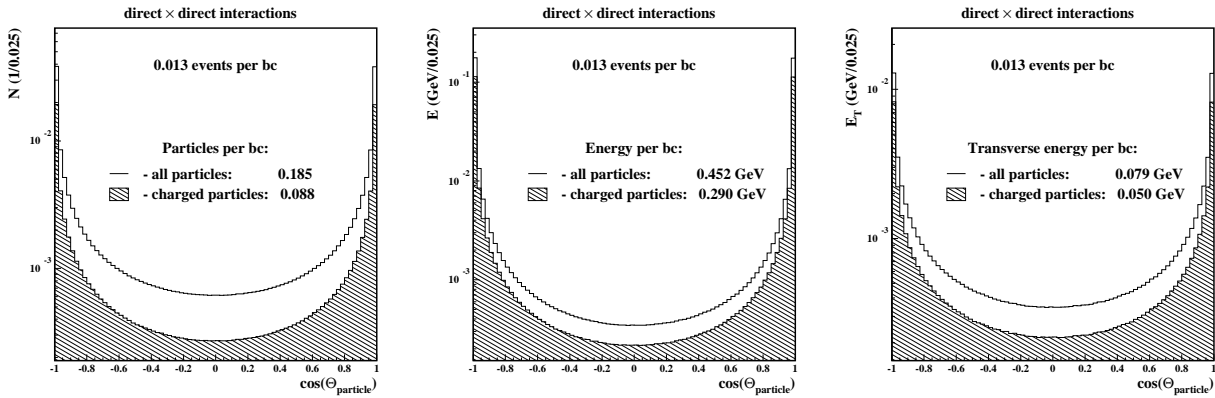


Figure C.3: Distributions of particle, energy and transverse energy flow in  $\cos(\theta_{particle})$  for *direct*  $\times$  *direct* case for  $\sqrt{s_{ee}} = 210$  GeV.



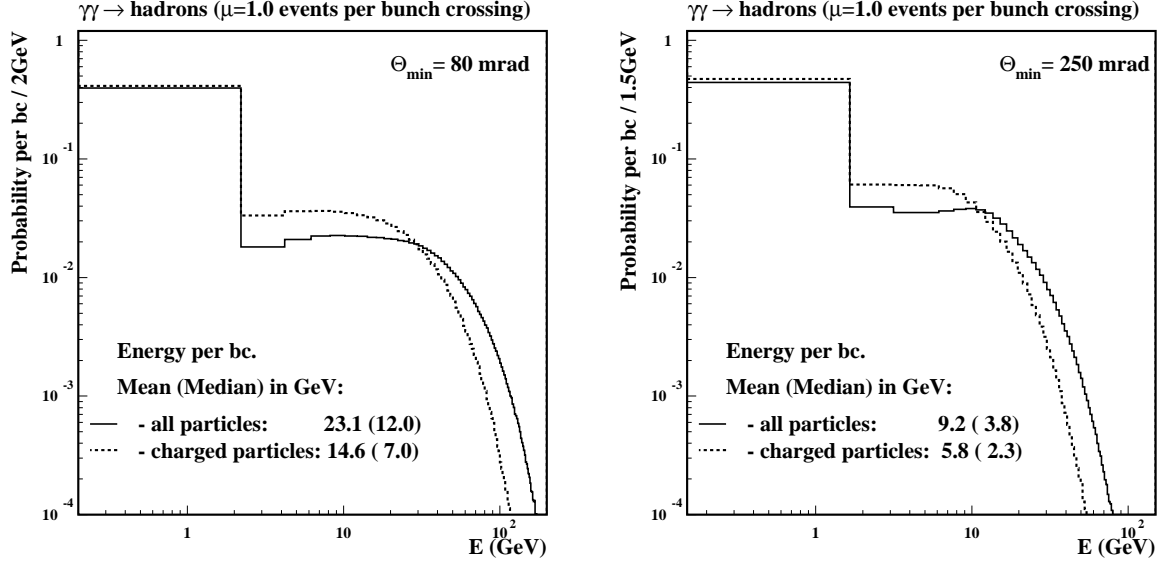


Figure C.4: Energy distributions for  $\gamma\gamma \rightarrow \text{hadrons}$  event with  $\theta_{\min} = 80$  and 250 mrad.

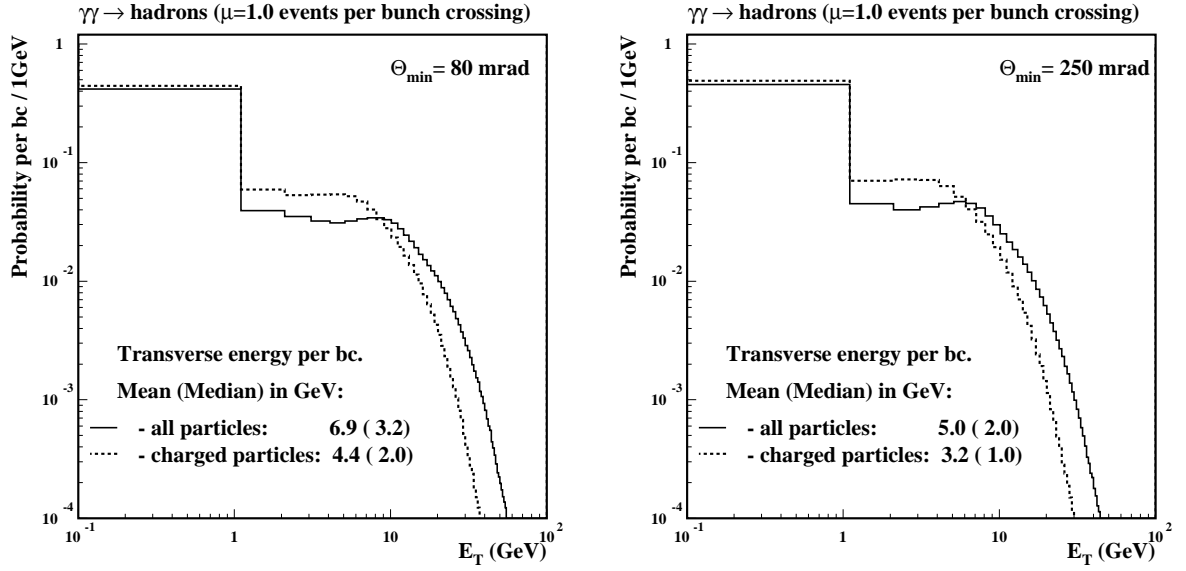


Figure C.5: Transverse energy distributions for  $\gamma\gamma \rightarrow \text{hadrons}$  event with  $\theta_{\min} = 80$  and 250 mrad.

$\sqrt{s_{ee}} = 210$  and  $419$  GeV, respectively. Probability distributions of all bunch crossings (multiple overlaying events possible) are compared with probability distributions of bunch crossing with only one  $\gamma\gamma \rightarrow \text{hadrons}$  event (visible in the detector). The low energy parts of the distributions are presented in detail in Fig. C.8 and C.9, showing a dip due to the limited detector sensitivity around  $E_{rec} \approx 0.5$  GeV. The most significant reduction of  $\gamma\gamma \rightarrow \text{hadrons}$  contamination is obtained when increasing  $\theta_{TC}$  cut from  $\theta_{mask}$  to  $\cos \theta_{TC} = 0.95$  and  $0.9$ . However, it is important to notice that the probability of observing no energy in the detector ( $E_{rec} < 0.2$  GeV) does not increase significantly with increase of  $\theta_{TC}$ . Most events remain visible in the detector although with highly reduced energy.

As the PYTHIA generator does not produce  $\gamma\gamma \rightarrow \text{hadrons}$  events for  $W_{\gamma\gamma} < 4$  GeV, we try to estimate the contribution of these events. In Fig. C.10 average energy reconstructed per one  $\gamma\gamma \rightarrow \text{hadrons}$  event,  $\langle E_{rec} \rangle$ , is shown as a function of  $W_{\gamma\gamma}$ , for  $\sqrt{s_{ee}} = 210$  GeV and  $419$  GeV. Again, the strong reduction of reconstructed energy is observed with increase of  $\theta_{TC}$ . It is worth noticing that for  $\sqrt{s_{ee}} = 210$  GeV the average reconstructed energy is slightly higher at given  $W_{\gamma\gamma}$  than for  $\sqrt{s_{ee}} = 419$  GeV. This is due to the larger boosts of the low energy  $\gamma\gamma$  events at higher  $e^-e^-$ -beam energies. However, the reconstructed energy per bunch crossing is higher for  $\sqrt{s_{ee}} = 419$  GeV as the expected number of  $\gamma\gamma \rightarrow \text{hadrons}$  events increases from about 1 to about 2 per bunch crossing. From the average numbers of overlaying events per bunch crossing and the fact that the fraction of luminosity below  $W_{\gamma\gamma} = 4$  GeV is equal approximately to 30%, we estimated that the neglected low- $W_{\gamma\gamma}$  overlaying events would contribute to no more than 0.3 GeV (on average) to the energy measured in the detector if  $\cos \theta_{TC} \approx 0.85$  is chosen.

Particles coming from overlaying events, entering the detector with the angle larger than  $\theta_{TC}$ , are expected to form jets with small relative transverse momentum,  $p_T^{jet}/E_T$ , where  $p_T^{jet}$  is the transverse momentum of the jet and  $E_T$  is the transverse energy of all energy-flow objects above  $\theta_{TC}$ . We studied reconstructed jet distributions for the  $\gamma\gamma \rightarrow h \rightarrow b\bar{b}$  and  $\gamma\gamma \rightarrow A \rightarrow b\bar{b}$  events with overlaying events included, for various values of  $\cos \theta_{TC}$ -cut. For comparison the 'ideal' measurement, *i.e.* without overlaying events (therefore using  $\theta_{TC} = \theta_{mask}$ ) was also considered. For consistency with the final analysis we required that for the jet with the highest transverse momentum an angle cut was fulfilled:  $|\cos \theta_{jet}| < 0.7$ , where  $\theta_{jet}$  is the polar angle of the jet. The  $p_T^{jet}/E_T$  distributions for jets reconstructed in  $\gamma\gamma \rightarrow h/A \rightarrow b\bar{b}$  events are shown for various values of  $\cos \theta_{TC}$  in Fig. C.11 ( $h$  production for  $\sqrt{s_{ee}} = 210$  GeV and  $M_h = 120$  GeV) and in Fig. C.12 ( $A$  production for  $\sqrt{s_{ee}} = 419$  GeV and  $M_A = 300$  GeV). For bunch crossing with  $\theta_{TC} = \theta_{mask}$  the contribution from overlaying events is clearly seen for  $p_T^{jet}/E_T < 0.1$ . Already for the cut  $\cos \theta_{TC} = 0.95$  this contamination is significantly reduced and the distribution approaches the 'ideal' one.

With increasing the  $\theta_{TC}$  cut the influence of overlaying events on the Higgs-boson

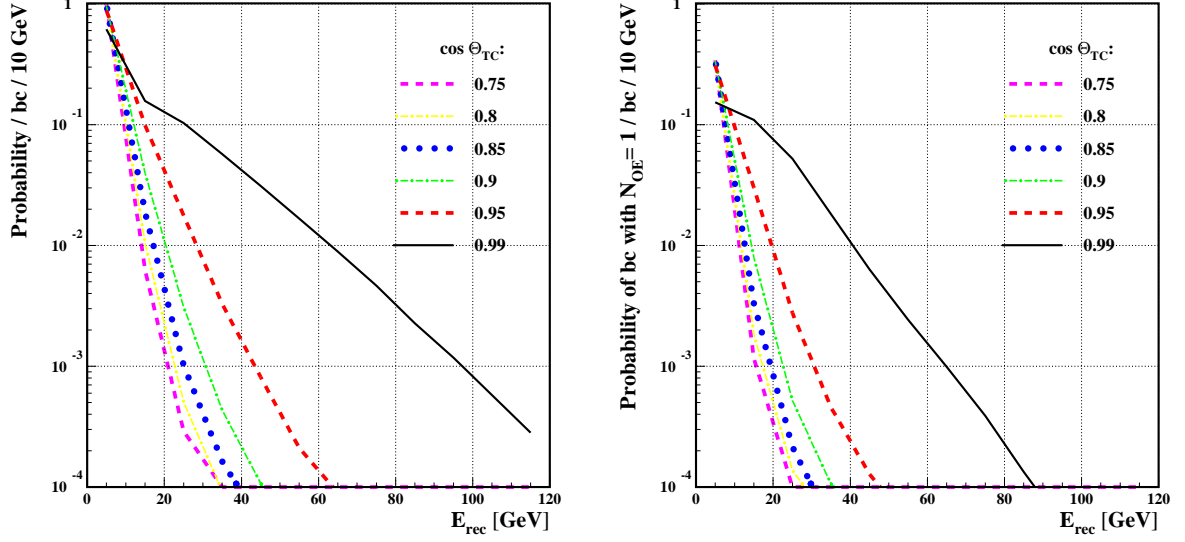


Figure C.6: Probability distribution for reconstructed energy,  $E_{rec}$ , for various values of  $\theta_{TC}$  and for  $\sqrt{s_{ee}} = 210$  GeV. On the right plot the probability for a bunch crossing with only one  $\gamma\gamma \rightarrow hadrons$  event which on the generator level has some particles above the detector mask. For clarity only centers of bins are connected by lines.

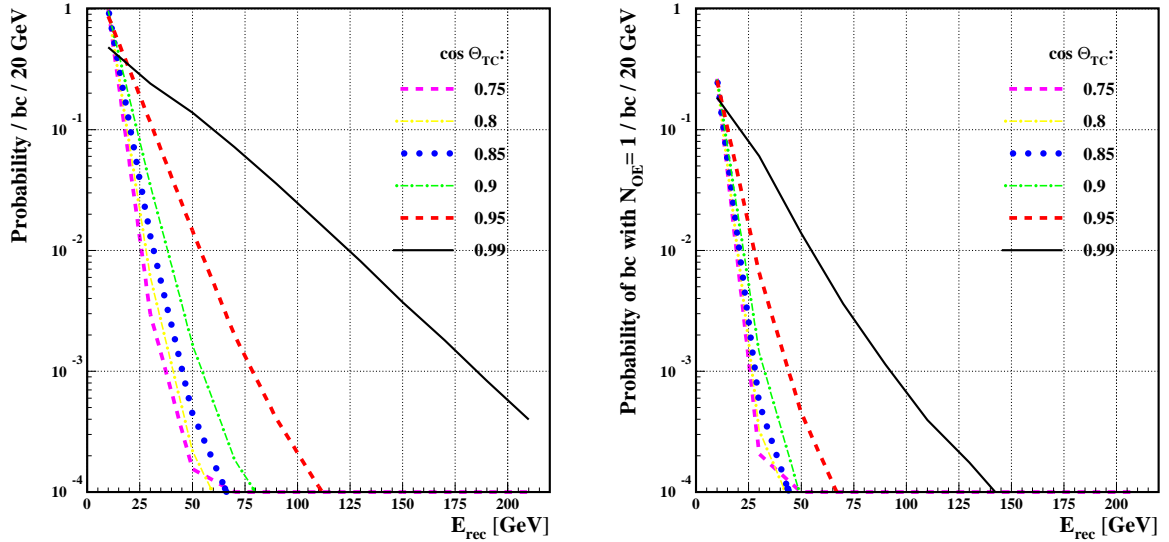


Figure C.7: Probability distribution for reconstructed energy,  $E_{rec}$ , for various values of  $\theta_{TC}$  and for  $\sqrt{s_{ee}} = 419$  GeV. On the right plot the probability for a bunch crossing with only one  $\gamma\gamma \rightarrow hadrons$  event which on the generator level has some particles above the detector mask. For clarity only centers of bins are connected by lines.

production events is decreasing. Also the lower systematic uncertainty due to  $\gamma\gamma \rightarrow \textit{hadrons}$  contribution coming from relatively large uncertainties of the cross sections for hadron-like interactions of photons can be expected. However, some tracks and clusters coming from signal event can be ignored at the same time. This will decrease mass resolution and worsen precision of the measurement. In Fig. C.11 and C.12 distributions of the reconstructed jet mass,  $M_{jet}$ , are shown for different  $\cos\theta_{TC}$  cuts. We see that for  $\cos\theta_{TC} = 0.75$  and  $0.8$  some jets lose most of their content and their mass is significantly underestimated ( $M_{jet} \lesssim 3$  GeV). Distribution obtained for  $\cos\theta_{TC} = 0.85$  nearly recovers the 'ideal' jet-mass distribution having almost the same mean value.

Finally, we checked the influence of the  $\theta_{TC}$ -cut on the Higgs-boson mass resolution. For this comparison the mass resolution was defined as the dispersion,  $\sigma$ , of the Gaussian distribution fitted to  $W_{rec} - W_{\gamma\gamma}$  or  $W_{corr} - W_{\gamma\gamma}$  distribution. The fit was performed in the range  $(\mu - \sigma, \mu + 1.5\sigma)$ , where  $\mu$  is the mean of the Gaussian distribution. As shown in Fig. C.13 and C.14, mass resolutions do not change significantly for  $\cos\theta_{TC} \leq 0.9$ . Both, the obtained resolution values and the shape of distributions show that the cut values  $\cos\theta_{TC} = 0.99$  and  $0.95$  are too weak to suppress the  $\gamma\gamma \rightarrow \textit{hadrons}$  contribution.

The full analysis (see Chapter 5) considering Higgs-boson production signal and the  $\gamma\gamma \rightarrow Q\bar{Q}(g)$  background was performed for processes  $\gamma\gamma \rightarrow h \rightarrow b\bar{b}$  (for  $M_h = 120$  GeV) and  $\gamma\gamma \rightarrow A, H \rightarrow b\bar{b}$  (for  $M_A = 300$  GeV), for all considered values of  $\cos\theta_{TC}$ . The best precision of the cross-section measurement was obtained for  $\cos\theta_{TC} = 0.85$  and  $0.9$ . Because higher  $\theta_{TC}$  cut does not deteriorate the precision, but has the advantage of reducing the systematical uncertainty due to  $\gamma\gamma \rightarrow \textit{hadrons}$  events, the value  $\cos\theta_{TC} = 0.85$  was chosen as the optimal one.

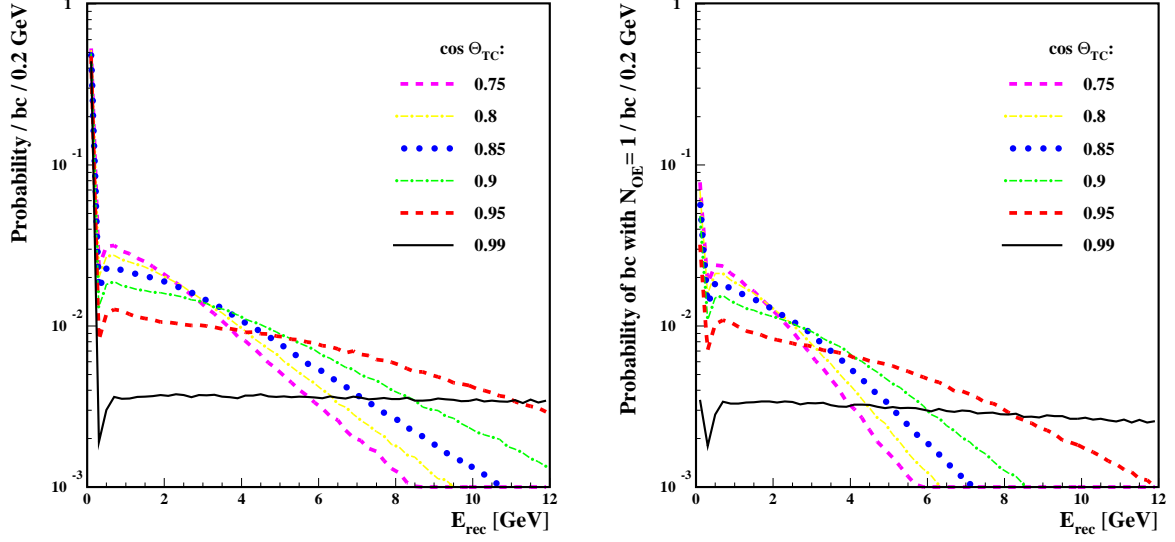


Figure C.8: Probability distribution for reconstructed energy,  $E_{rec}$ , for various values of  $\theta_{TC}$  and for  $\sqrt{s_{ee}} = 210$  GeV. On the right plot the probability for a bunch crossing with only one  $\gamma\gamma \rightarrow hadrons$  event which on the generator level has some particles above the detector mask. For clarity only centers of bins are connected by lines.

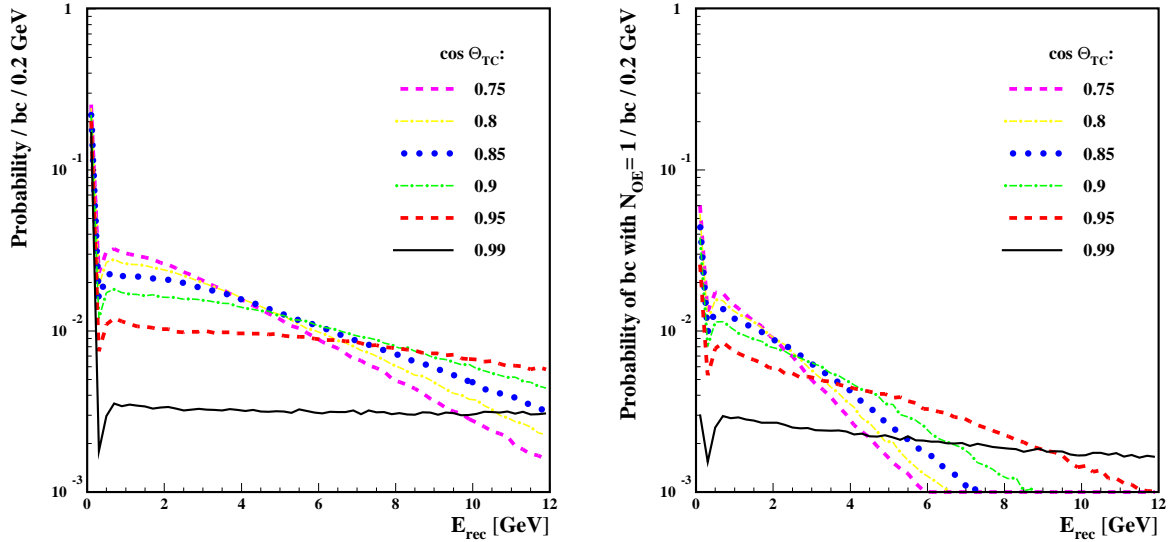


Figure C.9: Probability distribution for reconstructed energy,  $E_{rec}$ , for various values of  $\theta_{TC}$  and for  $\sqrt{s_{ee}} = 419$  GeV. On the right plot the probability for a bunch crossing with only one  $\gamma\gamma \rightarrow hadrons$  event which on the generator level has some particles above the detector mask. For clarity only centers of bins are connected by lines.

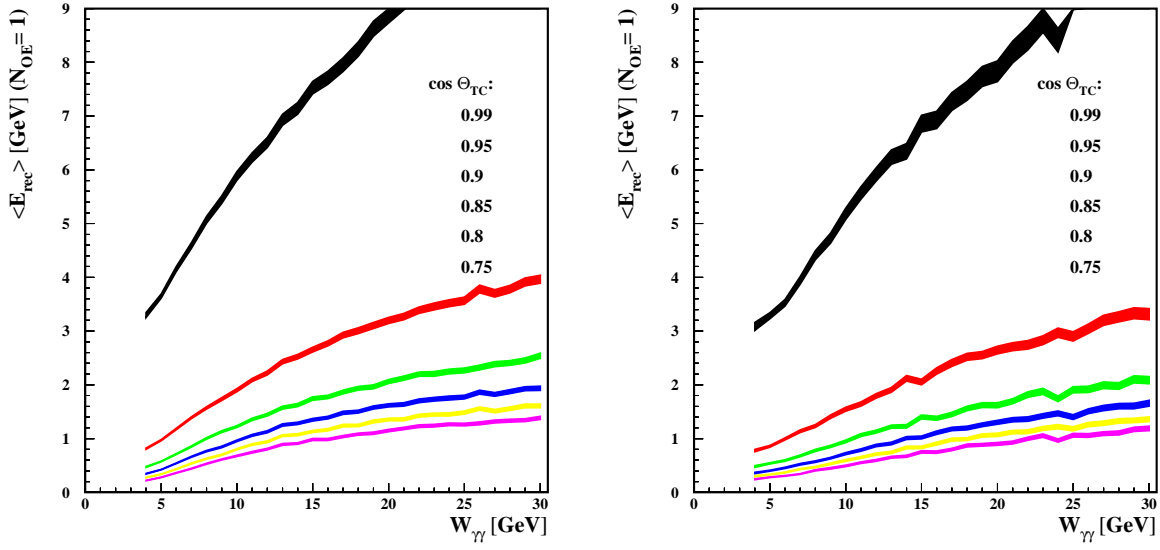


Figure C.10: Average reconstructed energy,  $\langle E_{rec} \rangle$ , dependence on  $\gamma\gamma$  invariant mass,  $W_{\gamma\gamma}$ , for bunch crossings with one  $\gamma\gamma \rightarrow \text{hadrons}$  event. Various values of  $\theta_{TC}$  for  $\sqrt{s_{ee}} = 210$  GeV (left) and 419 GeV (right) are considered.

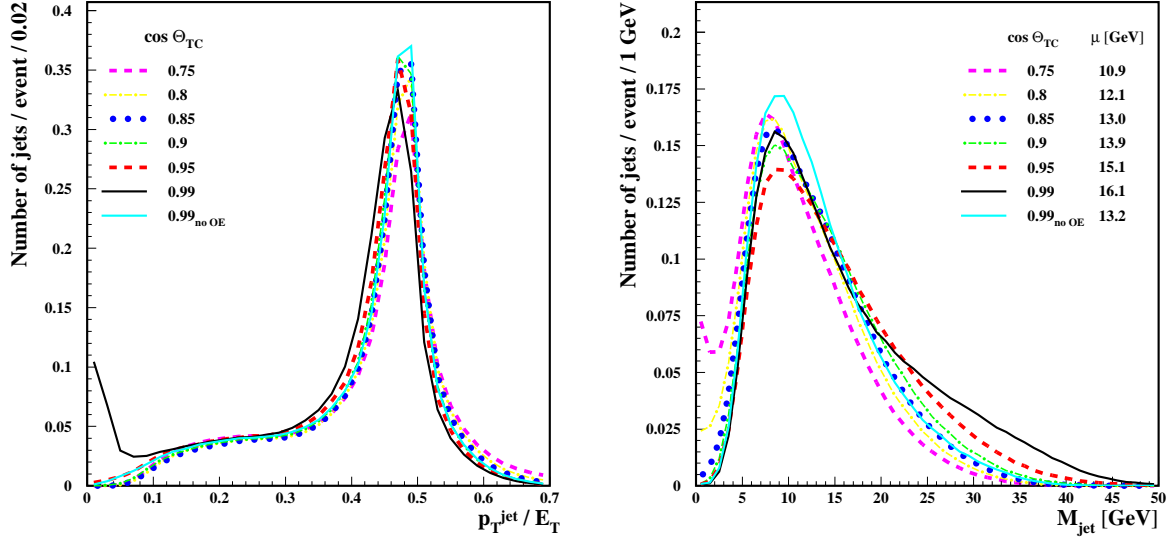


Figure C.11: Distribution of  $p_T^{jet}/E_T$  (left) and  $M_{jet}$  (right) for jets reconstructed in  $\gamma\gamma \rightarrow h \rightarrow b\bar{b}$  event, for  $\sqrt{s_{ee}} = 210$  GeV and  $M_h = 120$  GeV. Various values of  $\theta_{TC}$  are considered. For comparison results for the ideal case without overlaying events are also shown (no OE). The mean value of the  $M_{jet}$  distribution is presented for each case.

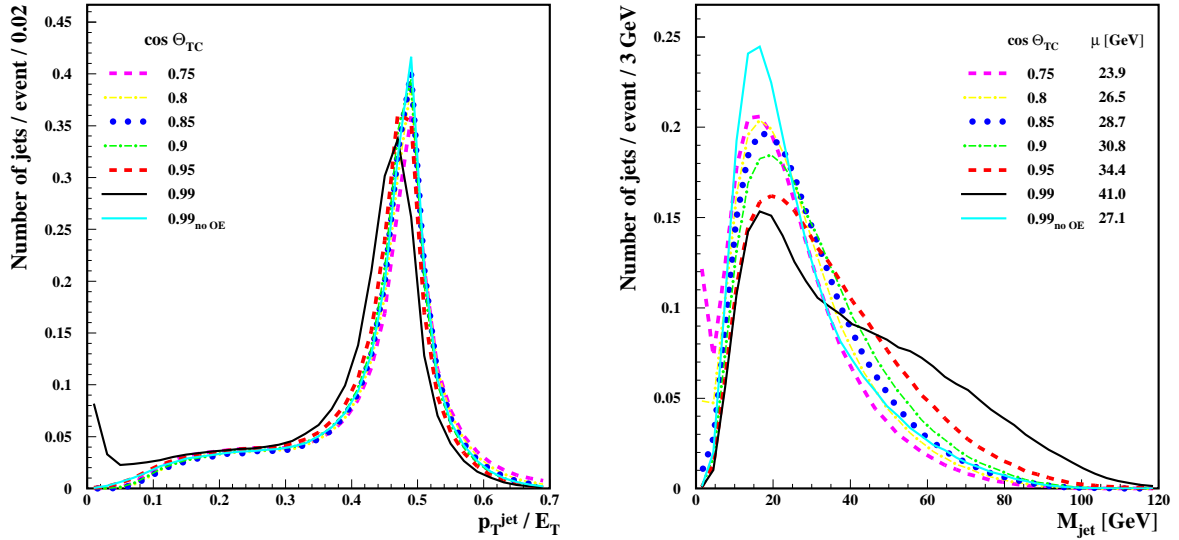


Figure C.12: Distribution of  $p_T^{jet}/E_T$  (left) and  $M_{jet}$  (right) for jets reconstructed in  $\gamma\gamma \rightarrow A \rightarrow b\bar{b}$  event, for  $\sqrt{s_{ee}} = 419$  GeV and  $M_A = 300$  GeV. Various values of  $\theta_{TC}$  are considered. Also results for the ideal case without overlaying events are shown (no OE). The mean value of the  $M_{jet}$  distribution is presented for each case.

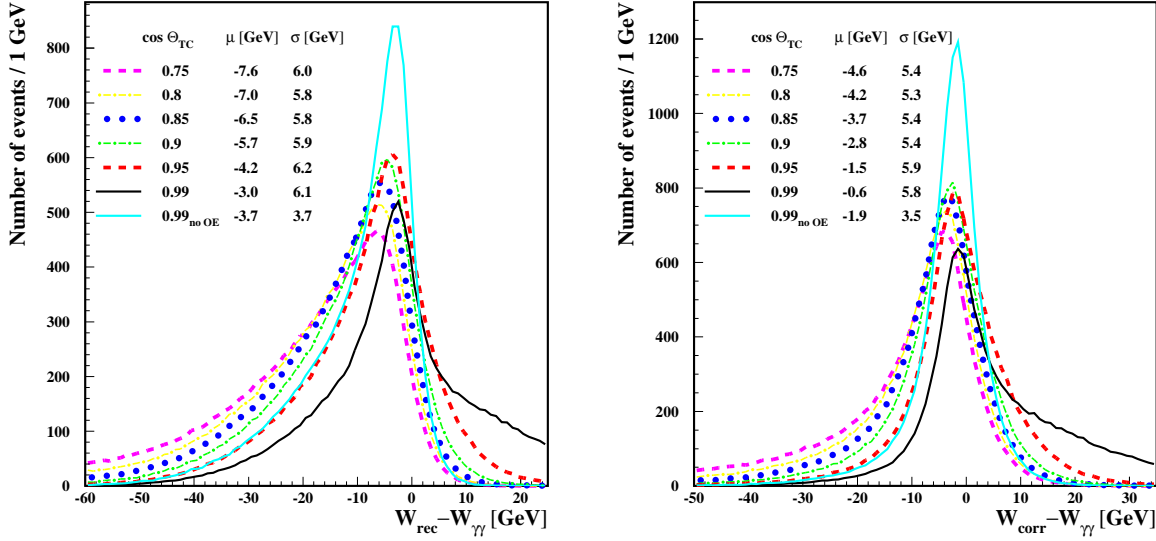


Figure C.13: Distribution of  $W_{rec} - W_{\gamma\gamma}$  (left) and  $W_{corr} - W_{\gamma\gamma}$  (right) for accepted  $\gamma\gamma \rightarrow h \rightarrow b\bar{b}$  events, for  $\sqrt{s_{ee}} = 210$  GeV and  $M_h = 120$  GeV. Various values of  $\theta_{TC}$  are considered. Also results for the ideal case without overlaying events are shown (no OE). The mean value,  $\mu$ , and the dispersion,  $\sigma$ , of the fitted Gaussian distribution is presented for each case. The fit was performed in the range  $(\mu - \sigma, \mu + 1.5\sigma)$ .

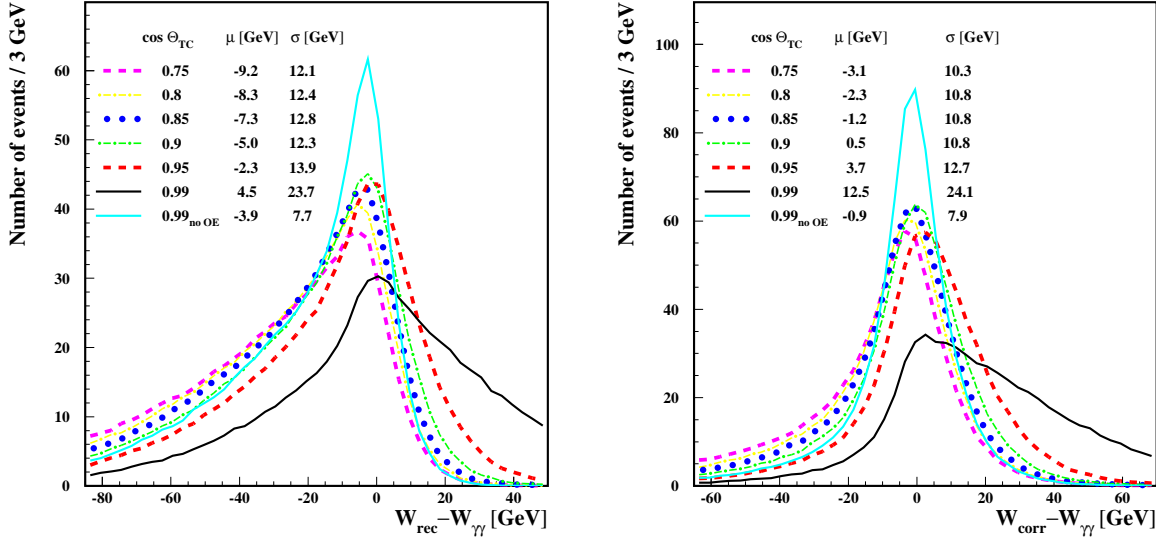


Figure C.14: Distribution of  $W_{rec} - W_{\gamma\gamma}$  (left) and  $W_{corr} - W_{\gamma\gamma}$  (right) for accepted  $\gamma\gamma \rightarrow A \rightarrow b\bar{b}$  events, for  $\sqrt{s_{ee}} = 419$  GeV and  $M_A = 300$  GeV. Various values of  $\theta_{TC}$  are considered. Also results for the ideal case without overlaying events are shown (no OE). The mean value,  $\mu$ , and the dispersion,  $\sigma$ , of the fitted Gaussian distribution is presented for each case. The fit was performed in the range  $(\mu - \sigma, \mu + 1.5\sigma)$ .



# Appendix D

## ORLOP

In this Appendix we describe the package ORLOP (OverLaying events for Photon collider) which was developed to take  $\gamma\gamma \rightarrow \text{hadrons}$  overlaying events into account in our analysis. The package includes subroutines which read in the luminosity spectra for  $\gamma\gamma$  collisions, appropriately rescale energies of beam photons (if necessary), generate  $\gamma\gamma \rightarrow \text{hadrons}$  events with variable beam energies, and add random number of the overlaying events to the earlier generated events of the studied hard scattering process.

Luminosity spectra obtained from the full simulation of  $\gamma\gamma$  collisions [56] are used to account properly for the low energy part of the spectrum. The results of the simulations are available only for three values of  $e^-e^-$  invariant mass,  $\sqrt{s_{ee}} = 200, 500$  and  $800$  GeV. The luminosity spectrum for user-defined value of  $\sqrt{s'_{ee}}$  is obtained by rescaling photon energies from the closest set by the factor  $E'_\gamma{}^{\text{max1}}/E_\gamma{}^{\text{max1}}$ , where  $E'_\gamma{}^{\text{max1}}$  and  $E_\gamma{}^{\text{max1}}$  are maximal energies of photons coming from electrons scattering off one laser photon for  $\sqrt{s'_{ee}}$  and  $\sqrt{s_{ee}}$ , respectively. To obtain  $E'_\gamma{}^{\text{max1}}$  and  $E_\gamma{}^{\text{max1}}$  values the COMPAZ program is used [57]. The ORLOP package can be easily extended to provide overlaying events also to  $e^+e^-$  collisions if the beamstrahlung photon spectrum is implemented.

The main program `gen_orlop`, running as a separate process, uses PYTHIA to generate  $\gamma\gamma \rightarrow \text{hadrons}$  events with variable beam energies, according to the realistic luminosity spectrum. As PYTHIA sometimes does not succeed to hadronize events with very low invariant mass, `gen_orlop` uses only  $\gamma\gamma$  collisions with  $W_{\gamma\gamma} > W_{\gamma\gamma}^{\text{min}} = 4$  GeV (see Appendix C for detailed discussion). The program sets following values for PYTHIA steering variables: `MSTP(14)=10` to properly include all kinds of real photon interactions, and `MSEL=2` to switch on elastic and diffractive processes. The crossing angle and the interaction point distribution are taken into account. At the beginning the program is run for 50000 events to calculate more precisely internal PYTHIA weights which influence contributions of various event classes. The calculated total cross section is used to determine the average number of overlaying events per bunch crossing,  $\mu$ .

The subroutine `add_orlop` is called to include overlaying events during generation

of the considered processes. This subroutine adds particles which are provided by the program `gen_orlop` to the PYTHIA event record. The call sequence of `add_orlop` is shown in the following listing where only parts relevant for use of ORLOP are present.

```
*      Example of ORLOP use:
*      Higgs-boson production 'gamma gamma -> h -> b bbar'
*      with overlaying events 'gamma gamma -> hadrons'.
      program produce_higgs_with_oe

*      Set Higgs-boson production 'gamma gamma -> h -> b bbar'

*      Initialization of ORLOP
      call add_orlop(1,ibeam,sqrts_ee,n_oe_per_bc)

*      Additional information (optional call)
      call add_orlop(2,n_collisions,luminosity,cross_sec)

*      Loop over bunch crossings
      do ibc=1,n_bc

*          Set photons energies for 'gamma gamma -> h -> b bbar'

*          Generate 'gamma gamma -> h -> b bbar' event
          call pyevnt

*          Add overlaying events 'gamma gamma -> hadrons'
          call add_orlop(3,n_oe,e_oe,pz_oe)

      enddo

*      End of loop over bunch crossings

*      Stop ORLOP
      call add_orlop(4,n_oe_tot,n_rewind,cross_sec)

      end
```

In calls of the subroutine `add_orlop(iflag,ivar,var1,var2)` the action undertaken and also the meaning of variables `ivar`, `var1`, `var2` depend on the value of the first parameter `iflag` as explained below.

The package ORLOP, which contains also a manual, shell scripts for convenient running of programs, and two examples of generator-level analysis, will be made publicly available after publication of results obtained in this thesis.

- iflag=1** Initialization. The main parameters for  $\gamma\gamma \rightarrow \textit{hadrons}$  generation are passed to the **gen\_orlop** program. Variables **ivar** and **var1** should be equal to the beam type and  $\sqrt{s_{ee}}$ , respectively. These – together with **iflag** – are the only input parameters. Beam type is at the moment defined only for  $\gamma\gamma$  collisions in the Photon Collider at TESLA. Variable **var2** is set to the average number of overlaying events per bunch crossing,  $\mu$ , calculated by **gen\_orlop**.
- iflag=2** Optional call allowing to obtain additional information from ORLOP. On return, variable **ivar** is equal to the number of beam collisions which are available in the simulated set. Variables **var1** and **var2** are equal to the luminosity of used spectrum [ $\text{pb}^{-1}\text{s}^{-1}$ ] and to the  $\gamma\gamma \rightarrow \textit{hadrons}$  cross section [pb].
- iflag=3** The call which actually adds overlaying events to the event record. The returned value of variable **ivar** is equal to the number of  $\gamma\gamma \rightarrow \textit{hadrons}$  events added. This is a random number from Poisson distribution with mean  $\mu$  (see description of **iflag=1**). Variables **var1** and **var2** are set to the total energy and to the longitudinal momentum of overlaying events. Before overlaying events are added all undetectable objects (except neutrinos) are removed from event record with call **pyedit(1)**.
- iflag=4** Terminate  $\gamma\gamma \rightarrow \textit{hadrons}$  generation by stopping **gen\_orlop**. Summary of overlaying events generation is returned. Variable **ivar** is set to the number of all added  $\gamma\gamma \rightarrow \textit{hadrons}$  events. Variable **var1** is equal to the number of times the available set of beam collisions was used. Variable **var2** is equal to the  $\gamma\gamma \rightarrow \textit{hadrons}$  final value of the cross section [pb] calculated by PYTHIA; this can be compared to the value provided with **iflag=2** to check stability of the result.



# Bibliography

- [1] B. Badelek *et al.*, Int. J. Mod. Phys. A 19 (2004) 5097, hep-ex/0108012.
- [2] C. Adolphsen *et al.*, LBNL-5424, SLAC-474.
- [3] N. Toge (ed.), KEK Report 2003-7.
- [4] I. Watanabe *et al.*, KEK Report 97-17.
- [5] J.-E. Augustin *et al.*, <http://www.interactions.org/pdf/ITRPexec.pdf>.
- [6] ATLAS Coll., Technical Design Report, CERN-LHCC 99-14 (1999).  
CMS Coll., Technical Proposal, CERN-LHCC 94-38 (1994).
- [7] S. Gentile, ATL-PHYS-2004-009.
- [8] S. Abdullin *et al.*, CMS NOTE 2003/033.
- [9] J. A. Aguilar-Saavedra *et al.*, hep-ph/0106315.
- [10] J. F. Gunion, H. E. Haber, SCIPP-90-22.
- [11] F. Richard, LAL-91-62.
- [12] D. L. Borden, D. Bauer, D. O. Caldwell, SLAC-PUB-5715.
- [13] J. F. Gunion, H. E. Haber, Phys. Rev. D 48 (1993) 5109.
- [14] D. L. Borden, D. A. Bauer, D. O. Caldwell, Phys. Rev. D 48 (1993) 4018.
- [15] D. L. Borden, V. A. Khoze, W. J. Stirling, J. Ohnemus, Phys. Rev. D 50 (1994) 4499, hep-ph/9405401

- [16] V. A. Khoze, hep-ph/9504348.
- [17] G. Jikia, A. Tkabladze, Nucl. Instrum. Meth. A 355 (1995) 81; Phys. Rev. D 54 (1996) 2030, hep-ph/9406428.
- [18] G. Jikia, A. Tkabladze, Phys. Rev. D 54 (1996) 2030, hep-ph/9601384.
- [19] T. Ohgaki, T. Takahashi, I. Watanabe, Phys. Rev. D 56 (1997) 1723, hep-ph/9703301.
- [20] T. Ohgaki, T. Takahashi, I. Watanabe, T. Tauchi, Int. J. Mod. Phys. A 13 (1998) 2411.
- [21] M. Melles, W. J. Stirling, Phys. Rev. D 59 (1999) 94009; Eur. Phys. J. C 9 (1999) 101, hep-ph/9807332.  
M. Melles, W. J. Stirling, V. A. Khoze, Phys. Rev. D 61 (2000) 54015, hep-ph/9907238.  
M. Melles, Nucl. Instrum. Meth. A 472 (2001) 128, hep-ph/0008125.
- [22] M. M. Mühlleitner, hep-ph/0008127.
- [23] G. Jikia, S. Söldner-Rembold, Nucl. Instrum. Meth. A 472 (2001) 133, hep-ex/0101056.
- [24] M. M. Mühlleitner, M. Krämer, M. Spira, P. M. Zerwas, Phys. Lett. B 508 (2001) 311, hep-ph/0101083.
- [25] D. M. Asner, J. B. Gronberg, J. F. Gunion, Phys. Rev. D 67 (2003) 035009, hep-ph/0110320.
- [26] M. M. Velasco *et al.*, hep-ex/0111055.
- [27] P. Nieżurawski, A.F. Żarnecki, M. Krawczyk, Acta Phys. Polon. B 34 (2003) 177, hep-ph/0208234.
- [28] P. Nieżurawski, A. F. Żarnecki, M. Krawczyk, hep-ph/0211455.
- [29] P. Nieżurawski, A. F. Żarnecki, M. Krawczyk, hep-ph/0307180.

- [30] P. Nieżurawski, A.F. Żarnecki, M. Krawczyk, hep-ph/0307183.
- [31] A. Rosca, K. Mönig, hep-ph/0310036.
- [32] J. F. Gunion, H. E. Haber, G. Kane, S. Dawson, The Higgs Hunters' Guide, Addison-Wesley, Reading, MA, 1990.
- [33] M. Carena, H. E. Haber, Prog. Part. Nucl. Phys. 50 (2003) 63, hep-ph/0208209.
- [34] Particle Data Group, Phys. Lett. B 592 (2004).
- [35] P. Higgs, Phys. Lett. 12 (1964) 132; Phys. Rev. 145 (1966) 1156.
- [36] I. J. R. Aitchison, A. J. G. Hey, Gauge Theories in Particle Physics, Adam Hilger Ltd, Bristol.
- [37] S. P. Martin, hep-ph/9709356.
- [38] LEP Electroweak Working Group, <http://lepewwg.web.cern.ch/> (status of winter 2005).
- [39] LEP Higgs Working Group, Phys. Lett. B 565 (2003) 61.
- [40] L. Zivkovic, ATL-PHYS-2004-023.
- [41] D. Zeppenfeld, R. Kinnunen, A. Nikitenko, E. Richter-Was, hep-ph/0002036.
- [42] E. Boos, J. C. Brient, D. W. Reid, H. J. Schreiber, R. Shanidze, Eur. Phys. J. C 19 (2001) 455, hep-ph/0011366.
- [43] J.-C. Brient, LC-PHSM-2002-003.  
M. Battaglia, hep-ph/9910271.
- [44] A. Djouadi, V. Driesen, W. Hollik, J. I. Illana, Eur. Phys. J. C 1 (1998) 149, hep-ph/9612362.
- [45] D. Asner *et al.*, hep-ph/0208219.

- [46] H. E. Haber, hep-ph/9505240.
- [47] I. F. Ginzburg, M. Krawczyk, P. Osland, Nucl. Instrum. Meth. A 472 (2001) 149, hep-ph/0101229; hep-ph/0101331.
- [48] P. Nieżurawski, A. F. Żarnecki, M. Krawczyk, Acta Phys. Polon. B 36 (2005) 833, hep-ph/0410291.
- [49] P. Nieżurawski, A. F. Żarnecki, M. Krawczyk, JHEP 0211 (2002) 034, hep-ph/0207294
- [50] C. P. W. Group *et al.*, hep-ph/0412251.
- [51] V. Barger, M. S. Berger, J. F. Gunion, T. Han, hep-ph/9504330.
- [52] R. Brinkmann *et al.*, DESY-01-011.
- [53] I. F. Ginzburg, G. L. Kotkin, V. G. Serbo, V. I. Telnov, Pizma ZhETF 34 (1981) 514, JETP Lett. 34 (1982) 491; Preprint INP 81-50, Novosibirsk, 1981 and Nucl. Instrum. Meth. A 205 (1983) 47; Preprint INP 81-102, Novosibirsk, 1981.  
I. F. Ginzburg, G. L. Kotkin, S. L. Panfil, V. G. Serbo, V. I. Telnov, Nucl. Instrum. Meth. A 219 (1984) 5.  
V. I. Telnov, Nucl. Instrum. Meth. A 294 (1990) 72.
- [54] V. I. Telnov, Nucl. Instrum. Meth. A 472 (2001) 43, hep-ex/0010033.
- [55] V. I. Telnov, Nucl. Instrum. Meth. A 355 (1995) 3.
- [56] V. I. Telnov, <http://www.desy.de/~telnov/stmalo/stmalo1.ps.gz> (talk);  
<http://www.desy.de/~telnov/ggtesla/spectra/> (simulations).
- [57] A. F. Żarnecki, Acta Phys. Polon. B 34 (2003) 2741, hep-ex/0207021.
- [58] I. F. Ginzburg, G. L. Kotkin, Eur. Phys. J. C 13 (2000) 295.
- [59] R. B. Palmer, SLAC-PUB-4707.



- [60] T. Behnke *et al.*, DESY-01-011.
- [61] M. Pohl, H. J. Schreiber, DESY-02-061, hep-ex/0206009.
- [62] T. Behnke, G. Blair, K. Mönig, M. Pohl, LC-TOOL-2001-005.
- [63] G. Belanger, F. Boudjema, Phys. Lett. B 288 (1992) 210.
- [64] S. Catani, Yu. L. Dokshitzer, M. Olsson, G. Turnock, B. R. Webber, Phys. Lett. B 269 (1991) 432.
- [65] R. Hawkings, LC-PHSM-2000-021-TESLA.
- [66] S. M. Xella Hansen, D. J. Jackson, R. Hawkings, C. Damerell, LC-PHSM-2001-024.
- [67] T. Kuhl, K. Harder,  
<http://www-dapnia.cea.fr/ecfadesy-stmalo/Sessions/Higgs/session1/kuhl.ps> (talk).
- [68] D. J. Jackson, Nucl. Instr. Meth. A 388 (1997) 247.
- [69] D. Buskulic *et al.*, Phys. Lett. B 313 (1993) 535.
- [70] A. Djouadi, J. Kalinowski, M. Spira, Comput. Phys. Commun. 108 (1998) 56,  
hep-ph/9704448.
- [71] T. Sjöstrand, P. Eden, C. Friberg, L. Lonnblad, G. Miu, S. Mrenna, E. Norrbin,  
Comput. Phys. Commun. 135 (2001) 238, hep-ph/0108264.
- [72] V. Makarenko, K. Mönig, T. Shishkina, hep-ph/0306135.